5-2014

Dynamic Complexity and Causality Analysis of Scalp EEG for Detection of Cognitive Deficits

Joseph Curtis McBride
University of Tennessee - Knoxville, jmcbrid4@utk.edu

To the Graduate Council:

I am submitting herewith a dissertation written by Joseph Curtis McBride entitled "Dynamic Complexity and Causality Analysis of Scalp EEG for Detection of Cognitive Deficits." I have examined the final electronic copy of this dissertation for form and content and recommend that it be accepted in partial fulfillment of the requirements for the degree of Doctor of Philosophy, with a major in Biomedical Engineering.

<div align="right">Xiaopeng Zhao, Major Professor</div>

We have read this dissertation and recommend its acceptance:

J.A.M. Boulet, Jeffrey Reinbolt, William Hamel, Adam Petrie, Kristin King

<div align="right">Accepted for the Council:
<u>Dixie L. Thompson</u></div>

<div align="right">Vice Provost and Dean of the Graduate School</div>

(Original signatures are on file with official student records.)

Dynamic Complexity and Causality Analysis of Scalp EEG
for Detection of Cognitive Deficits

A Dissertation Presented for the
Doctor of Philosophy
Degree
The University of Tennessee, Knoxville

Joseph Curtis McBride
May 2014

DEDICATION

For my wife and family whose love,
patience, and support have made this work possible.

ACKNOWLEDGEMENTS

ABSTRACT

This dissertation explores the potential of scalp electroencephalography (EEG) for the detection and evaluation of neurological deficits due to moderate/severe traumatic brain injury (TBI), mild cognitive impairment (MCI), and early Alzheimer's disease (AD). Neurological disorders often cannot be accurately diagnosed without the use of advanced imaging modalities such as computed tomography (CT), magnetic resonance imaging (MRI), and positron emission tomography (PET). Non-quantitative task-based examinations are also used. None of these techniques, however, are typically performed in the primary care setting. Furthermore, the time and expense involved often deters physicians from performing them, leading to potential worse prognoses for patients.

If feasible, screening for cognitive deficits using scalp EEG would provide a fast, inexpensive, and less invasive alternative for evaluation of TBI post injury and detection of MCI and early AD. In this work various measures of EEG complexity and causality are explored as means of detecting cognitive deficits. Complexity measures include event-related Tsallis entropy, multiscale entropy, inter-regional transfer entropy delays, and regional variation in common spectral features, and graphical analysis of EEG inter-channel coherence. Causality analysis based on nonlinear state space reconstruction is explored in case studies of intensive care unit (ICU) signal reconstruction and detection of cognitive deficits via EEG reconstruction models. Significant contributions in this work include: (1) innovative entropy-based methods for analyzing event-related EEG data; (2) recommendations regarding differences in MCI/AD of common spectral and complexity features for different scalp regions and protocol conditions; (3) development of novel artificial neural network techniques for multivariate signal reconstruction; and (4) novel EEG biomarkers for detection of dementia.

TABLE OF CONTENTS

LIST OF TABLES

LIST OF FIGURES

CHAPTER 1
INTRODUCTION AND CURRENT EEG RESEARCH
IN TBI, MCI, AND AD

Introduction to EEG

A Brief History of EEG

EEG has emerged as a potential clinical tool of interest in diagnosing and monitoring the pathological progression of neurological disorders including TBI and dementia over the last two decades. The revival of interest in EEG is the result of new technological developments that have allowed for the fast computation of various connectivity and complexity features of EEG which research suggest have potential application as biomarkers of neurological disease [110].

Richard Carton first described EEG in 1875, when he noted electrical oscillations on the exposed cortical surface of animals [111]. Fifty years later, Hans Berger began a series of reports in 1929 that are commonly accepted as the first systematic description of human EEG [48]. Quickly following Berger, Gibbs and Gibbs noted that EEG oscillatory behavior was sensitive to the effects of anesthetic agents. Specifically, the frequency of dominant EEG rhythms appeared to correlate with levels of alertness and attention [48]. The next century saw a significant improvement in transducers, amplifiers, and other equipment used to record and display EEG [110]. In the last 30 years, progress has been made toward understanding the genesis of EEG waveforms and how they relate to brain function [110].

Currently, EEG monitoring is often used to visually assess the general "well-being" of the higher central nervous system after injury and to assess the level of alertness of patients receiving anesthetics or pharmaceuticals [110]. EEG has also found numerous applications in the diagnosis and evaluation of neurological disorders. EEG is used to assess autonomic reactions of visual and auditory stimuli, thereby providing evidence for neurological deficits (e.g., use of EEG in newborn hearing screenings) [57]. EEG continues to be extensively used in studies of sleep disorders, where the frequencies of dominant EEG rhythms are used to assess depth of sleep [139]. EEG is generally accepted as being a highly sensitive and moderately specific indicator of brain swelling (ischemia) and oxygen deprivation (hypoxia) [110]. When EEG oscillatory behavior is correlated to functions of the cerebral cortex, such as awareness and memory, reliable and clinically relevant results have been observed [84,86]. These results provide supporting evidence for the current understanding that EEG is a phenomenon of the cerebral cortex.

Genesis of EEG Potentials

Bioelectrical potentials measured on the skin's surface are caused by the flow of ion-based electrical currents within the body [110]. The macroscopic currents recorded via EEG are the net summation of microscopic currents contributed by billions of individual

neurons in the brain [110]. Each neuron consists of a central body, called a soma, and branching tendrils called dendrites and axons. Dendrites carry afferent signals and axons carry efferent signals. Each soma has many dendrites but typically a single axon. The axon itself many have several branches. The axons and dendrites communicate via chemical reactions initiated or halted by neurotransmitters that occur at the junction between axons and dendrites. The junctions between the end of an axon and a dendrite (or in some cases, the soma) are known as synaptic gaps; see Fig. 1.1 for a schematic of a typical neural cell. The paths involved in the transmission of information throughout the brain are known as synaptic pathways [121].

The electrical activity of neurons can be separated into two categories: postsynaptic potentials (PSP) and regenerative action potentials (AP). PSPs occur when neurotransmitters released by a presynaptic axon alter the permeability of ion channels in the membrane of postsynaptic neural cells [110]. Subsequent flow of ions in and out of a postsynaptic cell changes the cell's transmembrane ionic gradient, and thus its transmembrane voltage. Neurotransmitters act over a very short distance, resulting in localized changes in transmembrane voltages, with the magnitude of voltage changes decreasing exponentially with distance from the synapse [110]. The change in transmembrane potential can be positive (depolarization) or negative (hyperpolarization). PSPs decay over time due to cessation of ligand-channel activity as a result of reuptake of neurotransmitters or PSP-induced currents that redistribute ionic charges [110]. PSPs last from tens of milliseconds to seconds. If a neuron's membrane is depolarized beyond an intrinsic threshold, an AP is initiated. APs propagate rapidly along neural membranes without diminishing in amplitude. The constant voltage of APs is sustained by voltage-sensitive ion channels [110]. APs typically last for about 2 ms and may reach approximately 100 mV in amplitude.
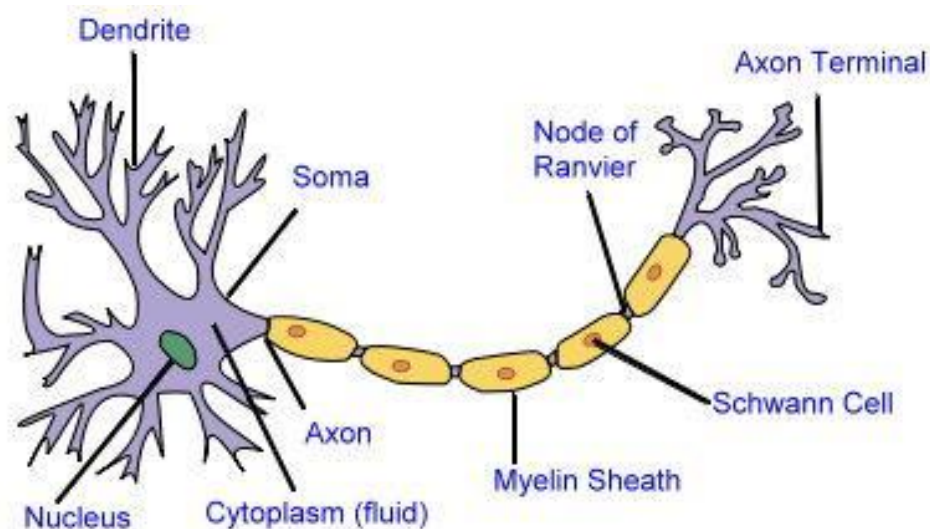
Fig. 1.1. General Schematic of A Neural Cell; figure copied from [128].

2

PSPs of pyramidal neurons in the brain are believed to be responsible for the macroscopic currents detected via EEG [110]. Pyramidal cells are neurons that have long, apical dendrites that extend through the cortical layers of the brain, from the soma toward the exterior surface of the cerebral cortex [158]. Pyramidal cells are thus arranged with relatively parallel dendrites. Each of these dendrites receives inputs from thousands of other neural cells. Interestingly, neighboring dendrites tend to receive PSPs from the same sources at homologous locations along their respective dendrites [110]. Physical distances between inhibitory and excitatory PSPs on individual dendrites yield bridging current loops between the PSPs [110]. Because neighboring pyramidal cells have similar PSP voltages at similar positions, their individual current loops combine additively in the extracellular fluid, creating voltages large enough to be detected on the surface of the scalp; see Fig. 1.2.

Recorded EEG voltages are the result of millions of asynchronously firing PSPs from all over the cerebral cortex. Thus, unlike electrocardiography (ECG), which is used to record the electrical activity of the heart, normal EEG has no readily apparent, repetitive nature [110]. Decades of research suggest, however, that certain characteristics of EEG are indicative of underlying brain activity [110]. For example, higher cortical function, such as abstract thought, is usually associated with higher frequencies and greater desynchronization of EEG channels [121]. In certain instances, such as specific stages of sleep, EEG may exhibit characteristic waveform features (e.g., K-spindles) which can be used for diagnostic purposes [57].

EEG Signal Acquisition

In order to record EEG potentials, metal needles or electrically conductive gel electrodes are used as transducers that convert physiological EEG currents into electrical currents capable of being recorded and processed. EEG is typically measured using multiple electrodes arranged on the scalp in a specific manner. The most commonly used arrangement is the International 10-20 System [68]. The 10-20 system is based on meridians crossing the scalp with additional lines drawn over the midfrontal and midparietal lobes. The typical nomenclature used to designate electrodes includes a prefix that indicates the brain/scalp region (e.g., C = central, F = frontal, T = temporal, etc.) and a number that indicates the relative distance from the midline. Right hemispheric electrodes are designated with even numbers (e.g., F4) and left hemispheric electrodes are designated with odd numbers (e.g., F3). Electrodes along the midline are designated with a Z (e.g., FZ) rather than a number.

EEG recordings are digitized samples of the continuous physiological potentials on the scalp. Digitization implies quantization in amplitude and time, the resolution of which are dependent on the number of bits and sampling frequency used [110]. The accuracy of binary numbers is determined by the number of bits they contain. For example, a 16-bit number can represent 2^{16} or 65,536 possible states. Assuming a range of -1.0 to +1.0 V, a 16-bit converter would allow for a resolution of approximately 30 μV. Sampling frequency inherently determines the maximum frequency of EEG oscillations that can be recorded without aliasing effects. The sampling rate should always be more than twice the highest
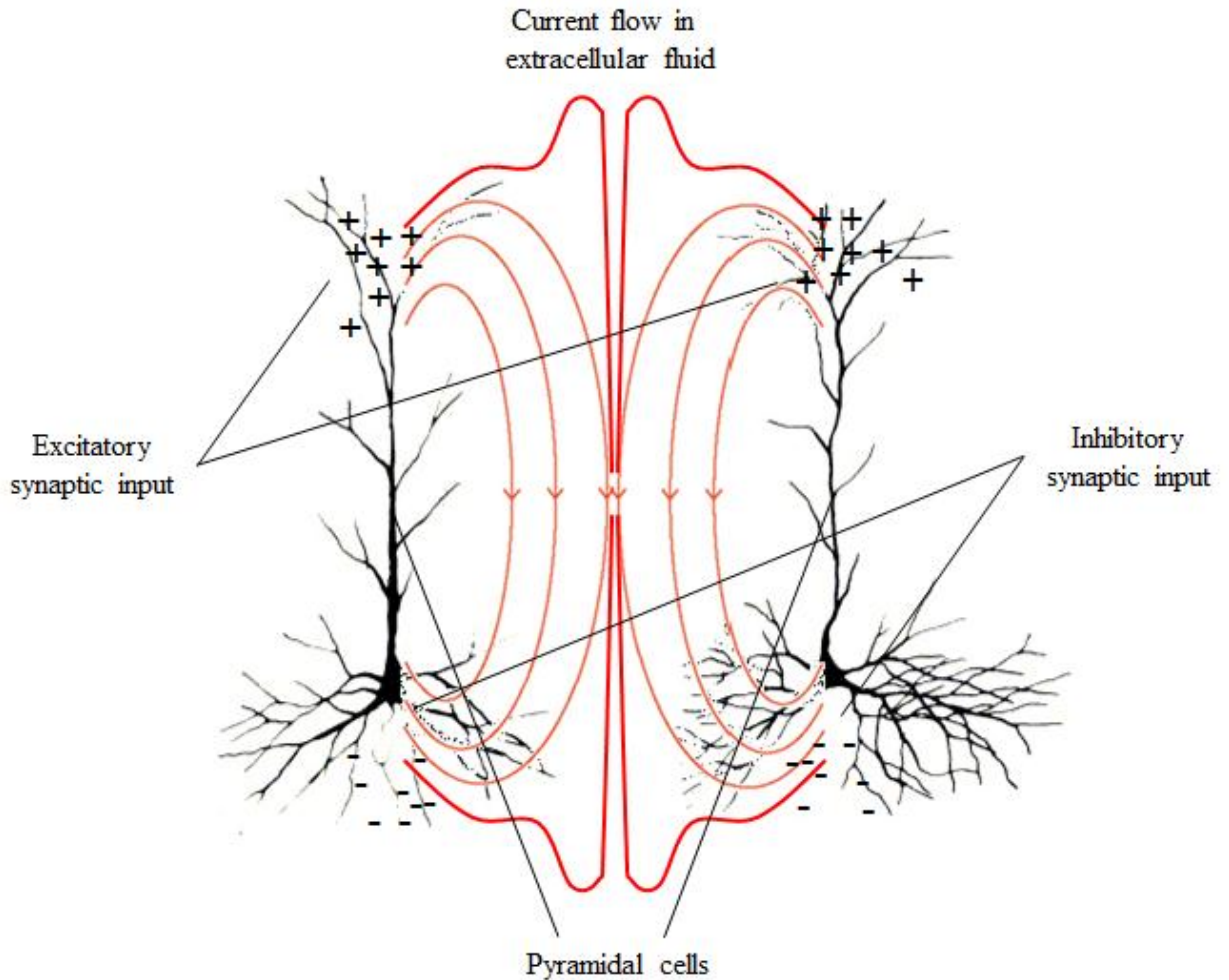
Fig. 1.2. Illustration of Current Loops in Extracellular Fluid Surrounding Pyramidal Cells.

expected frequency (or highest frequency of interest) [120]. Diagnostic EEG is typically sampled at 500 or 1000 Hz [110].

Preprocessing of EEG

Preprocessing of EEG is needed to remove artifacts that may appear due to electromyographic (EMG) sources and background electronics [110]. The most common source of EMG artifacts is eye blinks [110]. Transocular electrodes are often used to detect eye blinks and remove eye blink artifacts. In addition, the human body acts as an antenna, amplifying 60 Hz frequencies of background electronics [110]. For this reason, a 60 Hz notch filter is often used to remove 60 Hz frequency components. Alternatively, EEG may be recorded in specially designed rooms that mitigate interferences from background electronics. Finally, low-pass filters are used to remove any high frequency noise. Typically, only frequencies below 80 Hz are considered to be physiologically relevant [110].

Introduction to TBI

Overview of TBI

TBI can be defined as any acute physical injury that disrupts normal brain function. Usually such injuries are head injuries, but injuries to the chest due to concussive blasts can also produce TBI symptoms [30,157]. The severity of TBI is categorized by the severity of symptoms as mild, moderate, or severe [157]. In the case of mild traumatic brain injuries, patients may or may not experience a loss of consciousness for a short period of time, as well as headaches, faulty sensory adaptation, fatigue, changes in sleeping behavior, and mood disorders [95]. Those with moderate TBI suffer loss of consciousness (typically less than 1 hour), post-traumatic amnesia (PTA, typically less than 24 hours), and localized brain damage such as bleeding, bruising or lesions. Severe TBI usually presents loss of consciousness greater than 1 hour, PTA greater than 24 hours, and localized brain damage [95]. Repeated vomiting and nausea are also common symptoms of moderate and severe TBI due to increased intracranial pressure [157]. Severe TBI also has a multitude of unique symptoms including coma, incongruities in pupil dilation, and partial paralysis or numbness in the extremities [157]. When the skull is penetrated during the initial traumatic event, the patient is more likely to suffer severe TBI symptoms [121].

TBI does not necessarily imply loss of consciousness. In fact, one of the major difficulties in diagnosing mild TBI is that patients may not present with any obvious initial symptoms, such as loss of consciousness, and therefore are not often tested further by means of CT, MRI, or PET scanning [157]. Even in cases of severe TBI, such as gunshot wounds to the head, loss of consciousness does not always occur [157]. A system of the brain known as the Reticular Activating System is believed to be responsible for wakefulness and is located in the midbrain [121]. Research suggests that it is damage to this system resulting from rotational forces in the midbrain that is believed to be the cause of concussions and chronic fatigue post injury [121].

The most common causes of TBI in the United States are falls (28%), motor-vehicle collisions (20%), accidental trauma (19%), and physical assaults (11%) [157]. Concussive blasts are the leading cause of traumatic brain injury for active duty military personnel in war zones [30]. The risk of TBI varies with age and occupation, with the two age groups at greatest risk of injury being infants to 4 years of age and those 15- to 19-years old [157]. Occupations with high incidence of TBI include construction and certain military duties, such as paratrooping and infantry combat [30,157].

Pathology of TBI

The pathology of TBI can be divided into the physical processes immediately following the incident of injury (primary pathology) and the secondary pathology due to the natural healing processes including inflammation and scarring [121]. Primary pathology can be viewed as resulting from a combination of localized injury to the brain and diffuse axonal injury (DAI) throughout the brain.

Localized injury to the brain implies that a specific region of the brain is injured, such as a contusion in a particular area [121]. When the head experiences large acceleration/deceleration, the brain may strike the interior of the skull with enough force to incur damage. Because of the brain's anatomical positioning within the skull, the frontal and temporal lobes are the regions of the brain especially vulnerable to such injuries [30]. These regions are also where emotions and memory are formed and processed, where visual information is deciphered, and language is formulated. Patients with injuries to these regions of the brain often suffer from depression, have trouble maintaining socially acceptable behavior, and have difficulty communicating verbally [29,108].

When the brain strikes the skull, the soft tissues of the brain are compressed and stretched, and blood vessels that cover the surface of the brain or exist in the blood-rich protective layers between the brain and the skull may be stretched or torn [125]. The stretching and tearing of these blood vessels result in either micro-scale hemorrhages or overt bleeds. The collection of blood resulting from an intracranial bleed, known as hematoma, can increase intracranial pressure and surgery may be required to relieve the pressure within the skull and to stop bleeding. Surgery may also be required to remove blood clots that may develop. If an expanding hematoma is not treated quickly, other regions of the brain may become bruised, damaged, or ischemic, which can lead to regional brain cell death or the death of the patient [9,29,157]. Confirmation of the presence of a hematoma is best obtained from a non-contrast CT scan, although it can be identified on an MRI scan as well [121,157]. Unfortunately mild TBI patients do not routinely have CT or MRI scans performed, and may have small intracranial bleeds that remain undiagnosed until the bleed becomes a serious problem later on [157].

Unlike localized injuries to the brain that may result from TBI, such as contusions and intracranial bleeds, DAI occurs throughout the brain and is believed to be the cause of many of the later symptoms that develop from mild TBI [9,14,121,144]. When the brain experiences sharp acceleration/deceleration, axons within the brain are stretched and compressed because of their relatively fixed length and positions [51]. If the axons of a neural cell are sufficiently injured by such deformations, the cell will not survive [51,121]. The death of neurons is a common feature of TBI and occurs in small pockets throughout the brain. Though global in nature, the small scale of DAI makes the detection of DAI damage with CT and MRI scans difficult or impossible [64]. Instead, the diagnosis of DAI is usually made on the basis of a patient's symptoms, such as loss of consciousness. Anytime there is a loss of consciousness associated with a traumatic head injury DAI is present, and the length of time a patient is unconscious following TBI is directly correlated with the severity of DAI [64]. DAI, however, also occurs in patients who do not lose consciousness. For these patients, degenerative symptoms brought on by the secondary pathology of axonal injury are usually the only means of diagnosis, at which time little can be done to mitigate the damage [64,121].

Secondary pathology of TBI includes pathology resulting from the body's natural healing processes [157]. For example, as a result of the body's natural inflammatory response generalized swelling of the entire brain, known as edema, can occur after well after the time of the initial injury. Edema can cause increased intracranial pressure without

6

the presence of localized contusions or bleeds [121]. Depending on the location of the brain injury and level of intracranial pressure, damage to the midbrain or brain stem may occur. This is a potentially serious condition because damage to these regions of the brain can result in the loss of a patient's vital involuntary regulatory processes, such as breathing [29,108]. Depressed ventilatory status can lead to ischemia or hypoxia, which may result in large areas of neuronal demise or even brain death [108].

Some neurological symptoms of TBI present weeks or months after the injury. The cause of these symptoms is often due to the natural healing processes taking place in the brain. The development of fibrous scar tissue, for example, can act as an insulating factor and disrupt the flow of electrical signals (APs and PSPs) along a patient's synaptic pathways [121]. Years after the initial injury, as the scar tissue begins to tighten, further deformation of axons and disruption of synaptic pathways may occur, causing new or worsening symptoms [121].

Another common issue observed in TBI is the swelling of individual neural cell clusters in the brain, forming pockets known as axonal nodes [64,121]. These axonal nodes have similar effects to that of scar tissue. The physiopathology of axonal node development is not well understood, but it is believed to be the result of neural cells responding to specific neurotransmitters that "leak" from damaged axons during initial DAI and the presence of proteins associated with the natural inflammatory process [64].

Current Diagnostic Techniques Applied to TBI

Currently the most common methods of diagnosing TBI are the Glasgow scales, CT and MRI scanning, and biomarker proteins [157]. The Glasgow Coma Scale (GCS) tests are used to grade patients' level of consciousness post injury, focusing on eye responsiveness and verbal and motor functioning tests. The Glasgow Outcome Scale (GOS) tests are used to measure patients' levels of recovery long after the incident of injury [51]. CT, MRI, and PET scans are utilized to locate contusions of the brain, blood clots within the skull, and possible intracranial swelling that may take place soon after TBI [121,157]. Certain biomarker proteins in the blood and cerebrospinal fluid (CSF), which are characteristic of brain and nervous system injuries, are also used to detect TBI [102].

Glasgow Scales
The GCS is a common method used to determine the severity of TBI soon after injury [157]. Patients' scores are based on their best verbal responses, their ability to follow simple instructions, and eye opening responsiveness. GCS scores range from 3 to 15, with 3 indicating a patient whose eyes do not open, is incapable of speaking or making verbal sounds, and does not respond to simple instructions or painful stimuli. Low GCS scores are indicative of severe TBI. A score of 15 indicates that a patient has his/her eyes open and is capable of speaking and following simple instructions. Under current diagnostic criteria, a GCS score of 8 or below is indicative of severe TBI, 9-12 moderate TBI, and 13-15 mild TBI [51,157].

Certain factors affect the diagnostic validity of GCS tests. Often in emergency situations patients are intubated, a procedure during which a tube is placed down the patient's trachea to ensure a patent airway. Conscious patients must be sedated before they can be intubated. By the time GCS test are performed, patients may have been sedated and intubated, preventing them from performing the verbal GCS tests and affecting their response to the eye responsiveness and instruction exams [51]. The non-verbal GCS tests are usually still performed, with the fact that a patient is intubated during the test being denoted by a T next to the score (e.g., GCS 5T). Afterwards, the GCS tests are generally performed at regular intervals in attempt to acquire more accurate assessments [51]. Aside from intubation, the GCS score also fails to take into account the mental status of patients before or at the time of injury. Previously existing mental impairment or the consumption of alcohol prior to the incident of injury could negatively influence a patient's GCS score. Furthermore, GCS scores are often ineffective in diagnosing mild TBI injuries due to the fact that mild TBI patients often have high or normal GCS scores soon after the incident of injury [51,121,157].

Contrary to the GCS, the GOS is used to assess patients' levels of recovery post injury and is not intended to be a means of diagnosis. The GOS does not include in-depth neuropsychological testing. Occasionally GOS tests do serve as the means of diagnosis when patients' symptoms become progressively worse post injury due to secondary pathology of undiagnosed mild TBI [51,157].

CT, MRI, and PET

CT scans are performed using X-rays and produce images of the human brain that allow for detection of injures including contusions of the brain, intracranial bleeds, and brain swelling [121]. The X-rays used in CT scanning produce density maps of the body so that dense objects, such as metals and bone, cause significant image degradation. With non-contrast CT scans, intracranial hemorrhages are easily visible [121].

MRI scans are also used to diagnose brain swelling, contusions, and intracranial bleeds. MRI uses the magnetic resonance properties of molecules in tissues and primarily images the protons in the hydrogen atoms in water molecules [64]. MRI images are degraded somewhat by metallic foreign bodies but not to the extent that a CT is [121]. Certain medical devices, such as cardiac pacemakers, experience interference from the intense magnetic fields of the superconducting MRI magnets. Thus, patients containing such devices cannot be imaged by MRI [64]. Studies have demonstrated that neither CT nor conventional MRI is effective in determining the presence of DAI [64]. Diffusion tensor imaging, a specialized type of MRI that measures water diffusion in the brain, appears to be more sensitive in detecting DAI than traditional MRI scans, but still lacks the accuracy required for diagnosis [121].

PET scans use gamma radiation to detect levels of radioactively tagged glucose in the brain, with high levels of glucose being indicative of greater glucose consumption and therefore greater brain activity [29,108]. PET scans are currently used to detect areas of the brain with abnormal inactivity, which could indicate the presence of trauma.

Unfortunately, PET scans are not conducted outside of hospitals and PET scanning is not specific to TBI detection [121,157].

Biomarker Proteins

Recent research studies have identified proteins found in the blood and CSF that appear to be characteristic of TBI and neurological injuries [102]. Levels of these proteins in the blood and CSF increase soon after TBI and can be used as a possible means of diagnosing and measuring the severity of TBI. CSF measurements are generally preferred over blood samples because it is believed that blood serum levels of these proteins are more affected than CSF levels by non-nervous system sources [102]. Unfortunately, measurement of these proteins is still not reliable as a solitary means of diagnosing TBI and is usually performed in conjunction with other diagnostic tests, such as GCS tests, CT, or MRI.

Introduction to MCI and AD

Overview of MCI and AD

MCI, especially the amnestic type, is a degenerative neurological disorder defined by cognitive decline of a greater degree than expected for an individual's age but does not necessarily interfere with daily activities [45,100]. Early stages of AD cause similar symptoms of cognitive degeneration including progressive memory loss, shrinking vocabulary, and lower ability to execute precise motor movements. MCI is known to be a related neurological disorder to AD; however, there is still debate in the scientific community regarding whether MCI is an early stage of AD, simply comorbid with AD, or actually predisposes patients to developing AD [101,155]. Previous research has shown that MCI patients progress to AD at rate of approximately 10-15% of patients per year. An estimated 16% of individuals over the age of 70 years present with MCI symptoms [101]. The prevalence of MCI and AD increases with age, making MCI research of significant interest in geriatric medicine. Accurate identification of patients with MCI is crucial for AD treatment and research because patients with MCI are at high risk of developing AD. A major goal of current research is the development of early treatments with new therapies that may forestall or slow cognitive decline of MCI and AD.

AD is the most common form of dementia in the United States, effecting millions of Americans [151]. The disease process is known to cause a generally slow progression of cognitive degeneration. Early stages of AD include symptoms similar to MCI, both of which are commonly undiagnosed. AD is generally diagnosed sometime within the 4th to 14th year of the disease, during which time symptoms progress to a point that patients and their family/caretakers become aware that an obvious problem exists [151]. Symptoms during this later stage of the disease include the inability to speak except in simple phrases, inability to recognize close relatives and family members, loss of personality, and increasing aggression, irritability, or other indications of decreased inhibitory higher brain

functions. The disease ultimately results in death, usually through external factors such as infection of pressure ulcers or pneumonia [151].

Pathology of MCI and AD

Several causes for MCI and AD have been hypothesized based on the observations of chemical imbalances in the brains of AD patients; however, no definitive cause has yet been determined. Two of the leading hypotheses for the cause of AD are the tau hypothesis and the amyloid beta hypothesis.

Mammalian neural cells in the brain require the microtubule protein tau to function properly [66]. In a brain with AD, tau is abnormally hyperphosphorylated. The protein becomes toxic at higher concentrations when produced in excess and begins causing neurodegeneration. The brain's natural immune response to elevated levels of hyperphosphorylated tau is the formation of inert polymers from the toxic tau proteins [66]. The resulting neurofibrillary "tangles", however, consequently contribute to further cognitive degeneration [17].

The amyloid hypothesis postulates that amyloid beta deposits are the cause of AD. The peptide is contained in plaques found in AD brains post mortem [159]. Research with transgenic mouse models indicates that amyloid beta deposition is a key component in the disease process. Immunological therapies that decrease amyloid beta concentrations have been shown to have stabilizing effects on cognitive degeneration [159].

Other hypotheses for the cause of AD include the breakdown of the myelin sheaths of neural cells, which serve as protective insulation for neural cells' axons and dendrites [16]. This hypothesis is difficult to test experimentally, however, because myelin breakdown is known to be a normal effect of aging [16]. Another hypothesis currently being considered is oxidative stress signaling. Oxidative stress is caused by an imbalance in biochemical processes, resulting in the production of reactive oxygen species (ROS). ROS levels are mainly affected by mitochondrial and metabolic abnormalities; however, amyloid beta levels have been shown to be a minor factor [137].

No root cause has been attributed to MCI; however, given the high number of MCI patients that progress to AD, the causes of both diseases may be related on a fundamental level [151].

Current Diagnostic Techniques Applied to MCI and AD

Protein Biomarkers

Unfortunately, the diagnostic capabilities for AD are limited, with only "possible" or "probable" diagnoses being capable. Definitive diagnosis of AD can only truly be made by a post-mortem analysis of the brain [151]. Nevertheless, physicians have developed an array of neuropsychological exams and assessments that allow them to diagnose patients accurately while they are still alive.

The earliest stage of MCI and AD diagnosis is often based on neuropsychological tests and patient history evaluations [101]. Once it is determined that a patient is experiencing abnormal cognitive decline, physicians employ more quantitative diagnostic tools. One such tool is the analysis of CSF biomarker proteins [8]. The most common CSF biomarkers used for AD diagnosis are amyloid beta and tau. These proteins provide one of the more reliable means of distinguishing AD from other forms of dementia and appear in characteristically abnormal levels at the earliest onset of the disease [8]. Published findings suggest that spinal taps cap identify abnormal proteins in patients who went on to develop AD later [39].

PET and MRI

Imaging in Alzheimer's diagnostics is one of the fastest growing areas of the disease's study. PET and structural MRI are two of the leading imaging methods used currently. PET is generally used to analyze neurochemical activity in the brain. In AD research, the amyloid-binding compound Pittsburgh Compound-B (PiB) is most widely used [65]. The regional variation in PiB binding *in vivo* are strikingly similar to the deposits of amyloid beta and tau neurofibrillary tangle distributions observed post mortem [65]. PET scans have been able to measure PiB uptake of the neocortex and identify the regional placement of the amyloid beta plaque burden with moderate specificity [85].

Structural MRI studies have focused on the hippocampus, one of the main areas of the brain affected by the disease and the center of neurofibrillary pathology [67]. These scans can also measure myelin breakdown rates in the brain as a function of a patient's age, one of the key components in the consideration of the patient's treatment [16]. Structural MRI is often used in conjunction with PET as using both imaging modalities provides a more well-rounded view of the brain and its diseased areas.

Current EEG Research in TBI, MCI, and AD

Evaluation of TBI Using EEG

EEG data have been used to study TBI patients' severity of injury, level of awareness and unconsciousness, and to predict patient outcome. Such computer-aided signal processing of EEG data is often referred to as quantitative EEG (QEEG) [152]. QEEG has been studied in conjunction with other neurological indicators, such as MRI, to predict gross outcomes of TBI patients.

One of the first QEEG methods investigated was Fourier Transform EEG (FT-EEG), which provides concurrent and continuous resolution and quantification of all relevant brainwave frequency bands. Leon-Carrion *et al.* demonstrated the ability of FT-EEG to correctly discriminate between different levels of functional dependence for individuals who had sustained TBI [73]. Others have shown that FT-EEG can better predict survival of TBI patients than other common clinical tools, such as GCS tests [152]. More recently, FT-

EEG and MRI have been used as complementary tools in order to relate anatomical and physiological symptoms of injuries of TBI patients [60,140,141,146]. In a related approach to FT-EEG, Thatcher *et al.* used variables derived from EEG spectral analyses to accurately classify mild (n=40), moderate (n=25), and severe (n=43) TBI patients, achieving a classification accuracy of 96.39%, sensitivity of 95.45%, and specificity of 97.44% [142].

QEEG-derived techniques have also been used to examine differences in responsiveness and level of awareness in TBI individuals. The Bispectral Index (BSI), derived from EEG, is primarily used to monitor the depth of unconsciousness in TBI patients. Paul and Rao have also shown that in patients with mild and moderate head injuries there was a significant correlation between GCS scores and BSI; however, the large degree of scatter of BSI values for a given GCS score limits the use of BSI as a monitor for depth of coma in TBI [99]. Docktree *et al.* and Roche *et al.* examined differences in the response times (RTs) and alpha band power synchronization of TBI EEG and controls during a Sustained Attention Response Task [40,114]. They noted that while controls demonstrated lengthening RTs and alpha band power desynchronization, TBI individuals demonstrated shorter RTs with no evidence of alpha desynchronization. Angelakis *et al.* studied trait and state differences in peak alpha frequency, a measure of alertness that has been correlated to cognitive performance [6]. EEG recordings were taken before and after visual and auditory working memory tasks, including repeated tasks (WAIS-R Digit Span). They concluded that TBI individuals demonstrated significantly lower peak alpha frequencies, mostly during post-task rest.

In addition to traditional QEEG and imaging techniques, several researchers have also explored the use of EEG entropy analyses for evaluation of brain injuries. For example, Tong *et al.* explored statistical characteristics of Tsallis-like time-dependent entropy derived from EEG of individuals who had suffered asphyxic cardiac arrest (ACA) injury [144]. Specifically, the mean and variance of Tsallis-like time-dependent entropy showed good specificity to ACA brain injury and its recovery. Cao and Slobounov used entropy to measure EEG nonstationarity and used nonstationarity features to discriminate mild TBI [28]. Bezerianos *et al.* showed that EEG rhythm changes estimated from time-dependent entropy can be used to discriminate brain ischemia damage [18]. Zhang *et al.* used Tsallis entropy in quantifying burst suppression in rats after induced ACA injury [163].

Diagnosis of MCI and AD Using EEG

Recent research in exploring the potential for diagnosing MCI and AD from EEG has yielded three major observations: (1) slowing of EEG, (2) reduced complexity of EEG, and (3) perturbations in EEG synchrony [37]. Current techniques used for detecting each of these abnormalities are summarized here. In addition, limitations of computational analysis of EEG for diagnosing MCI and AD are discussed.

Slowing of EEG
Different EEG frequency bands are known to be of physiological relevance. These bands include delta band frequencies (0—3.5 Hz), theta band frequencies (3.5—7.5 Hz), alpha band frequencies (7.5—12.5 Hz), beta band frequencies (12.5—25 Hz), and gamma

band frequencies (25—100 Hz). Delta and theta frequencies are associated with sleeping, drowsiness, and daydreaming; alpha and beta bands are associated with being awake and alert; gamma band frequencies are associated with short-term memory and cross-modal tasks (tasks which require various regions of the brain to work in concert) [57]. AD appears to affect each of these EEG frequency bands in specific ways. Previous research has shown that MCI and AD EEG demonstrates a "slowing," or a shift in spectral power of EEG toward the lower frequency bands [15,20,35,46,58,83,94,107,119,148]. Interestingly, however, increased spectral power in the gamma band has also been reported in MCI and AD compared to normal individuals [149]. Oscillations in high-energy regions of time-frequency maps of EEG activity have also been observed to occur at lower frequencies in MCI and AD, indicating that the frequency of transient EEG oscillations also "slow" in AD [37].

Reduction in EEG Complexity

Various complexity measures have been used to quantify EEG complexity [37]. Several of these are measures with roots in information theory, including Tsallis entropy, approximate entropy, sample entropy, multiscale entropy (MSE), and Lempel-Ziv complexity.

In information theory, entropy is a measure of the uncertainty associated with a random variable. The classical mathematical definition of entropy was proposed by Shannon, and is referred to as Shannon entropy [123]. Tsallis entropy is a nonextensive generalization of Shannon entropy, parameterized by a nonextensivity parameter q. The parameter q is a measure of the nonextensivity of the system of interest. Nonextensivity refers to the fact that a system's total entropy is not equal to the sum of the entropy of its constituent parts [34]. See Chapter 2 for more details regarding the mathematical theory of Tsallis entropy.

Sneddon *et al.* investigated Tsallis entropies computed for event-related EEG intervals during a delayed recognition task as well as a test of perception of structure-from-motion (SFM) [126]. Specifically, a ratio of anterior to posterior event-related Tsallis entropies was computed. Sneddon *et al.* demonstrated that the Tsallis entropy measure used was capable of high discrimination between normal and MCI individuals when applied to the delayed recognition task, yielding results that were comparable to the accuracy reported for PET scans. Tsallis entropy did not perform well for the SFM task, suggesting that the event-related Tsallis entropy measure used may be specific to different psychological tasks [126]. In another study, Zhao *et al.* demonstrated that normalized Tsallis entropies can be used to compute EEG markers that appear to discriminate AD from normal individuals [164].

Approximate entropy is an entropy measure that reflects the likelihood that patterns in a time series will be followed by "similar" patterns [37, 106]. Sample entropy is a modified version of approximate entropy, which employs smaller bins [82]. In MSE analysis, the entropy of coarse-grained time series, constructed from the original time series, are computed for various coarseness parameter values (scales) [32,33]. The entropy

of each coarse-grained time series may be computed using Tsallis entropy, approximate entropy, or sample entropy. See Chapter 3 for more information on the derivation of MSE.

Lempel-Ziv complexity measures the number of unique patterns in a times series [71]. See Chapter 5 for more details regarding the mathematical theory of Lempel-Ziv complexity. Lempel-Ziv theory is used in the Lempel-Ziv-Welch compression algorithm. The extent of compression, often expressed as a ratio of the file size before and after compression, is a measure of the regularity of a time series.

Differences in measures of approximate entropy, sample entropy, MSE, and Lempel-Ziv complexity in MCI and AD have been investigated in several studies [1,2,3,62,98,160]. All of these studies observed greater regularity (decreased complexity) in the EEG of individuals with MCI and AD. No biological mechanism has been determined to be responsible for this phenomenon. It should be noted that decreased complexity might also be related to the slowing of EEG, since slower (low pass) signals are intrinsically more regular [37].

Changes in EEG Synchrony
A multitude of studies have reported decreased synchronization in EEG of MCI and AD patients recorded during resting states. These studies have employed a large variety of synchronization measures including the Pearson correlation coefficient, magnitude and phase coherence, Granger causality, phase synchrony, state-space synchrony, stochastic event synchrony, mutual information, and graphical network measures.

Perhaps the most basic synchrony measure, the Pearson correlation coefficient is a measure of the linear correlation between two time series. Although there have been published findings suggesting the decrease in Pearson correlation coefficients in EEG of MCI patients compared to normal individuals, results have not been statistically significant. Furthermore, no differences have been observed between AD patients and normal individuals [37].

As a frequency domain analog to the Pearson correlation coefficient, magnitude coherence measures linear correlations in the frequency domain. Many studies have demonstrated a decrease in magnitude and phase coherence in MCI and AD patients' EEG [7,19,24,52,59,61,69,87,132,136,150]. In some studies, differences have even allowed for the discrimination of MCI and normal controls' (NC) EEG records using coherence features. Contradictory results, however, have also been reported, which suggests that coherence features may be incapable of serving as discriminatory features for distinguishing between MCI and NC or AD and NC [36,38,72,134,135].

Granger causality extends correlation coefficients from two time series to multiple time series, allowing for the estimation of the causality of linear interactions. Many different Granger causality measures have been proposed, including linear and nonlinear extensions [5,31,74]. Examples of linear measures include the direct transfer function (DTF) and full frequency directed transfer function (ffDTF). Previous research has noted

decreased ffDTF in MCI and AD patients compared to NCs; however, only a minor decrease in DTF was observed, and only for AD patients [36,38].

All of the above measures assess synchronization of the amplitude/magnitude of time series. In addition to the amplitude synchrony measures, phase synchrony measures have also been investigated. Examples include mean phase coherence, phase lag index, imaginary coherence, and global field synchrony (GFS) [77,81,132]. While the other phase synchrony measures compare the phase of two time series, GFS allows for the detection of phase coupling between a large number of channels. Decreased phase synchrony has been reported in resting EEG of mild AD patients [132]. A general decrease in GFS has been observed in AD; however, Park *et al.* did not observe this effect in MCI [36]. In addition to GFS, Park *et al.* investigated five additional phase synchrony measures, none of which demonstrated significant differences between MCI patients and NC. In a similar study, Dauwels *et al.* observed no differences in AD patients [38]. Differences have been reported in the spatial distributions of EEG phase synchrony between AD patients and NCs [76].

Another group of synchrony measures includes state-space synchrony measures. These measures are based on the assumption that time series are generated by an unknown, deterministic, and potentially high-dimensional nonlinear dynamical system. Generally, an attempt is made to reconstruct the system by representing the time series in a state space, where each time series is represented as a trajectory in the in the state space. Signals are considered to be synchronous if their trajectories remain "close" to each other [37]. Significant decreases in sate-space synchrony measures have been observed in MCI and AD patients who transitioned from MCI to AD [13,70,103,104,131,134,153,161].

A recently developed approach, termed stochastic event synchrony, characterizes the interaction between "events" in two time series [34]. Typically, in EEG, these "events" include spikes or transient oscillatory components [11,12,22,109]. Significant decreases in synchrony have been noted in MCI and AD patients using these measures [36]. Stochastic event synchrony and ffDTF have also been shown to have high discrimination in separating MCI and AD EEG records from NC records when used in conjunction [36].

Derived from information theory, mutual information and Kullback-Leiber divergence measures have been applied toward the analysis on EEG synchrony in MCI and AD. Inter-channel mutual information has been observed to be significantly reduced in AD patients compared to NCs [71]. No significant differences between MCI and NC EEG have been reported based on observations of mutual information of Kullback-Leiber divergence [36]. See Chapter 4 for more on the mathematical theory of mutual information.

Various synchrony measures have been used to construct macroscopic network models of the brain using EEG where each electrode serves as a node and synchrony measures determine connections between nodes. Typically a threshold is applied to determine if a synchrony measure between any two channels is significant (included in the graph). If a synchrony measure fails the threshold criterion, the connection between those two nodes is severed (excluded from the graph) [37]. The properties of the resulting graph can be analyzed using graph theory and used as measures of synchrony. In effect, this is a

method for deriving features of features with the objective being a reduction in the feature space. For example, a total of 435 unique inter-channel synchronization measures for an EEG record with 30 channels may be summarized using a handful of graphical network features [90].

A graphical network's complexity is typically quantified in terms of statistical randomness and regularity among the network's connections [145]. More recent research has demonstrated that the behavior in complex systems (e.g., the human brain) is shaped by the interactions among the network's constituent elements [27]. Brain networks characteristically demonstrate small-world behavior, or clustering [17,47,112,129,133]. Small-world behavior is the occurrence of highly connected clusters of nodes within a larger network [154]. EEG records of MCI and AD patients have demonstrated weaker small-world network characteristics, or decreased clustering, compared to NCs [55,130].

Datasets Used in Analyses

Event-Related EEG for TBI (WM1 Dataset)

The EEG data for TBI participants used in the studies presented in this work were originally collected by Vagnini *et al.* [147]. The corresponding normal participants were required to have no medical history of TBI. Records obtained from hospitals revealed that the TBI participants had sustained their injuries an average of 13 years (SD 7.2 years) prior to the data collection, had an average GCS score of 8.7 (SD 2.9) at the time of injury, and an average loss of consciousness of 7.2 days (SD 12 hours). CT and MRI scans indicated moderate to severe injury in a variety of regions in the brain, including brain stem, frontal, temporal, parietal, and occipital lobes in both the right and left hemispheres.

Participants were given a series of tests to evaluate their reading comprehension, writing abilities, and their depressive states. Specifically these tests included the Weschler Test of Adult Reading (WTAR) and the Beck Depression Inventory II (BDI-II). There were no statistically significant differences between the TBI and normal controls in regards to reading and writing abilities or depressive state. Participants were also well matched in regards to age, gender, education level, and marital status; see Table 1.1.

Participants were connected to 32-channel EEG caps using a Neuroscan™ SynAmp II system. Recordings were taken during a visual memory recognition ("old-new") task [147]. The memory task consisted of two phases: the study phase and the recognition phase; see Fig. 1.3. During the study phase, participants were initially shown 100 images of common objects for 5 s each and asked to memorize the images. The images were studied for a second time after a short break and the participants were again asked to memorize the images. During the recognition phase, the participants were shown 140 images, 70 of which were from the previously studied (old) set of 100 images, and 70 of which were previously unseen (new) images. EEG recordings were taken during the recognition phase

while the participants were asked to determine whether the images were old or new. Note that the order in which the 140 images were shown was predetermined in a random manner. To avoid expectation effects, interstimulus intervals between images and fixation images (presented between each image) were randomly determined to be 1100 ms, 1300 ms, or 1500 ms. The recognition phase took approximately 9.5 min to complete on average. EEG recordings were sampled at 500 Hz. The 32 EEG channels included 2 ocular channels, which were used to determine the dominant eye blink frequency. Notch filters were used to remove dominant eye blink frequencies and to remove 60 Hz frequencies, which may have been amplified by background electronic devices. A simple 2nd order Butterworth low-pass filter was used to attenuate frequencies greater than 150 Hz.

Only 25 of the 32 channels are used in analyses. The channels not used include the horizontal and vertical ocular channels, HEO and VEO, and channels that were corrupted or missing for one or more participants due to signal loss. Missing channels were those for which no data were recorded. Only three participants had corrupted or missing channels—two NC, one TBI—but this led to a total of five channels that could not be included. Thus, analyses are conducted with 25 channels out of the 32 available. The omitted channels included the two ocular channels (HEO and VEO) as well as CZ, CPZ, FZ, FC3, and FC4.

The performance in the memory tests of the normal and TBI participants are presented in Fig. 1.4. The difference in sample means allows for the statistical inference of a linear separability at the population level with 95% confidence. However, due to the large variation in the scores of TBI participants, the performance for each image type allowed for a maximum classification accuracy of only 73.3%. Using the performance on both old and new images as features for a support vector machine model with a quadratic kernel, a leave-one-out cross-validation accuracy of 86.7% was achieved; see Chapter 2 for more information regarding support vector machines and leave-one-out cross-validation. However, one potential concern of using performance-based classification is that a normal participant could purposefully make wrong choices during the memory recognition to reduce his or her performance (malingering) [147]. Collectively, the 30 EEG records (15 TBI, 15 NC) recorded during the old-new working memory task just described are referred to as the first working memory dataset (WM1 Dataset) in later Chapters.

Event- and Non-Event-Related EEG for MCI, AD (WM2 and NER Datasets)

The MCI and AD EEG data used in the studies presented in this work were collected in the laboratory of Dr. Yang Jiang of the Behavioral Science Department and Sanders-Brown Center on Aging at the University of Kentucky (UK) College of Medicine. Participants between the ages of 60 and 90 years were recruited from a study cohort of cognitively normal older adults identified by the Alzheimer's Disease Center (ADC) of the UK College of Medicine. MCI patients were recruited from the Memory Disorders Clinic of the ADC. Normal older participants are screened regularly and when screenings indicate possible cognitive decline they are referred to the ADC's Research Memory Disorders Clinic. MCI and AD participants were diagnosed and recruited by cognitive neurologists Drs. C. Smith and G. Jicha at the UK ADC Clinical Core and from its Research Memory Disorders Clinic.

Table 1.1. Demographic Data WM1 Dataset Participants

Variable	TBI	NC
age	40.5 (11.7)	36.2 (12.2)
education	14.3 (1.9)	15.4 (2.3)
WTAR	105.5 (6.9)	110.3 (11.3)
BDI-II	6.9 (6.3)	5.1 (7.6)
gender	46.7	56.3
race	100	68.8
marital status	53.3	50
n	15	15

means; standard deviations in ( ); WTAR = Weschler Test of Adult Reading; BDI-II = Beck Depression Index II; gender reported in % female; race reported in % white; marital status reported in % single. Data taken from Vagnini *et al.* [147].
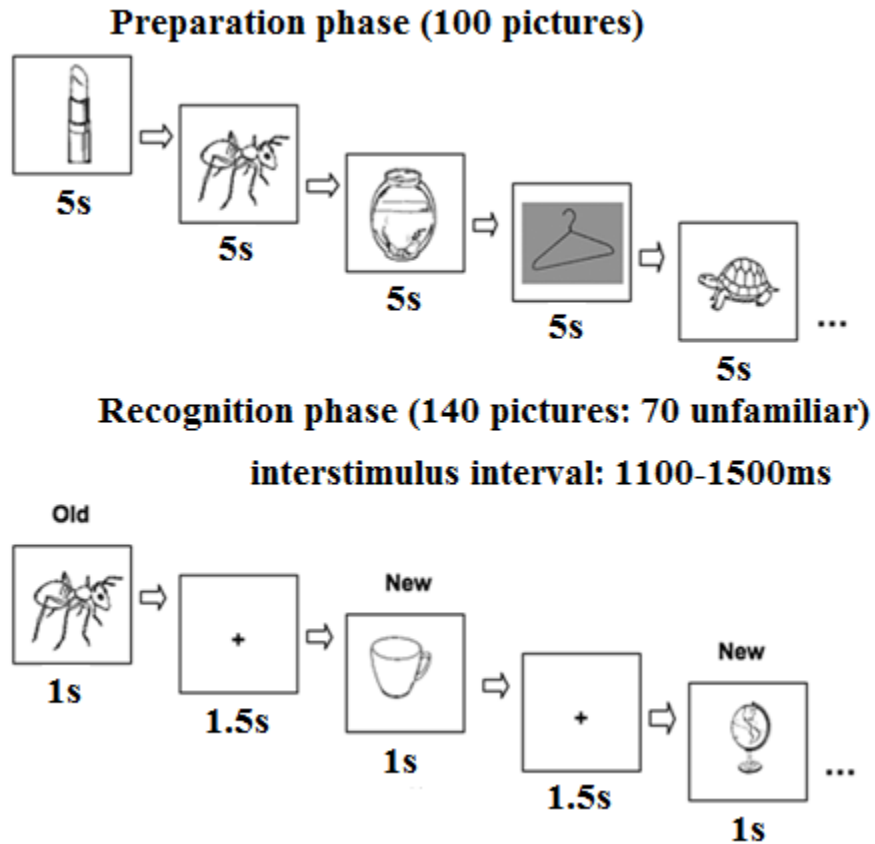
Fig. 1.3. Examples of Images Shown during WM1 Dataset Working Memory Task [147].
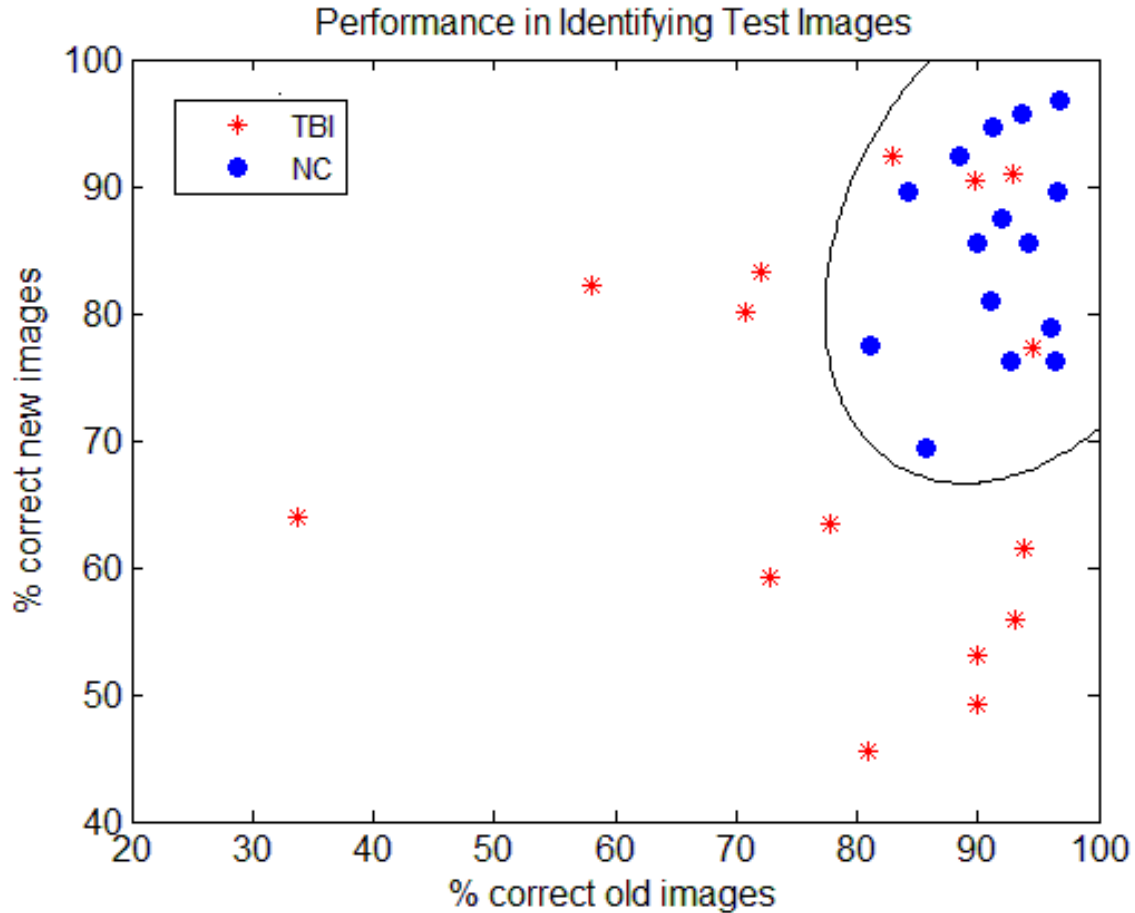
Fig.1.4. Performance of NC and TBI Participants for Working Memory Task [91]. Note the optimal classification boundary determined using a support vector machine model and quadratic kernel function.

A list of neurological assessments used to make MCI and AD diagnoses is provided in Table 1.2 [117].

Participants were screened to exclude active or unstable medical conditions, depression, and other psychiatric disorders, or history of neurologic or neurosurgical conditions. No participants were to have the ApoE4 allele for Alzheimer's risk or to be on any psychoactive medication other than antidepressants. Due to the small number of participants, individuals with the ApoE4 risk factor were excluded in order to have more uniform groups. Systolic hypertension, donepezil, and anti-depressants are known to modulate EEG markers including event-related potentials (ERPs) associated with cognitive functions. These conditions are very common in the population of interest, complicating outright exclusion; however, uncontrolled hypertension or use of sedatives, such as the benziazepines, was basis for exclusion from the study.

All MCI participants belonged to the amnestic MCI subtype. In addition, a few of the MCI participants also presented with executive dysfunction. Differences between single- and multiple-domain MCI subtypes are not he focus of the current study. MCI and early AD participants' EEG data were recorded as soon as possible after diagnoses were made. Two different sets of EEG data were recorded: event-related data recorded during a visual working memory task and non-event-related data recorded during resting states and simple cognitive task.

Event-Related Data Collection (WM2 Dataset)

Event-related EEG was recorded for 17 NC, 16 MCI, and 10 AD participants. Participants were well matched with regards to age, with NC, MCI, and AD participants having mean ages of 75.2 years (SD 4.9 years), 73.9 years (SD 9.5 years), and 76.5 years (SD 5.2 years), respectively. NC participants were 60% female and AD participants were 70% female. MCI participants were only 20% female. Difference in MCI gender was likely due to recruiting and does not reflect population trends.

Participants were connected to 64- or 32-channel EEG caps using a Neuroscan II system (10-20 montage). In either case, only the 32 common channels were recorded. Recordings were taken during a visual working-memory matching task [26]. The matching task consisted of 30 trials with 2-s intervals between trials. During each trial, participants were initially shown an image (sample target) for 3 s and asked to hold the image in mind. Sample target images were outlined in a green border in order to distinguish them. After 1 s, participants were then shown a series of test images. The test images consisted of two repetitions of the original image ("targets"), two similar but different images ("distractors"), and one filler image (target or distractor chosen at random) presented in a randomized order. The number of target versus distractor images presented was also randomized, but equal in occurrence. Thus, a total of 150 test images were shown during all 30 trials, including 75 targets and 75 distractors. Each of the test images was shown for 1 s. To avoid expectation effects, interstimulus intervals between test images were randomly determined to be 900 ms, 1000 ms, or 1100 ms. The entire matching task required approximately 9.8 min to complete on average. EEG recordings were sampled at 500 Hz. The 32 EEG channels included 2 ocular channels, which were used to determine the dominant eye blink frequency. Notch filters were used to remove dominant eye blink frequencies and to remove 60 Hz frequencies, which may have been amplified by background electronic devices. A simple 2nd order Butterworth low-pass filter was used to attenuate frequencies greater than 150 Hz.

Broster *et al.* previously analyzed the data used here in conjunction with a replication of the matching task in order to study the effects of repetition priming in MCI and AD. For data detailing the performance of participants for the matching task, including accuracies and response times, the reader is referred to their work [26].

Collectively, the 43 EEG records (17 NC, 16 MCI, and 10 AD) recorded during the working memory matching task just described are referred to as second working memory dataset (WM2 Dataset) in this document.

Table 1.2. Cognitive Tests and Other Evaluations Used to Make MCI, AD Diagnoses

General Cognitive Measures	Baseline Only
MMSE	National Adult Reading Test
Clinical Dementia Rating (CDR)	**Medical Evaluation**
Memory Domain Measures	Physical exam
WMS Logical Memory I & II	Neurological exam
California Verbal Learning Test	Medical history
Attention/Executive Domain Measures	Medications
Trail Making Tests A & B	Nutritional supplements
WAIS-R Digit Span & Digit Symbol	Food Frequency Questionnaire (FFQ)
Language Domain Measures	**Psychiatric Evaluation**
COWAT	Neuropsychiatric Inventory Questionnaire (NPIQ)
Animal Fluency	Geriatric Depression Scale (GDS)
Vegetable Fluency	**Functional Ability Measures**
Boston Naming	Functional Assessment Questionnaire (FAQ)
Visual/Spatial Domain Measures	SF-36
CERAD Figures	ADCS-ADL
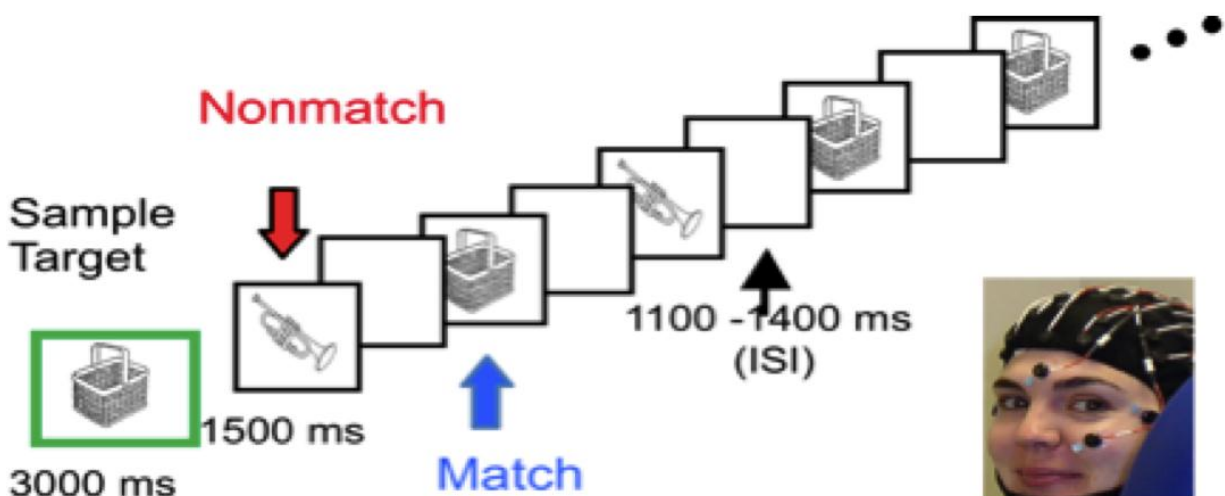
Fig. 1.5. Examples of Images Shown During WM2 Dataset Working Memory Task [26].

Non-Event-Related Data Collection (NER Dataset)

Non-event-related EEG was recorded for 15 NC, 16 MCI, and 17 AD participants. Participants were well matched with regards to age, with NC, MCI, and AD participants having mean ages of 75.7 years (SD 5.5 years), 74.6 years (SD 9.0 years), and 76.7 years (SD 5.2 years), respectively. NC and AD participants were also well matched in regards to gender, with NC and AD participants being comprised of 60% females. MCI participants were only 25% female. Again, the difference in MCI gender was likely due to recruiting and does not reflect population trends.

Participants were connected to 64- or 32-channel EEG caps using a Neuroscan II system (10-20 montage). In either case, only the 32 common channels were recorded. EEG data were recorded under a protocol using three different non-memory-task conditions. These included: (1) resting with eyes open (REO) for 5 min, (2) resting with eyes closed while counting backwards by ones for 10 min while tapping a finger (counting task), and (3) resting with eyes closed (REC) for 10 min, followed by another 5 min of REO. EEG recordings were performed without interruption at the same appointment for each participant. EEG data were acquired at 500 Hz. The 32 EEG channels included 2 ocular channels, which were used to determine the dominant eye blink frequency. Notch filters were used to remove dominant eye blink frequencies and to remove 60 Hz frequencies, which may have been amplified by background electronic devices. A simple 2nd order Butterworth filter was used to attenuate frequencies greater than 200 Hz. In addition, analysis of EEG data examined only frequency components less than 40 Hz.

Collectively, the 48 EEG records (15 NC, 16 MCI, and 17 AD) recorded during the resting states and simple cognitive task just described are referred to as the non-event-related dataset (NER Dataset) in this document.

CHAPTER 2
EVENT-RELATED DISCRIMINATION OF TBI AND MCI
USING TSALLIS ENTROPY

In this Chapter, an exploration of event-related Tsallis entropy measures as potential biomarkers of neurological disease is presented. The approach developed is applied toward the discrimination of TBI and MCI using EEG recorded during working memory tasks. The specific working memory task protocols for TBI and MCI data are similar, but differ in several respects; see Chapter 1 for more details regarding data collection procedures. This Chapter begins with a review of the mathematical theory of communication systems and the definition for an estimator of Tsallis entropy. Next, the methodology for computing event-related Tsallis entropy measures is described. Finally, results obtained for discrimination of TBI vs. NC and MCI vs. NC EEG records are presented and discussed.

Mathematical Theory of Tsallis Entropy

Components of Communication Systems in the Brain

Levels of Communication in the Brain

The mathematical bases of signal theory were originally presented by Shannon in his classic work *The Mathematical Theory of Communication* [120]. In this work, Shannon describes the essential components of any communication system as being: (1) a sender, or originator of the signal; (2) a receiver, or the final destination of the signal; (3) a communication channel, or medium through which the signal can travel (radio and other electromagnetic waves can travel in the absence of a medium); and (4) an encoding of the information contained within the signal. A synthetic example of such a communication system would be the telegraph. The system used to relay information via a telegraph is composed of the telegraph key (the sender) and the telegraph receiver (the receiver) at the other end of the telegraph wire (communication channel). The message sent via the telegraph system is encoded using Morse code.

Communication systems in nature are rarely as simple as the example of the telegraph just given. For example, communication within the brain occurs at the microscopic and macroscopic levels [29,108,125]. At the microscopic level, the method of communication is the interneuronal PSPs and APs. Neurons serve as both senders and receivers of PSPs and APs, with the synaptic gaps between neurons described in Chapter 1 serving as the communication channel by which the PSPs and APs are transmitted from one neuron to another. Previous studies have concluded that the method of encoding of information by PSPs and APs in interneuronal communication is based on the time variation or frequency of occurrence of PSPs and APs [29, 108]. Though the basic means of communication at the microscopic level within the brain is well understood, the amount of

interconnectivity involved in synaptic pathways is currently beyond the ability of modern technology to accurately map [108,125].

The picture becomes even more ambiguous at the macroscopic level of communication within the brain. Communication within the brain at this level involves intra- and inter-regional, time-varying voltages that are recordable by EEG. The brain itself serves as the originator and receiver of the signals, usually with different regions originating and receiving the signals [125]. Each major structural area or "nucleus" of neurons within the brain can serve as both senders and receivers [30]. In the case of EEG, the communication channel includes the brain, skull, soft tissues between different brain structures, and the EEG recording devices themselves.

The Encoding Problem
The method of encoding of time-varying EEG voltages is unknown [125,126]. This makes the translation of the information captured in the signal nearly impossible, a problem often referred to in cognitive neuroscience as the "encoding problem" [125]. The challenge presented in analyzing EEG data lies in the process of estimating the information contained in the signal without knowledge of the method of encoding. A plausible assumption, however, is that the ability of individuals who suffer from neurological disorders to process information is less than that of healthy individuals. Such disparity in information processing by the brain could theoretically be evident in the amount of information present in EEG data recorded during cognitively taxing activities [125].

Estimation of Tsallis Entropy

Classical Shannon Entropy
Information can be defined as that which decreases uncertainty and the basic amount of information in a signal can be defined mathematically in terms of entropy [125]. The classic formula for calculating entropy of a signal, originally proposed by Shannon, is generally known as Shannon entropy and can be calculated using Equation (2.1) [125]:

$$S = \sum_{i=1}^{N} p(x_i) \ln[p(x_i)], \quad (2.1)$$

where x is a random variable with domain N informational symbols (x_1, x_1, ..., x_N) and $p(x_i)$ is the probability of occurrence of information event x_i in the signal. Those familiar with entropy in other scientific applications, such as thermodynamics, may recognize that the formula for Shannon entropy is the same as Gibbs-Boltzmann entropy, which is the measure of disorder in a thermodynamic system [125].

Unfortunately, Shannon entropy has limited validity in application to natural signals, including EEG, because Shannon entropy is based on the assumption that the system being measured is an extensive system. In other words, the total entropy of the system is assumed to be equal to the sum of the entropy present in the system's individual components. This is not the case for the EEG signal acquisition system, which is composed

of the brain, skull, skin, muscles, electrodes, connecting wires, and the data acquisition system used to record measurements. The relationship between the entropy present in these individual components to the entropy of the EEG signal is not known and can change from trial to trial, patient to patient, and is dependent on the equipment used. The EEG recording system, therefore, is more accurately viewed as an intensive system, in which the entropy present in the individual components of the system may be sub- or super-additive in relation to the entropy in the EEG signal [125].

Tsallis Entropy for Intensive Systems

  Fortunately, a formula for estimating the entropy of an intensive system, first proposed by Tsallis, is applicable for analyzing the entropy of EEG and other natural signals. The general formula for Tsallis entropy is presented as Equation (2.2):

$$S_T = \sum_{i=1}^{N} p(x_i) \ln_q \left(\frac{1}{p(x_i)} \right) = \frac{1 - \sum p^q(x_i)}{q - 1}, \quad (2.2)$$

  where the q-logarithm function is defined as:

$$\ln_q(x) \equiv \frac{x^{1-q} - 1}{1 - q}, \forall\, x > 0, q \in \mathbb{R}. \quad (2.3)$$

In particular, $\ln_1(x) = \ln(x)$. The parameter q is a measure of the nonextensivity of the system being measured. Given the relationship presented in Equation (2.2), the amount of information contained within an EEG signal, or the entropy of the signal, can be estimated if the probability of occurrence of the information events within the signal is known.

 Observations of known physical information events in other natural signals provide examples that can be used to estimate the probability of the information events in EEG recordings. Specifically, critical points (local maxima, local minima, and discontinuities) appear to delineate information events in natural signals [125]. Using this observation, an approximation of Tsallis entropy for $q = 2$ was proposed by Sneddon as follows:

$$S_T \approx \hat{S}_T = 1 - \frac{\frac{1}{N} \sum s_i^2}{\sigma^2}, \quad (2.4)$$

where N is the number of bins delineated by local critical points of the signal, s_i^2 is the variance within each of these bins ($i = 1, \dots, N$), and σ^2 is the variance of the entire signal. In the studies presented here, critical points are defined as points where the discrete derivative $(x_{n+1} - x_n)/\Delta t$ equals zero or changes sign from its previous value.

Methodology

Selection of Event-Related Intervals

Visual Stimulus Events

Though the working memory tasks differed for the TBI and MCI data, both tasks included two distinct types of images. As described in Chapter 1, the TBI working memory task was comprised to two phases. The first phase was the study phase, during which participants were shown 100 images and asked to memorize them. The second (recognition) phase, during which EEG was recorded, included the presentation of 140 images, 70 of which had benn presented during the study phase (old, studied images) and 70 of which had not been seen previously (new images). The presentation of each old and new image during the second phase constituted an event. Thus, there were a total of 140 events, 70 corresponding to the presentation of old images and 70 corresponding to the presentation of new images.

The protocol for the MCI working memory task is described in detail in Chapter 1. This working memory task consisted of single phase, comprised of 30 trials. For each trial, participants were presented with a sample target image and asked to memorize the image. The participants were then shown a set of five test images comprised of at least two target images (repetitions of the sample target) and at least two distractor images (images similar to the sample target image but different in some respect). The order of presentation of target and distractor images after each sample target image was randomized. The number of target versus distractor images presented was also randomized, but equal in occurrence. Thus, a total of 150 test images were shown during all 30 trials, including 75 targets and 75 distractors. Each presentation of a target or distractor image was considered an event for a total of 150 events, 75 corresponding to target images and 75 corresponding to distractor images.

Event-Related Intervals

Tsallis entropies are computed for selected visual stimulus events using two discrete intervals, I1 and I2. Here, the I1 interval is selected to be the first 300 ms after an image was shown (0-300 ms), and the I2 interval is selected to be 300 to 800 ms after an image was shown (300-800 ms).

Selection of I1 and I2 intervals is motivated by previous observations of visually evoked EEG responses during short-term memory tasks, including event-related potentials (ERPs), and the desire to have non-overlaying intervals. Neuronal changes in response to a visual stimulus presentation typically occur within 1 s after stimulus onset. An ERP known as P100 is also often referred to a P1 because it is the first positive-going component observed around 100-150 ms after the onset of visual stimuli. It is associated with perceptual difficulty and visual attention [44]. P1 is considered a visually evoked potential (VEP) due to its apparent relationship to visual stimuli. Its amplitude is maximized over the lateral occipital scalp and varies based on the attention paid to visual stimulation.

Similarly, P300 is often referred to as P3 because it is also a positive-going component observed around 300-600 ms after the onset of visual stimuli. P3 is considered to be an endogenous potential, meaning that its amplitude and timing are not related to the type of stimulus but rather the individual's reaction to the stimulus. Its amplitude is typically maximized over the parietal area. Thus, the limits of the I1 and I2 intervals were chosen such that they encompass the possible ranges for the occurrence of P100 and P300 ERPs, respectively.

Event-Related Tsallis Entropy Functionals

Regional Segregation of EEG Electrodes

As discussed in Chapter 1, due to channel corruption and missing data only 25 uncorrupted channels were available for all 30 of the WM1 Dataset's EEG records. The WM2 Dataset did not include any corrupted or missing channels. Thus, there were 30 channels (32 channels excluding the 2 ocular channels) available for WM2 Dataset. Note that the 30 channels available for the WM2 Dataset included the 25 channels available for the WM1 Dataset. These 30 channels are divided into 6 recording regions corresponding to major regions of the cerebral cortex; see Fig. 2.1. The six regions include the central region (posterior frontal electrodes), anterior frontal region, left temporal region, occipital region, parietal region (central and parietal electrodes), and the right temporal region denoted by C, F, L, O, P, and R, respectively. Channels excluded from analysis of the WM1 Dataset are indicated in Fig.2.1.

Tsallis Entropy Functionals

Tsallis entropies are computed for I1 and I2 intervals corresponding to each event for all channels. Tsallis entropies are then averaged for each image type within each scalp region for each event-related interval. These regional averages are termed Tsallis entropy functionals (TEFs). Thus, for the WM1 Dataset, 6 old TEFs and 6 new TEFs are calculated for each of the 2 event-related intervals for a total of 24 TEFs per record. For the WM2 Dataset, 6 target TEFs and 6 distractor TEFs are calculated for each of the 2 event-related intervals for a total of 24 TEFs per record.

Discrimination of EEG Records

The 24 TEFs are used as features for discrimination of TBI vs. NC EEG records (WM1 Dataset) and MCI vs. NC EEG records (WM2 Dataset). Discrimination analyses are performed using support vector machine functions in MATLAB [88]. Feature selection is used to determine which TEFs best discriminate between categories of EEG records. Discrimination accuracy is assessed using leave-one-out cross-validation accuracy.

Leave-One-Out Cross-Validation (LOOCV)

Leave-one-out cross-validation (LOOCV) accuracy is determined as follows. For each record, a support vector machine model is trained using selected features from all other records. The model is then applied to the current record and the resulting categorical determination is recorded. This process is repeated for all records and the LOOCV accuracy is equal to the accuracy of recorded resulting categorical determinations. This is a rigorous
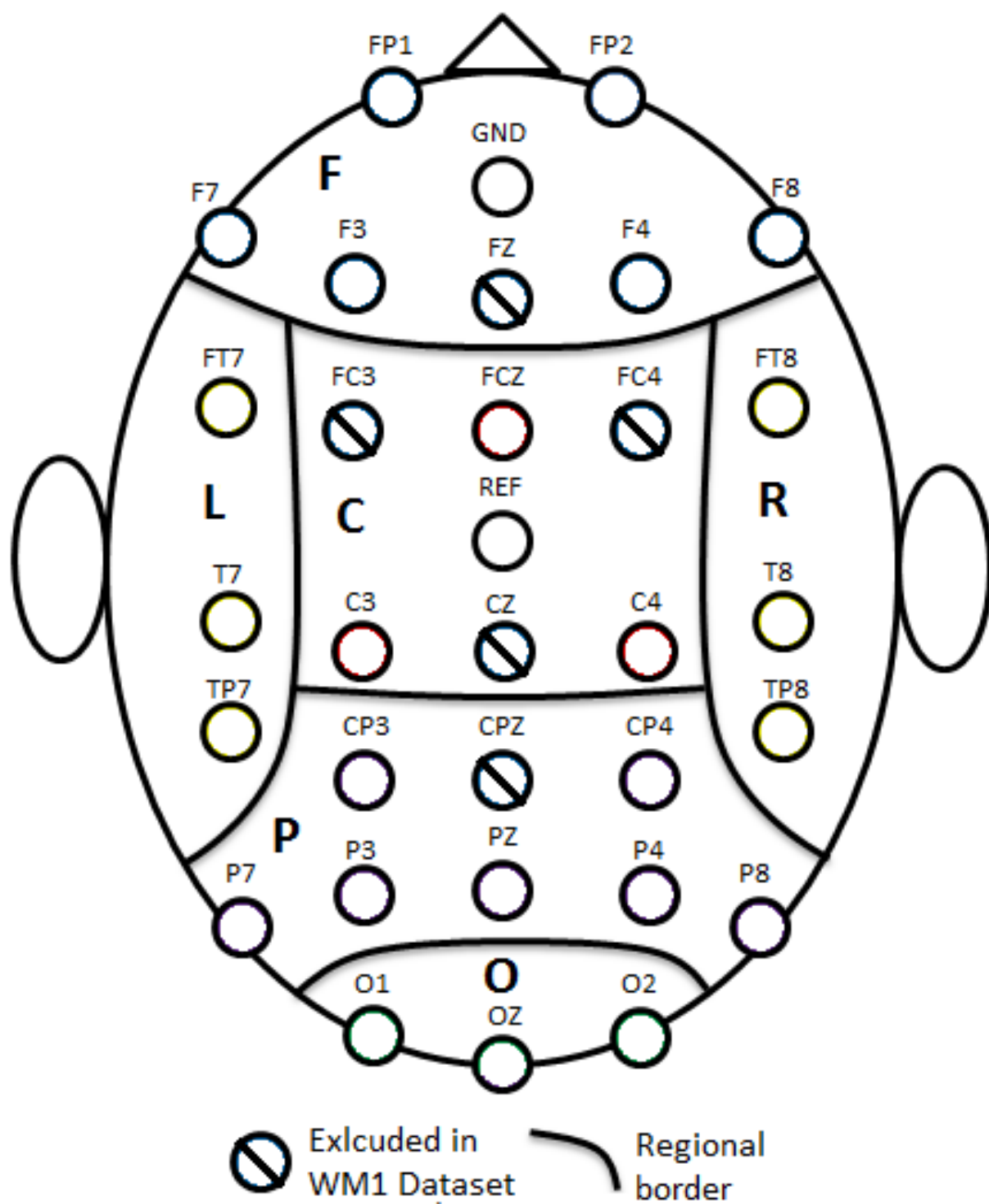
Fig. 2.1. Regional Boundaries for Electrodes. Note channels excluded for WM1 Dataset. C = central; F = frontal; L = left temporal; O = occipital; P = parietal; R = right temporal.

method of cross-validation and helps to ensure that results are more generalizable to other datasets.

Support Vector Machine (SVM)

Support vector machines (SVMs) are a collection of techniques for pattern classification and nonlinear regression. SVMs have been widely applied in machine learning, optimization, statistics, neural networks, functional analysis, etc. The fundamental premise of SVM is to construct a hyperplane in a feature space to serve as the decision surface for separating data from two different categories. For convenience, two theoretical categories are denoted by +1 and -1. The objective in SVM analysis is to maximize the margin between positive and negative examples. Figure 2.2 shows a schematic representation of an optimized separation hyperplane for a 2D feature space. In case patterns are not separable, a nonlinear mapping can be applied to transform input data into a new feature space by means of a kernel function. Then, an optimal hyperplane can be constructed between the two categories in the new feature space. The data vectors that are nearest to the constructed hyperplane in the transformed space are known as support vectors.

SVM analysis is based on the method of structural risk minimization. Consider a train set $\{(x_i, y_i)\}$ for $i = 1, \dots, N$ where input $x_i \ni \mathbb{R}^n$ and the associated output $x_i \ni \{-1, +1\}$. Let φ be a transformation mapping function. The aim is to find a separating hyperplane $\boldsymbol{w} \cdot \boldsymbol{\varphi}(\boldsymbol{x}) + b = 0$ such that $y_i(\boldsymbol{w} \cdot \boldsymbol{\varphi}(x_i) + b) \geq 1 \; \forall \; i$. The optimal separating hyperplane minimizes the cost function $F = (1/2)\boldsymbol{w}^T \cdot \boldsymbol{w}$. This constrained optimization problem can be solved using the method of Lagrange multipliers as present in Equation (3.5):

$$J = \frac{1}{2}\boldsymbol{w}^T \cdot \boldsymbol{w} - \sum_{i=1}^{N} \alpha_i (\, y_i(\boldsymbol{w} \cdot \boldsymbol{\varphi}(x_i) + b) - 1), \quad (3.5)$$

where the nonnegative auxiliary variables α_i are known as Lagrange multipliers. Solving this optimization problem using techniques such as a quadratic program leads to an SVM.

For a given testing vector $\boldsymbol{x}$, an inner-product kernel is defined as $K(\boldsymbol{x}, x_i) = \boldsymbol{\varphi}^T(\boldsymbol{x})\boldsymbol{\varphi}(x_i)$. Based on the form of the inner-product kernel, different vector machines can be generated, including linear learning machines, polynomial learning machines, and radial basis function machines. In the Tsallis entropy analyses presented in this work SVM analyses are performed using quadratic kernel functions and SVM functions in MATLAB [88]. The cost parameter, used for penalizing misclassifications during optimization, is held constant at unity.

Feature Selection and Statistical Significance

To avoid overfitting and to increase robustness of analysis, *nested* LOOCV loops are used for feature selection and testing of selected features. The inner loop is used to generate a list of suggested combinations of up to eight features using a forward, supervised, high-score method of feature selection. The scores used are LOOCV accuracies
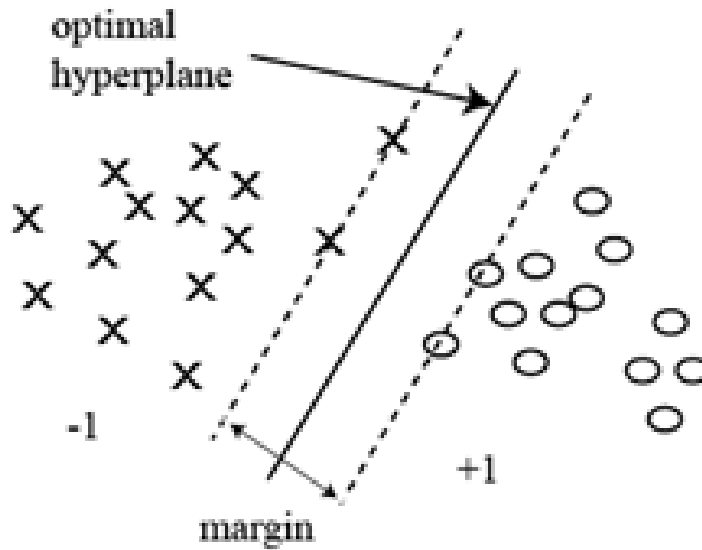
Fig. 2.2. Schematic Representation of SVM Classification of Two Categories Using a Linear Hyperplane in 2D Feature Space. Categories are denoted by +1 and -1, respectively.

of SVM model simulations using a subset of records. The outer loop is used to determine the LOOCV accuracy of suggested features using all available records. For more details on forward, supervised, high-score feature selection, see work by Bishop [21].

The statistical significance of LOOCV accuracies obtained using selected TEFs is estimated using Monte Carlo permutation testing. Specifically, 10,000 permutations of shuffled labels are used to estimate 95% confidence intervals for the probabilities that the LOOCV accuracies obtained are due to chance. The p-values presented are determined using this method. For more on Monte Carlo permutation testing, see work by Thomas and Holmes [143].

Results for Discrimination of TBI and MCI
Using Tsallis Entropy

TBI vs. NC Results

Two-sample student t-distribution tests (unequal variance) are performed on group means of all 24 TEFs in order to determine whether it can be statistically inferred that groups are linearly separable at the population level. Results for the WM1 Dataset are presented in Table 2.1. For the majority of TEFs, differences between group means are significant enough to statistically infer linear separability in the populations. Given the

small sample size, such inference requires large differences between group means and small variation within groups. It should be noted that such tests are dependent on the assumption of representative samples.

A summary of the feature selection results for TBI vs. NC discrimination are presented in graphical form in Fig. 2.3, where a color scale is used to indicate the inclusion of given features in the best 200 performing combinations of features tested in outer loop simulations. For example, 100% would indicate that a given feature is included in all of the best 200 performing combinations; 50% indicates inclusion in half of the 200 best performing combinations; etc. As can be seen in Fig. 2.3, TEFs corresponding to I2 intervals of new image presentation events appear to best discriminate TBI records, most notably in the occipital (O) and right temporal (R) regions. In addition, TEFs corresponding to I2 intervals of old image presentation events for the central (C) and right temporal (R) regions also appear to contribute markedly toward discriminating TBI. TEFs corresponding to I1 intervals do not appear to contribute as significantly to discrimination of TBI.

Ultimately, the four TEFs with the highest inclusivity in the 200 best performing combinations are selected for further analyses. These TEFs are denoted as O_{new}^{I2}, R_{new}^{I2}, C_{old}^{I2}, and R_{old}^{I2}, where letter indicates region, superscript indicates event-related interval, and subscript indicates image type. Combinations of one to four of selected TEFs are tested, where combinations are increased by adding selected TEFs sequentially in order of their relative inclusivity ranking. Results for TBI vs. NC discrimination obtained using selected TEFs are presented in Table 2.2. A maximum LOOCV accuracy of 93.3% (p-value < 4.7716E-4) is achieved using all four selected TEFs.

MCI vs. NC Results

Results for two-sample student t-distribution tests (unequal variance) on TEF group means for the WM2 Dataset are presented in Table 2.3. For all 24 TEFs, differences in MCI and NC group means are significant enough to statistically infer linear separability in the populations. Feature selection results for MCI vs. NC discrimination are presented in graphical form in Fig. 2.4. The format of Fig. 2.4 is analogous to Fig. 2.3 for TBI vs. NC feature selection results. As can be seen in Fig. 2.4, TEFs corresponding to the left temporal (L) region are highly discriminatory for all event-related intervals. Additionally, the most highly discriminatory TEFs are those corresponding to I2 intervals of distractor image presentations in the parietal (P) and frontal (F) regions.

Ultimately, the six TEFs clearly indicated in Fig. 2.4 as being highly discriminatory are selected for further analyses: P_{new}^{I2}, F_{new}^{I2}, L_{new}^{I1}, L_{old}^{I1}, L_{old}^{I2}, and L_{new}^{I2}. Combinations of one to six of selected TEFs are tested, where combinations are increased by adding selected TEFs sequentially in order of their relative inclusivity ranking. Results for MCI vs. NC discrimination obtained using selected TEFs are presented in Table 2.4. A maximum LOOCV accuracy of 81.8% (p-value < 0.0036) is achieved using only the three most highly inclusive TEFs selected via feature selection. The use of additional selected TEFs does not necessarily improve the overall accuracy of the discrimination. This is a phenomenon often

observed in SVM discrimination, which results from the fact that an additional dimension in the feature space can actually result in an optimized hyperplane with inferior accuracy.

Table 2.1. Significance of TBI and NC Group Differences in TEFs

TEFs			
Image/Interval	Region	Group means	P-value
old I1	C	TBI < NC	<0.05
	F	TBI > NC	NS
	L	TBI < NC	<0.15
	O	TBI > NC	<0.05
	P	TBI < NC	NS
	R	TBI < NC	<0.05
new I1	C	TBI < NC	<0.05
	F	TBI > NC	NS
	L	TBI < NC	<0.15
	O	TBI > NC	<0.1
	P	TBI < NC	NS
	R	TBI < NC	<0.05
old I2	C*	TBI < NC	<0.05
	F	TBI > NC	NS
	L	TBI < NC	<0.15
	O	TBI > NC	<0.05
	P	TBI > NC	NS
	R*	TBI < NC	<0.1
new I2	C	TBI < NC	<0.05
	F	TBI > NC	<0.15
	L	TBI < NC	<0.15
	O*	TBI > NC	<0.05
	P	TBI > NC	<0.15
	R*	TBI < NC	<0.1

*TEF selected via feature selection; NS = not significant
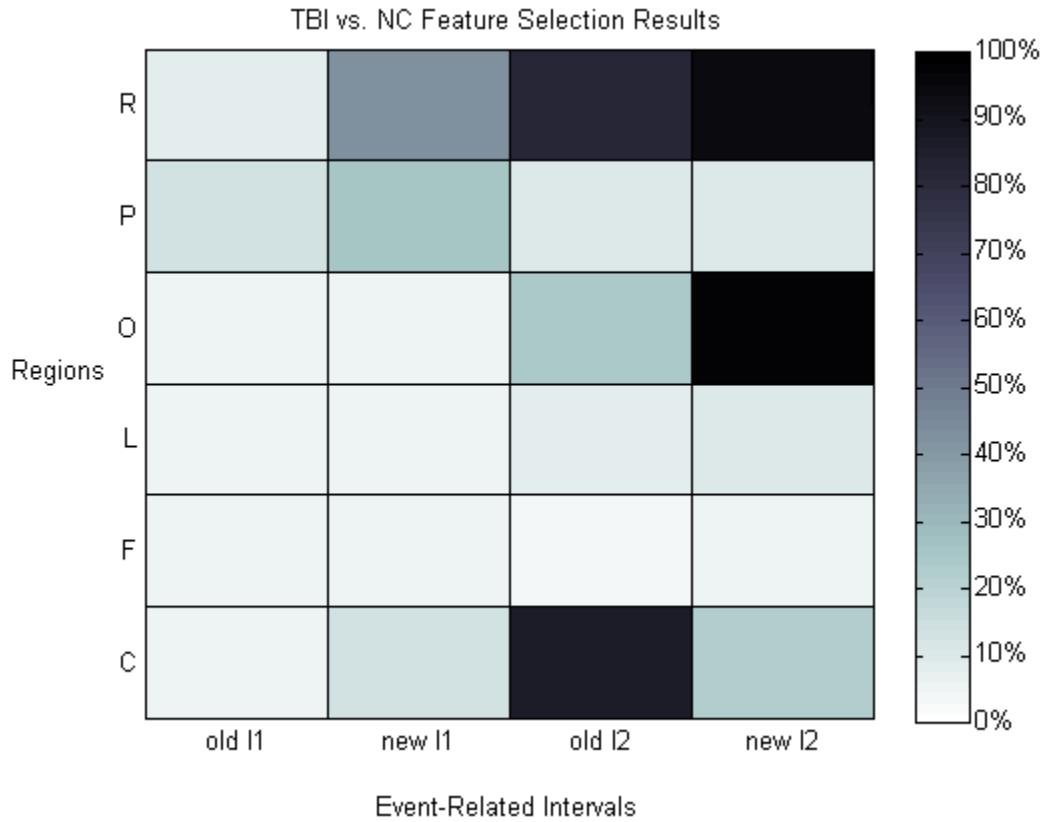
Fig. 2.3. TEF Feature Selection Results for TBI vs. NC Discrimination. Color scale indicates the inclusion of given features in the 200 best performing combinations.

Table 2.2. TBI vs. NC Discrimination Results Using Selected TEFs

# in combn.	TEFs	Acc. (Sens., Spec.)*	95% CI for p-value
1	O_{new}^{I2}	60.0% (86.7%, 33.3%)	(0.2500, 0.2672)
2	$O_{new}^{I2}, R_{new}^{I2}$	80.0% (86.7%, 73.3%)	(0.0022, 0.0044)
3	$O_{new}^{I2}, R_{new}^{I2}, C_{old}^{I2}$	83.3% (80.0%, 86.7%)	(0.0010, 0.0028)
4	$O_{new}^{I2}, R_{new}^{I2}, C_{old}^{I2}, R_{old}^{I2}$	93.3% (100%, 86.7%)	(0, 4.7716E-4)

*acc. = overall LOOCV accuracy; sens. = sensitivity or accuracy in TBI group; spec. = specificity or accuracy in NC group

Table 2.3. Significance of MCI, NC Group Differences in TEFs

TEFs Image/Interval	Region	Group means	P-value
Target I1	C	MCI < NC	<0.05
	F	MCI > NC	<0.1
	L*	MCI < NC	<0.05
	O	MCI < NC	<0.025
	P	MCI < NC	<0.025
	R	MCI < NC	<0.05
Distractor I1	C	MCI < NC	<0.05
	F	MCI > NC	<0.15
	L*	MCI < NC	<0.05
	O	MCI < NC	<0.025
	P	MCI < NC	<0.025
	R	MCI < NC	<0.05
Target I2	C	MCI < NC	<0.05
	F	MCI > NC	<0.1
	L*	MCI < NC	<0.1
	O	MCI < NC	<0.025
	P	MCI < NC	<0.05
	R	MCI < NC	<0.05
Distractor I2	C	MCI < NC	<0.05
	F*	MCI > NC	<0.15
	L*	MCI < NC	<0.15
	O	MCI < NC	<0.025
	P*	MCI < NC	<0.05
	R	MCI < NC	<0.05

*TEF selected via feature selection
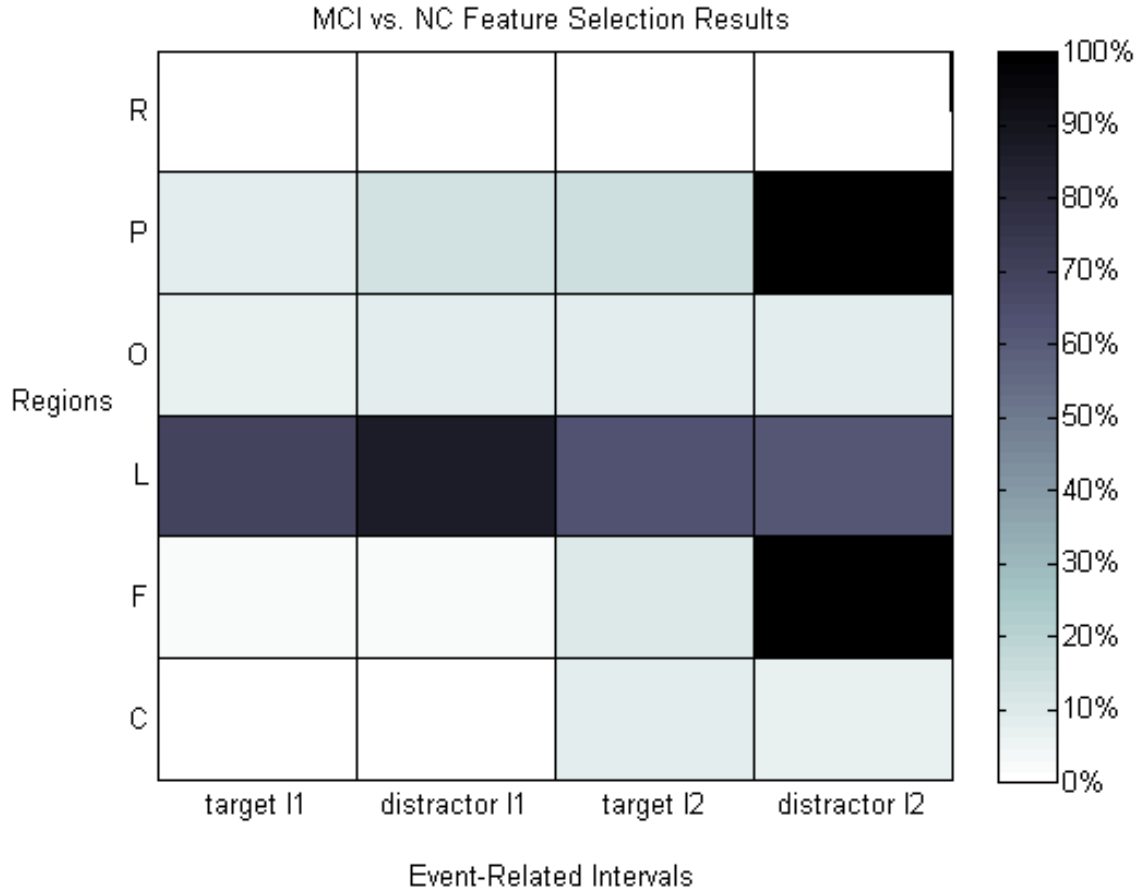
Fig. 2.4. TEF Feature Selection Results for MCI vs. NC Discrimination. Color scale indicates the inclusion of given features in the 200 best performing combinations.

Table 2.4. MCI vs. NC Discrimination Results Using Selected TEFs

# in combn.	TEFs	Acc. (Sens., Spec.)*	95% CI for p-value
1	P_{new}^{I2}	66.7% (81.3%, 52.9%)	(0.0606, 0.0702)
2	$P_{new}^{I2}, F_{new}^{I2}$	63.6% (56.3%, 70.6%)	(0.1363, 0.1501)
3	$P_{new}^{I2}, F_{new}^{I2}, L_{new}^{I1}$	81.8% (81.3%, 82.4%)	(0.0016, 0.0036)
4	$P_{new}^{I2}, F_{new}^{I2}, L_{new}^{I1}, L_{old}^{I1}$	78.8% (81.3%, 76.5%)	(0.0040, 0.0068)
5	$P_{new}^{I2}, F_{new}^{I2}, L_{new}^{I1}, L_{old}^{I1}, L_{old}^{I2}$	81.8% (81.3%, 82.4%)	(0.0015, 0.0035)
6	$P_{new}^{I2}, F_{new}^{I2}, L_{new}^{I1}, L_{old}^{I1}, L_{old}^{I2}, L_{new}^{I2}$	81.8% (81.3%, 82.4%)	(0.0025, 0.0041)

*acc. = overall LOOCV accuracy; sens. = sensitivity or accuracy in MCI group; spec. = specificity or accuracy in NC group

Discussion and Conclusions

Several previous studies have used ERPs to reveal cortical deficits during cognitive tasks among TBI patients in both acute phase and weeks after the incident of injury [50]. Reduced ERP P300 amplitudes have been reported among TBI patients compared to normal controls during cognitive performance tasks (such as memory and attention tasks) [80,147]. En lieu of complex ERP analysis, which generally requires redundant protocols and multiple trials, the method present here using event-related Tsallis entropy demonstrates that analysis of EEG data from a single trial has the potential to successfully discriminate TBI vs. NC. The methodology presented may be used in future investigations to develop a simple and effective means for screening for and possibility evaluating the severity of TBI.

Previous work by Sneddon *et al.* has demonstrated that event-related Tsallis entropy measures of EEG can be used to discriminate MCI from normal controls with accuracy comparable of PET scans. Sneddon *et al.* also reported that their approach appeared to be task specific [126]. The accuracy achieved using the current methodology and working memory matching task is comparable to the accuracy reported by Sneddon *et al.* Sneddon *et al.* investigated the ratio of frontal to parietal event-related Tsallis entropy. Interestingly, parietal and frontal TEFs also appear to be the best discriminating features for MCI in this study, specifically those corresponding to I2 intervals of distractor image presentation events. However, in addition to frontal and parietal TEFs, left temporal TEFs appear to be highly discriminatory regardless of the event-related interval or type of image being presented.

The accuracy in discriminating TBI vs. NC and MCI vs. NC EEG records achieved by the methods presented here likely reflects underlying differences resulting from altered neural mechanisms in TBI and MCI brains during short-term memory recognition tasks. Results indicate that differences between TBI and NC groups' responses are greater for the I2 event-related intervals, which correspond to the endogenous ERP P300. P300 is part of an autonomic response of the visual cortex and visual processing regions of the brain to visual stimuli. The ventral stream of the autonomic pathway of visual information processing in the brain is known to involve the occipital, central, parietal, right temporal, and ultimately frontal lobes [121]. Interestingly, the four TEFs that best discriminated TBI vs. NC EEG records include three of these five regions. The differences observed in the left temporal region of MCI participants may be indicative of an alteration in the organization of visual information processing in the brain due to neurodegeneration

The reported injuries in the TBI participants were widespread across the brain. One limitation of this study is the lack of access to data to allow evaluation of the correlation between the areas of brain injury with TEF results. In a future study, examining participants with acute damage in a known area of the brain may be able to provide further insights into area-specific TBI.

The results in this work demonstrate a strong correlation between Tsallis entropy-based TEFs and the presence of moderate to severe TBI and MCI. Extensive numerical

analyses are carried out to investigate the influences of various parameters, including choice of different event-related intervals. Results suggest that a simple model based on SVM with a quadratic kernel function and the regional, event-related Tsallis entropy measures presented here may be a viable method for the development of a diagnostic screening tool for TBI or MCI. Since EEG is more convenient and much more cost effective than the gold standard imaging modalities, EEG-based techniques would allow for earlier medical intervention and therefore better prognoses for TBI and MCI patients.

The current method cannot be readily applied to the clinical setting since it requires 25-30 EEG channels and takes about 30 min to collect the data (including setup time). A shorter protocol and fewer electrodes would be required for more convenient application. In addition, a larger sample size and new test samples would also be needed to further validate the approach before it could be applied in a private practice setting. The approach presented here may have potential for indexing cognitive deficits due to neurological disorders in other clinical applications.

CHAPTER 3
DISCRIMINATION OF TBI, MCI, AND AD
USING MULTISCALE ENTROPY

In this Chapter, an exploration of event-related Multiscale Entropy (MSE) measures as potential indicators of neurological disease is presented. The approach developed is applied toward the discrimination of TBI, MCI, and AD using EEG recorded during working memory tasks. The specific working memory task protocols for the TBI data and the MCI and AD data are similar, but differ in several respects; see Chapter 1 for details regarding data collection procedures. The Chapter begins with a review of the mathematical theory of MSE. Next, the methodology for computing event-related MSE measures is described. Later, the method is adapted for NER data in order to discriminate MCI and AD using EEG recorded during resting states and a simple cognitive task. Results for working memory and NER analyses are presented and discussed. For MCI and AD discrimination, NER results are compared to results obtained for event-related analyses.

Mathematical Theory of Multiscale Entropy

Premise of MSE Analysis

MSE was first introduced as a tool for quantifying the complexity of a signal when considering several time series derived from the same original data [33]. The premise of MSE is based on the computation of entropy (Tsallis entropy, sample entropy, or approximate entropy) estimated on coarse-grained sequences, each of which represents the system dynamics of the original signal of interest on different time scales (coarseness parameters). Generally, sample entropy is the favored choice for computing the entropy of these coarse-grained time series due to two important attributes: (1) sample entropy is independent of the sequence length (for stationary time series), and (2) can be applied to relatively short, noisy datasets [113].

In order to compute MSE values for a given one-dimensional time series $x = [x_1, \ldots, x_N]$, one must first construct successive coarse-grained time series X^s corresponding scale factors $s = 1, \ldots, M$. This is accomplished as follows. For a given scale s, the original time series x is divided into non-overlapping windows of length s and the values within each window are averaged. This process is summarized by Equation (3.1):

$$X_i^s = \frac{1}{s} \sum_{k=(i-1)s+1}^{si} x_k, \quad (3.1)$$

where $1 \leq i \leq N/s$ and subscripts denote elements in the time series vectors. It should be readily apparent from the definition provided in Equation (3.1) that the coarse-grained times series X^1 corresponding to scale factor $s = 1$ is simply the original signal x.

Moreover, the length of each coarse-grained time series is s times shorter than the original signal.

Computing Sample Entropy

Having constructed the coarse-grained time series from the original signal, the sample entropy of each is computed. Sample entropy measures the negative of the logarithmic conditional probability that sets of patterns that are "close" to each other (within a tolerance r) for m contiguous points remain similar at the next point (also "close" for m + 1 data points). Note that self-matches are not included in calculating the probability. The more irregular the data, the larger the sample entropy value will be (sample entropy is non-negative) [114]. A code for computing sample entropy is provided below. See also work by Richman and Moorman, Costa *et al.*, or Abásolo *et al.* [2,32,113].

```
% code for computing sample entropy
X = N x 1 time series
A = m x 1 vector of zeros % number of matches of length 1,…,m
B = m x 1 vector of zeros % number of matches of length 1,…,m
                         % excluding last point
C = N x 1 vector of zeros
D = N x 1 vector of zeros
for i = 1,…,N-1
    for j = 1,…,N-i
        k = i + j;
        if |X(k)-X(i)| < r %tolerance test
            D(j) = C(j) + 1;
            for n = 1,…,min[m,D(j)]
                A(n) = A(n) + 1;
                if k < N
                    B(n) = B(n) + 1;
                end
            end
        else
            D(j)=0;
        end
    end
    for j = 1,…,N-i
        C(j)=D(j);
    end
end
probability = A(m) / B(m-1);
sample entropy = -log(probability);
```

The values chosen for m and r are critical for the performance of MSE. Comparisons between time series can only be made when time series are the same length and values for m and r are constant. In order to avoid significant contribution to sample entropy due to noise, r must be greater than most of the noise in the original signal. In addition, if the tolerance level is set too low, estimation of sample entropy may fail (due to division by zero in computing probability) [42]. Typically, the accuracy and confidence for sample entropy improves as the tolerance r is increased and the length of matches m decreases (thereby increasing the number of matches of length m and m + 1) [82].

It is often convenient to normalize the tolerance by the standard deviation of the original time series [32]. MSE profiles are sensitive to both variance and entropy because the effective filter, r, is fixed but not normalized for the estimation of sample entropy on scales $s > 1$ [97]. However, the entropy of a sequence depends both on its variance and correlation properties [33]. Furthermore, there is no straightforward relationship between variance and entropy for non-trivial signals [32,42]. Thus, the tolerance should not be normalized for each coarse-grained time series because the changes in variance contain information about the entire original signal [32].

Previous researchers have applied MSE to the study of background activity of EEG in patients with AD [2,42]. These previous studies used the values m = 1 and r = 0.25 times the standard deviation of the original signal. These same values for m and r are used in computing MSE in this work.

Methodology

Selection of Event-Related Intervals

Working Memory Datasets
 The choice of events for both the TBI working memory dataset (WM1 Dataset) and the MCI and AD dataset (WM2 Dataset) are the same as described in Chapter 2 for event-related Tsallis entropy analyses. Thus, a total of 140 events—70 corresponding to presentation of old images and 70 corresponding to presentation of new images—are present in the WM1 Dataset. For the WM2 Dataset, a total of 150 events are present—75 corresponding to the presentation of target images and 75 corresponding to the presentation of distractor images. For each event, event-related intervals of 1 s are examined (0-1000 ms after presentation of image). The chosen window length is based on previous studies that VEPs tend to occur within 1 s after the presentation of visual stimuli [44]. See Chapter 2 for more information regarding common VEPs.

Non-Event-Related Dataset
 For the non-event-related dataset (NER Dataset), which did not contain any events corresponding to the presentation of external stimuli, pseudo-events are defined as non-overlapping windows of EEG. For simplicity of comparison between event- and non-event-

related results, a window length of 1 s is chosen for NER pseudo-events. Previous studies that have investigated the transient, nonstationary nature of EEG, have also noted that the current behavior of EEG is relatively independent of EEG behavior 1 s previous. In other words, the majority of quasi-stationary segments in EEG (pseudo-events) have been observed to have durations less than 1 s [74].

As described in Chapter 1, the NER Dataset consisted of three separate protocol conditions: the REO condition, the counting task, and the REC condition. For each protocol condition, samples of 2 min duration are extracted for analyses. Given the definition of pseudo-events provided above, each 2-min sample contained 120 non-overlapping, 1-s pseudo-events.

MSE Deviation Measures

Deviations of Entropy-vs.-Scale (E-s) Curves
For both MW1 and WM2 Datasets, MSE entropy-vs.-scale (*E-s*) curves are computed for selected visual stimulus events using intervals of 1 s duration (0-1000 ms after presentation of images). For the NER Dataset, for which no events were present, non-overlapping, pseudo-events intervals of 1-s duration are examined. MSE *E-s* curves are computed for each pseudo-event.

MSE values are calculated for scales *s* = 1,...,5 and entropy values are averaged across events for each scale, channel, and image type. Thus, for the event-related datasets WM1 and WM2, two *E-s* curves are computed for each channel: one corresponding to each image type (old/new for WM1 Dataset, target/distractor for WM2 Dataset). For the NER Dataset, only one *E-s* curve is calculated for each channel; however, this procedure is repeated for each of the three protocol conditions.

Average *E-s* curves are computed for each group (TBI, MCI, AD, and NC) of EEG records. Thus, for the WM1 Dataset, TBI and NC average *E-s* curves are computed for each channel and image type (e.g., FP1 old images, FP1 new images, etc.). For the WM2 Dataset, AD, MCI, and NC average *E-s* curves were computed for each channel and image type (e.g., FP2 target images, FP2 distractor images, etc.). For the NER Dataset, AD, MCI, and NC average *E-s* curves are computed for each channel, for each protocol condition (e.g. REO F3, counting task F3, REC F3, etc.).

Deviations of participants' individual *E-s* curves from the group average *E-s* curves are computed for each scale. See Fig. 3.1 for an illustration of the deviations (*D*) for an example participant's data. For the WM1 Dataset, a ratio of the average absolute deviation of from the TBI average curve to the NC average curve is computed for each channel and image type. The formula for these ratios is presented in Equation (3.2):

$$R_C^{Im} = \frac{\frac{1}{5}\sum_{s=1}^{N} D_s^{TBI}}{\frac{1}{5}\sum_{s=1}^{N} D_s^{NC}} = \frac{\sum_{s=1}^{5} D_s^{TBI}}{\sum_{s=1}^{5} D_s^{NC}}, \quad (3.2)$$

where Im denotes the image type (old/new), C denotes the channel (e.g., FP1, FP2, etc.), and D_s^{group} denotes absolute deviation in entropy of the participant from group (TBI/NC) average entropy at scale s; see Fig. 3.1 (a)-(b) for illustration of how deviation is determined for the WM1 Dataset for a given channel and image type. The ratios R_C^{Im} are later used as features in SVM models for discrimination of TBI and NC EEG records.

Similar ratios are computed for the WM2 Dataset; however, the three groups of EEG records in the WM2 Dataset provide three binary classification problems: (1) MCI vs. NC, (2) AD vs. NC, and (3) MCI vs. AD. One ratio is computed for each binary classification problem, as presented in Equations (3.3)—(3.5):

$$_{NC}^{MCI}R_C^{Im} = \frac{\sum_{s=1}^{5} D_s^{MCI}}{\sum_{s=1}^{5} D_s^{NC}}, \quad (3.3)$$

$$_{NC}^{AD}R_C^{Im} = \frac{\sum_{s=1}^{5} D_s^{AD}}{\sum_{s=1}^{5} D_s^{NC}}, \quad (3.4)$$

$$_{AD}^{MCI}R_C^{Im} = \frac{\sum_{s=1}^{5} D_s^{MCI}}{\sum_{s=1}^{5} D_s^{AD}}, \quad (3.5)$$

See Fig. 3.1 (c)-(d) for illustration of how deviation is determined for the WM2 Dataset for a given channel and image type. The ratios $_{NC}^{MCI}R_C^{Im}$, $_{NC}^{AD}R_C^{Im}$, $_{AD}^{MCI}R_C^{Im}$ are later used as features in SVM models for the binary discrimination problems MCI vs. NC, AD vs. NC, and MCI vs. AD, respectively.

For the NER Dataset, ratios are computed for each channel and protocol condition. As was the case for the WM2 Dataset, the three groups of EEG records provide three binary discrimination problems. Thus, three different ratios are computed for each protocol condition corresponding to the particular binary discrimination problem. The formulas for these ratios are presented in Equations (3.6)—(3.8):

$$_{NC}^{MCI}R_C^{Pr} = \frac{\sum_{s=1}^{5} D_s^{MCI}}{\sum_{s=1}^{5} D_s^{NC}}, \quad (3.6)$$

$$_{NC}^{AD}R_C^{Pr} = \frac{\sum_{s=1}^{5} D_s^{AD}}{\sum_{s=1}^{5} D_s^{NC}}, \quad (3.7)$$

$$_{AD}^{MCI}R_C^{Pr} = \frac{\sum_{s=1}^{5} D_s^{MCI}}{\sum_{s=1}^{5} D_s^{AD}}, \quad (3.8)$$

where Pr denotes the protocol condition (REO, counting task, REC); see Fig. 3.1 (e)-(g) for illustration of how deviation is determined for the NER Dataset for a given channel and protocol condition. The ratios $_{NC}^{MCI}R_C^{Pr}$, $_{NC}^{AD}R_C^{Pr}$, $_{AD}^{MCI}R_C^{Pr}$ are later used as features in SVM

models for the binary discrimination problems MCI vs. NC, AD vs. NC, and MCI vs. AD, respectively.

As discussed in Chapter 1, due to channel corruption and missing data only 25 uncorrupted channels were available for all of the WM1 Dataset's EEG records. Both the WM2 Dataset and NER Dataset did not include any corrupted or missing channels. Thus, there were 30 channels (32 channels excluding the 2 ocular channels) available for both datasets containing MCI and AD EEG records. Note that the 30 channels available for the WM2 and NER Datasets included the 25 channels available for the WM1 Dataset. Channels excluded from analysis of the WM1 Dataset are indicated in Fig. 2.1.

Since ratios are computed on an individual channel basis, there are a total of 50 ratios for the WM1 Dataset—25 for old images and 25 for new images; 60 ratios for each binary discrimination problem for the WM2 Dataset—30 for target images and 30 for distractor images; and 90 ratios for each binary discrimination problem for the NER Dataset—30 for the REO condition, 30 for the counting task, and 30 for REC condition.

Discrimination of EEG Records

Feature selection is used to determine which features best discriminate between groups of EEG records. To avoid overfitting and to increase robustness of analysis, *nested* LOOCV loops are used for feature selection and testing of selected ratios. The inner loop generates a list of suggested combinations of ratios using a forward, supervised, high-score feature selection method where combinations are scored using LOOCV accuracy of SVM model predictions based on a smaller subset of records. The outer loop then determines the LOOCV accuracy of the combinations of ratios suggested by the inner loop for all records. Specifically, combinations of up to six channels/ratios are tested. The contribution of individual ratios is assessed based on how often they appear in the best 200 performing combinations tested in the outer loop simulations. A set of ratios is then selected based on relative inclusivity in the best 200 performing combinations. All SVM simulations are performed using quadratic kernel functions and the cost coefficient is held constant at unity. See Chapter 2 for more details concerning LOOCV and SVM.

The statistical significance of LOOCV accuracies obtained using selected ratios is evaluated using Monte Carlo permutation testing. Ten thousand permutations of shuffled labels are used to estimate 95% confidence intervals for the probabilities that the LOOCV accuracies obtained are due to chance. The p-values presented are determined using this method. For more information regarding Monte Carlo permutation testing see work by Thomas and Holmes [143].
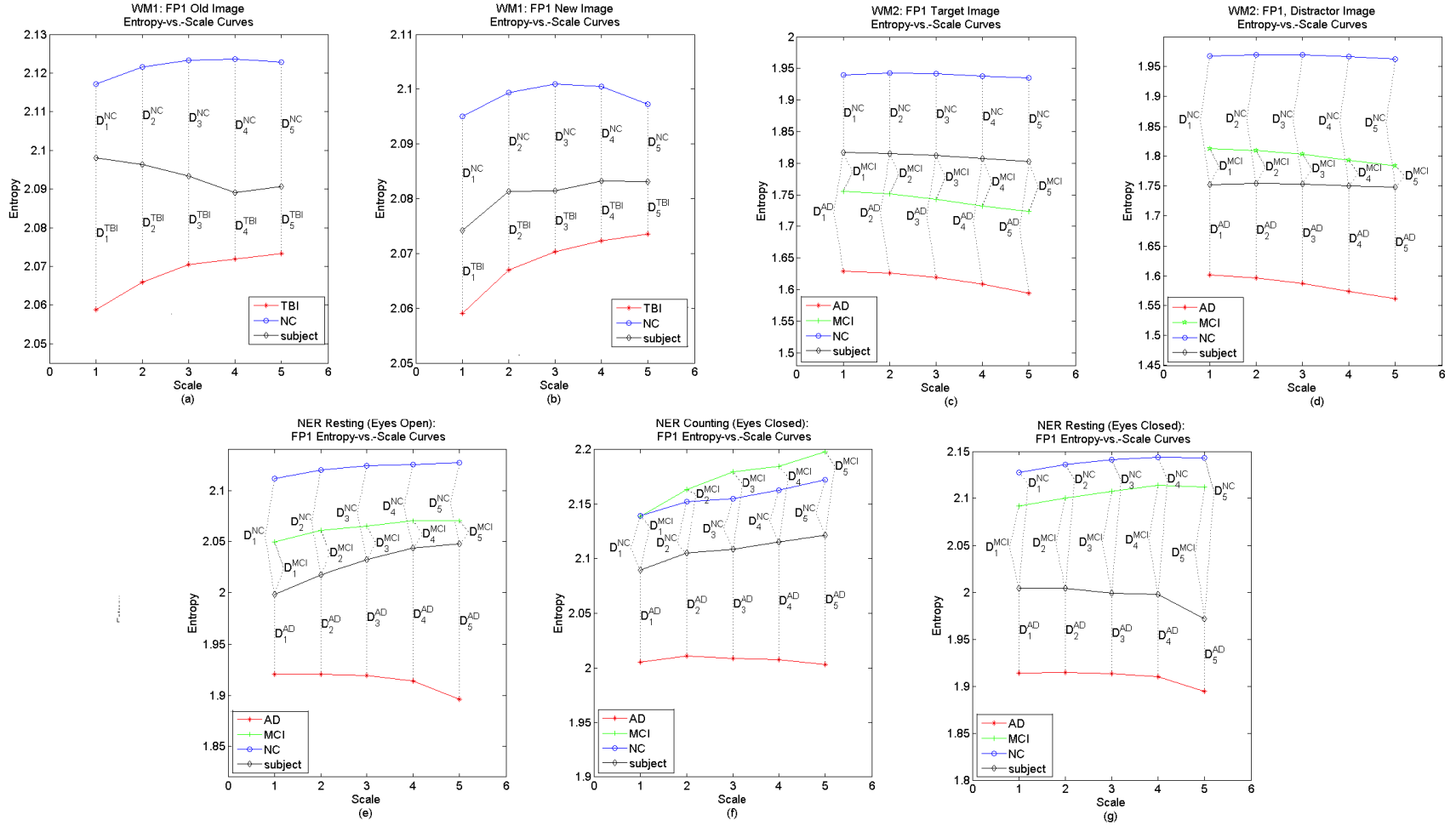
Fig. 3.1. Illustration of MSE Deviation from Average *E-s* Curves. (a) WM1 Dataset old images; (b) WM1 Dataset new images; (c) WM2 Dataset target images; (d) WM2 Dataset distractor images; (e) NER Dataset resting with eyes open condition; (f) NER Dataset counting with eyes closed condition; NER Dataset resting with eyes closed condition. All plots are for channel FP1. Here, D^{NC} denotes deviation from NC average curve; D^{TBI} denotes deviation from TBI average curve; and D^{MCI} denotes deviation from MCI average curve; D^{AD} denotes deviation from AD average curve.

44

Results for Discrimination of TBI, MCI, and AD
Using MSE Ratios

TBI vs. NC Working Memory Results

TBI vs. NC LOOCV discrimination accuracies for individual ratios are presented in a graphical format in Fig. 3.2. The color scale indicates the accuracy. As demonstrated in the figure, accuracies of 70-80% are possible using only the ratios of relative distance between *E-s* curves of individual channels. For old images, there appears to be large differences in the *E-s* curves for channels in the posterior parietal and frontotemporal regions of the scalp. For new images, the largest differences are observed in the channels of the central region of the scalp; see Fig. 2.1 for general regional scalp boundaries.

A summary of the feature selection results is presented in Fig. 2.3, where a color scale is used to indicate the inclusion of given features in the 200 best-performing feature combinations. For example, 100% would indicate that a given ratio is included in all of the 200 best performing feature combinations; 50% indicates inclusion in half of the 200 best performing feature combinations; etc. As can be seen in Fig. 3.3, five to six ratios are clearly highlighted as being highly discriminatory (highly inclusive). The five ratios with greatest inclusivity are selected and tested in combination using a quadratic SVM model. Specifically, these ratios are, in descending rank of performance, R_{P4}^{old}, R_{P7}^{new}, R_{C4}^{old}, R_{O1}^{old}, and R_{PZ}^{old}. The results are summarized in Table 3.1. An accuracy of 93.3% (p-value <4.910E-6) is achieved using the five selected ratios in combination. Recall that the 95% confidence intervals for p-values presented in Table 3.1 for LOOCV accuracies are estimated using Monte Carlo permutation testing.

Table 3.1. TBI vs. NC Discrimination Results Using Selected MSE Ratios

# in combn.	Ratios	Acc. (Sens., Spec.)*	95% CI for p-value
1	R_{P4}^{old}	73.3% (73.3%, 73.3%)	(0.0293, 0.0359)
2	R_{P4}^{old}, R_{P7}^{new}	83.3% (73.3%, 93.3%)	(0.0004, 0.0011)
3	R_{P4}^{old}, R_{P7}^{new}, R_{C4}^{old}	80.0% (73.3%, 86.7%)	(0.0021, 0.0043)
4	R_{P4}^{old}, R_{P7}^{new}, R_{C4}^{old}, R_{O1}^{old}	90.0% (86.7%, 93.3%)	<1.115E-4
5	R_{P4}^{old}, R_{P7}^{new}, R_{C4}^{old}, R_{O1}^{old}, R_{PZ}^{old}	93.3% (86.7%, 93.3%)	<4.910E-6

*acc. = overall leave-one-out cross-validation accuracy; sens. = sensitivity or accuracy in TBI group; spec. = specificity or accuracy in NC group
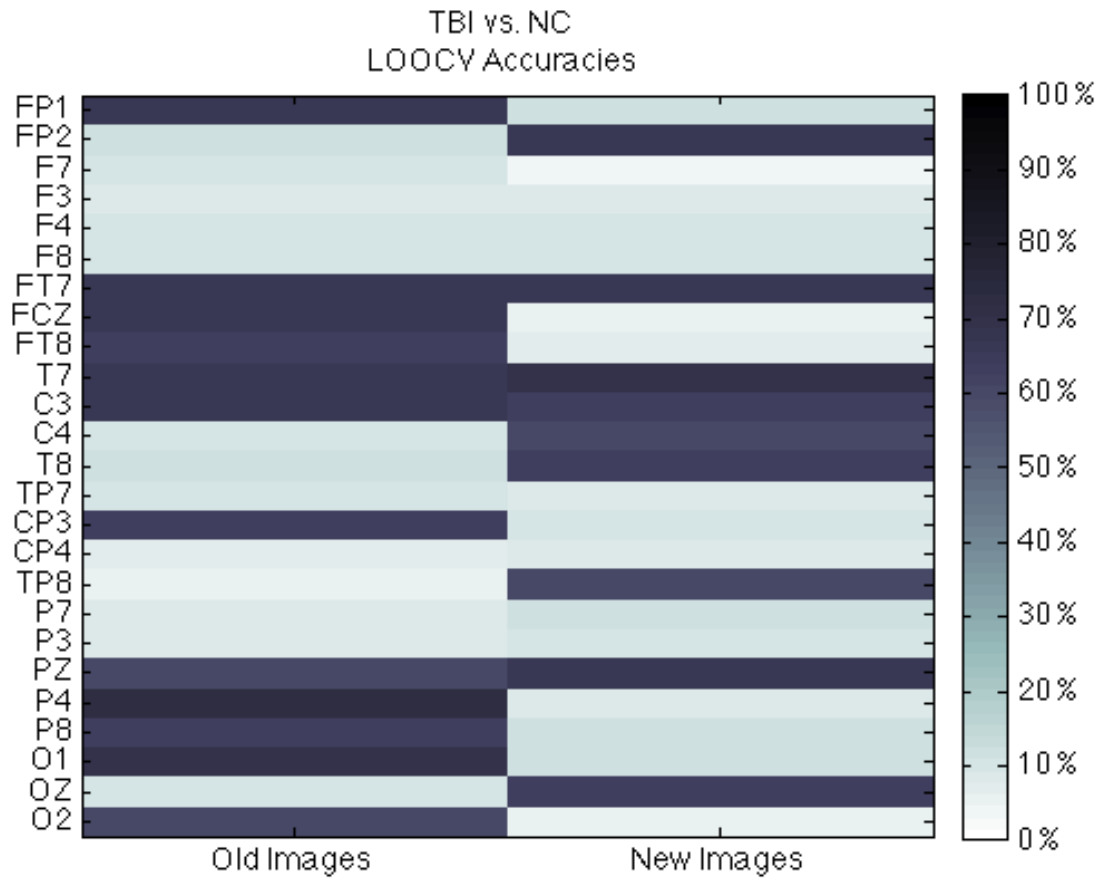
Fig. 3.2. TBI vs. NC LOOCV Accuracies for MSE Ratios. As can be seen in the figure, for old images, the majority of differences are observed in channels of the posterior parietal and frontotemporal regions. For new images, the differences are more widespread.

MCI and AD Working Memory Results

MCI vs. NC

MCI vs. NC working memory LOOCV discrimination accuracies for individual ratios are presented in a graphical format in Fig. 3.4. Accuracies of 60-75% are possible using only the ratios of the average relative distance to MCI and NC *E-s* curves for individual channels. For target images, the majority of differences are observed in channels of the occipital, frontal, and central regions. For distractor images, differences are concentrated in channels of the central and frontal regions.

The feature selection results are presented in Fig. 3.5, where a color scale is used to indicate the inclusion of given features in the 200 best-performing feature combinations. Five ratios are clearly highlighted in Fig. 3.5 as being highly discriminatory (highly inclusive). Note that target image ratios of channels in the frontal and anterior parietal regions appear to best discriminate MCI and NC participants. The five highlighted ratios are

Fig. 3.3. MSE Feature Selection Results for TBI vs. NC. Color scale indicates the inclusion of given features in the 200 best performing combinations for the given protocol condition.

selected and tested in combination using a quadratic SVM model. Specifically, these ratios are, in descending rank of performance, ${}^{MCI}_{NC}R^{target}_{FP2}$, ${}^{MCI}_{NC}R^{target}_{CPZ}$, ${}^{MCI}_{NC}R^{target}_{CP4}$, ${}^{MCI}_{NC}R^{target}_{F3}$, and ${}^{MCI}_{NC}R^{target}_{F7}$. Note that only ratios for target images are selected. The results are summarized in Table 3.2. An accuracy of 87.9% (p-value <1.322E-4) is achieved using the first four selected ratios. Confidence intervals for p-values are estimated using Monte Carlo permutation testing

AD vs. NC

　　　AD vs. NC working memory LOOCV discrimination accuracies for individual ratios are presented in a graphical format in Fig. 3.6. As shown in Fig. 3.6, accuracies of 60-80% are possible using only the ratios of the average relative distance to AD and NC *E-s* curves for individual channels. As can be seen in Fig. 3.6, for target images, the majority of differences are observed in channels of the occipital, frontal, and central regions. For distractor images, differences are observed in channels of the central and frontal regions.

The feature selection results are presented in Fig. 3.7. The color scale indicates the inclusion of given features in the 200 best-performing feature combinations. Note that only two ratios are highlighted and the majority of ratios have poor inclusivity. Thus, the feature selection process is unsuccessful in suggesting a robust set of ratios for discrimination analyses. Instead, the five ratios with the best performance on an individual basis (Fig. 3.6) are selected. Specifically, these ratios are, in descending rank of performance, $_{NC}^{AD}R_{F8}^{target}$, $_{NC}^{AD}R_{F3}^{distract}$, $_{NC}^{AD}R_{C4}^{distract}$, $_{NC}^{AD}R_{CP4}^{distract}$, and $_{NC}^{AD}R_{FC4}^{target}$. LOOCV discrimination results are summarized in Table 3.3. An accuracy of 88.9% (p-value <2.886E-5) is achieved using the first two selected ratios. The results displayed in Table 3.3 are a great illustration of the fact that the use of additional features does not necessarily improve the performance of an SVM classifier. Confidence intervals for p-values are estimated using Monte Carlo permutation testing.

AD vs. MCI

Results for AD vs. MCI working memory LOOCV discrimination of individual ratios are presented in a graphical format in Fig. 3.8. Accuracies of 70-80% are possible using only the ratios of the average relative distance to AD and MCI *E-s* curves for individual channels. As can be seen in the figure, high accuracies are achieved using ratios from various regions of the scalp for both target and distractor images.

Figure 3.9 presents the feature selection results, where a color scale is used to indicate the inclusion of given features in the 200 best-performing feature combinations. Five ratios are clearly highlighted in Fig. 3.9 as being highly discriminatory (highly inclusive). These channels are located in the frontal and parietal regions of the scalp. The five highlighted ratios are selected and tested in combination using a quadratic SVM model. Specifically, these ratios are, in descending rank of performance, $_{MCI}^{AD}R_{F7}^{target}$, $_{MCI}^{AD}R_{FP2}^{distract}$, $_{MCI}^{AD}R_{F8}^{target}$, $_{MCI}^{AD}R_{P4}^{target}$, and $_{MCI}^{AD}R_{P7}^{target}$. The results are summarized in Table 3.4. An accuracy of 92.3% (p-values <4.910E-6) is achieved using the first four selected ratios. Confidence intervals for p-values are estimated using Monte Carlo permutation testing.
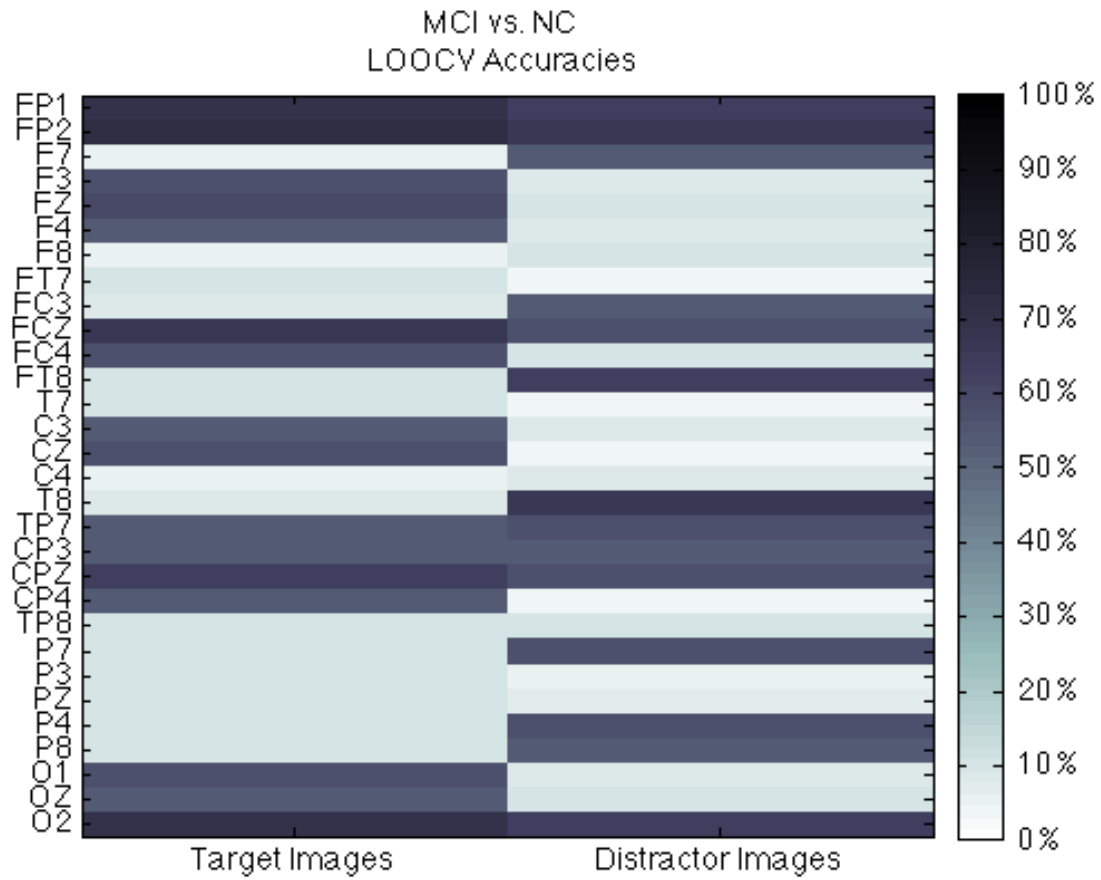
Fig. 3.4. MCI vs. NC LOOCV Accuracies for Working Memory MSE Ratios. As can be seen in the figure, for target images, the majority of differences are observed in channels of the occipital, frontal, and central regions. For distractor images, differences are concentrated in channels of the central and frontal regions.
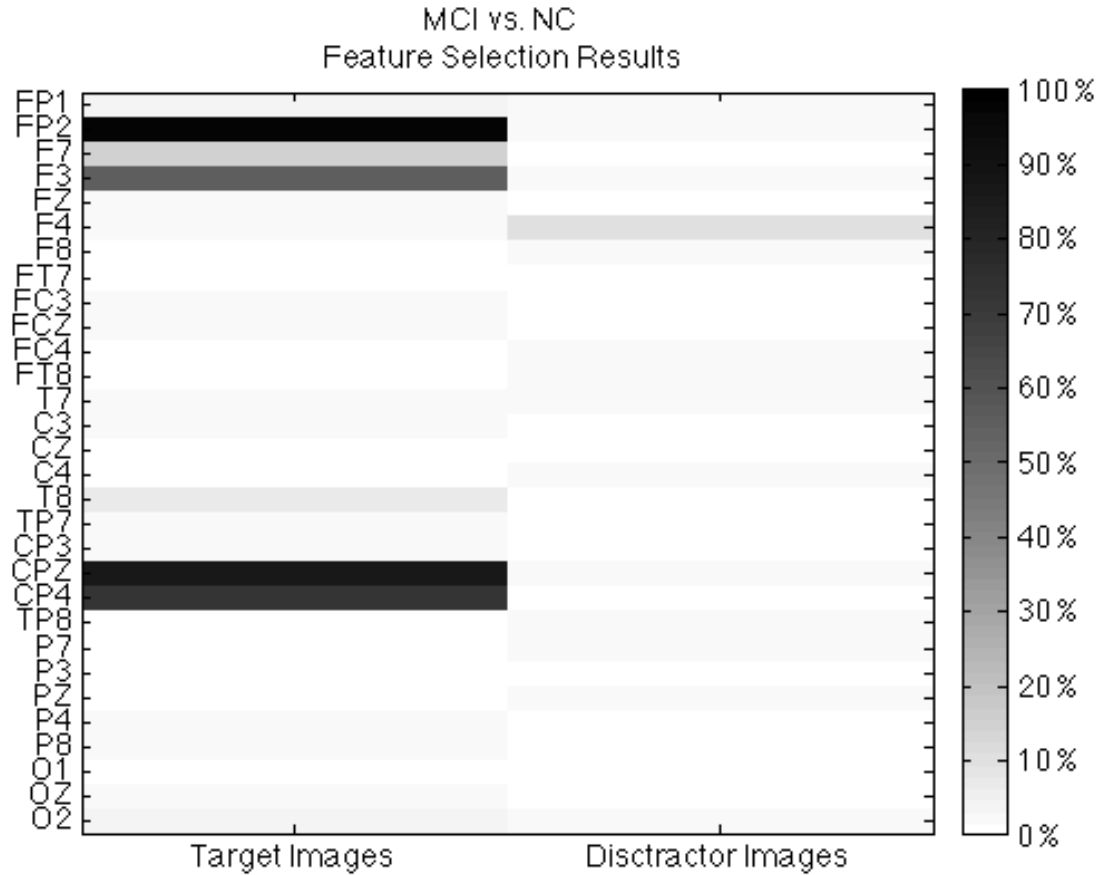
Fig. 3.5. Working Memory MSE Feature Selection Results for MCI vs. NC. Color scale indicates the inclusion of given features in the 200 best performing combinations for the given protocol condition. Note that target image ratios of channels in the frontal and anterior parietal regions appear to best discriminate MCI and NC participants.

Table 3.2. MCI vs. NC Discrimination Results Using Selected Working Memory MSE Ratios

# in combn.	Ratios	Acc. (Sens., Spec.)*	95% CI for p-value
1	$_{NC}^{MCI}R_{FP2}^{target}$	72.7% (68.8%, 76.5%)	(0.0245, 0.0300)
2	$_{NC}^{MCI}R_{FP2}^{target}$, $_{NC}^{MCI}R_{CPZ}^{target}$	78.8% (87.5%, 70.6%)	(0.0020, 0.0031)
3	$_{NC}^{MCI}R_{FP2}^{target}$, $_{NC}^{MCI}R_{CPZ}^{target}$, $_{NC}^{MCI}R_{CP4}^{target}$	81.8% (93.8%, 70.6%)	<7.980E-4
4	$_{NC}^{MCI}R_{FP2}^{target}$, $_{NC}^{MCI}R_{CPZ}^{target}$, $_{NC}^{MCI}R_{CP4}^{target}$, $_{NC}^{MCI}R_{F3}^{target}$	87.9% (93.8%, 82.4%)	<1.322E-4
5	$_{NC}^{MCI}R_{FP2}^{target}$, $_{NC}^{MCI}R_{CPZ}^{target}$, $_{NC}^{MCI}R_{CP4}^{target}$, $_{NC}^{MCI}R_{F3}^{target}$, $_{NC}^{MCI}R_{F7}^{target}$	84.9% (93.8%, 76.5%)	<3.176E-4

*acc. = overall LOOCV accuracy; sens. = sensitivity or accuracy in MCI group; spec. = specificity or accuracy in NC group
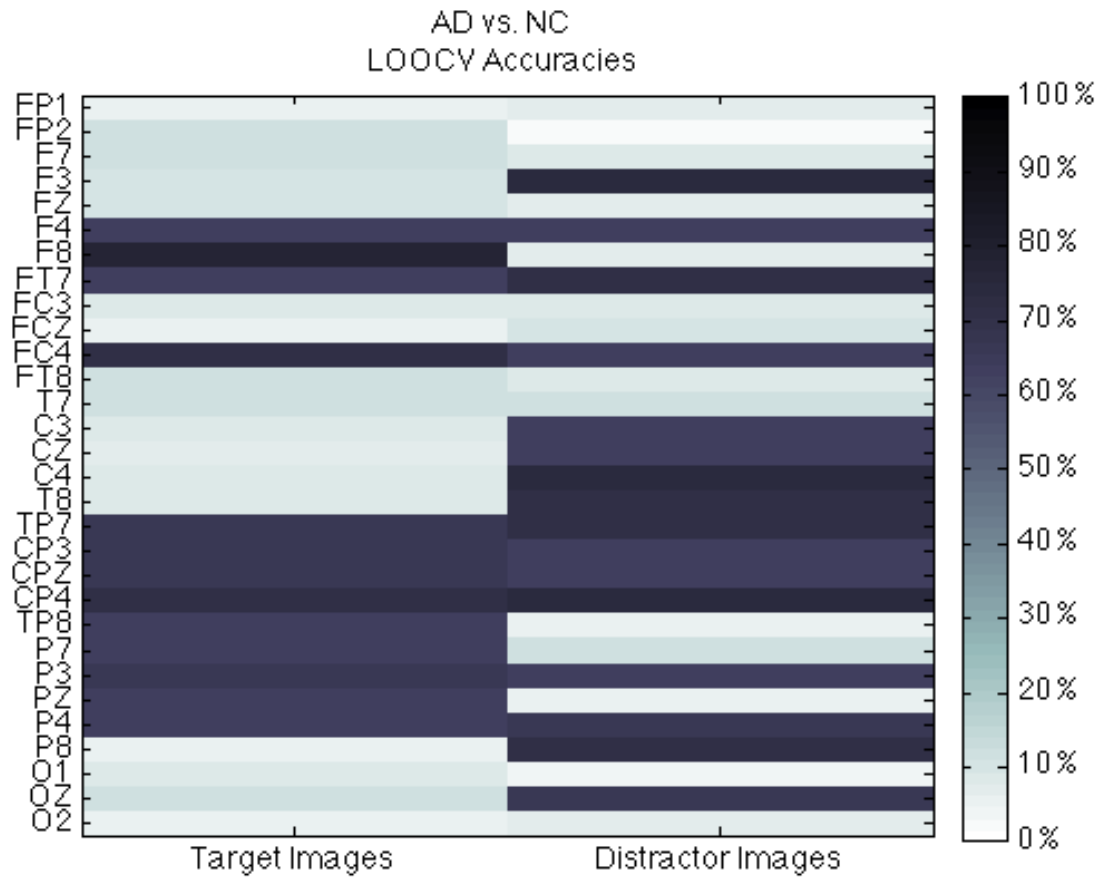
Fig. 3.6. AD vs. NC LOOCV Accuracies for Working Memory MSE Ratios. As can be seen in the figure, for target images, the majority of differences are observed in channels of the frontal and parietal regions. For distractor images, differences are concentrated in channels of the central, parietal, and frontal regions.

Fig. 3.7. Working Memory MSE Feature Selection Results for AD vs. NC. Color scale indicates the inclusion of given features in the 200 best performing combinations for the given protocol condition. Results from feature selection are poor, with only two to three ratios suggested. Ratios were selected based on individual performance instead.

Table 3.3. AD vs. NC Discrimination Results Using Selected Working Memory MSE Ratios

# in combn.	Ratios	Acc. (Sens., Spec.)*	95% CI for p-value
1	${}_{NC}^{AD}R_{F8}^{target}$	77.8% (80.0%, 76.5%)	(0.0056, 0.0101)
2	${}_{NC}^{AD}R_{F8}^{target}$, ${}_{NC}^{AD}R_{F3}^{distract}$	88.9% (90.0%, 88.2%)	<2.886E-5
3	${}_{NC}^{AD}R_{F8}^{target}$, ${}_{NC}^{AD}R_{F3}^{distract}$, ${}_{NC}^{AD}R_{C4}^{distract}$	88.9% (90.0%, 88.2%)	<3.732E-5
4	${}_{NC}^{AD}R_{F8}^{target}$, ${}_{NC}^{AD}R_{F3}^{distract}$, ${}_{NC}^{AD}R_{C4}^{distract}$, ${}_{NC}^{AD}R_{CP4}^{distract}$	77.8% (80.0%, 76.5%)	(0.0026, 0.0052)
5	${}_{NC}^{AD}R_{F8}^{target}$, ${}_{NC}^{AD}R_{F3}^{distract}$, ${}_{NC}^{AD}R_{C4}^{distract}$, ${}_{NC}^{AD}R_{CP4}^{distract}$, ${}_{NC}^{AD}R_{FC4}^{target}$	74.1% (70.0%, 76.5%)	(0.0273, 0.0131)

*acc. = overall leave-one-out cross-validation accuracy; sens. = sensitivity or accuracy in AD group; spec. = specificity or accuracy in NC group

**Fig. 3.8.** AD vs. MCI LOOCV Accuracies for Working Memory MSE Ratios. As can be seen in the figure, high accuracies are achieved using ratio from various regions of the scalp for both target and distractor images.
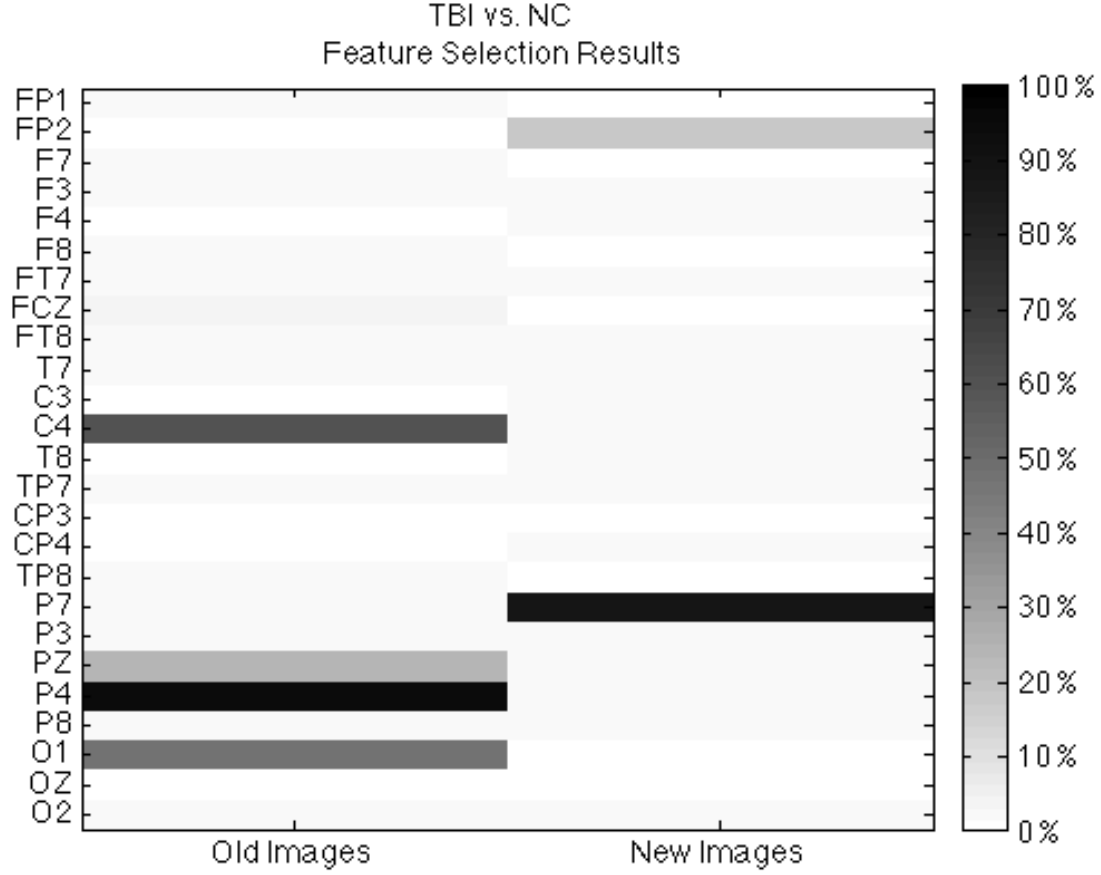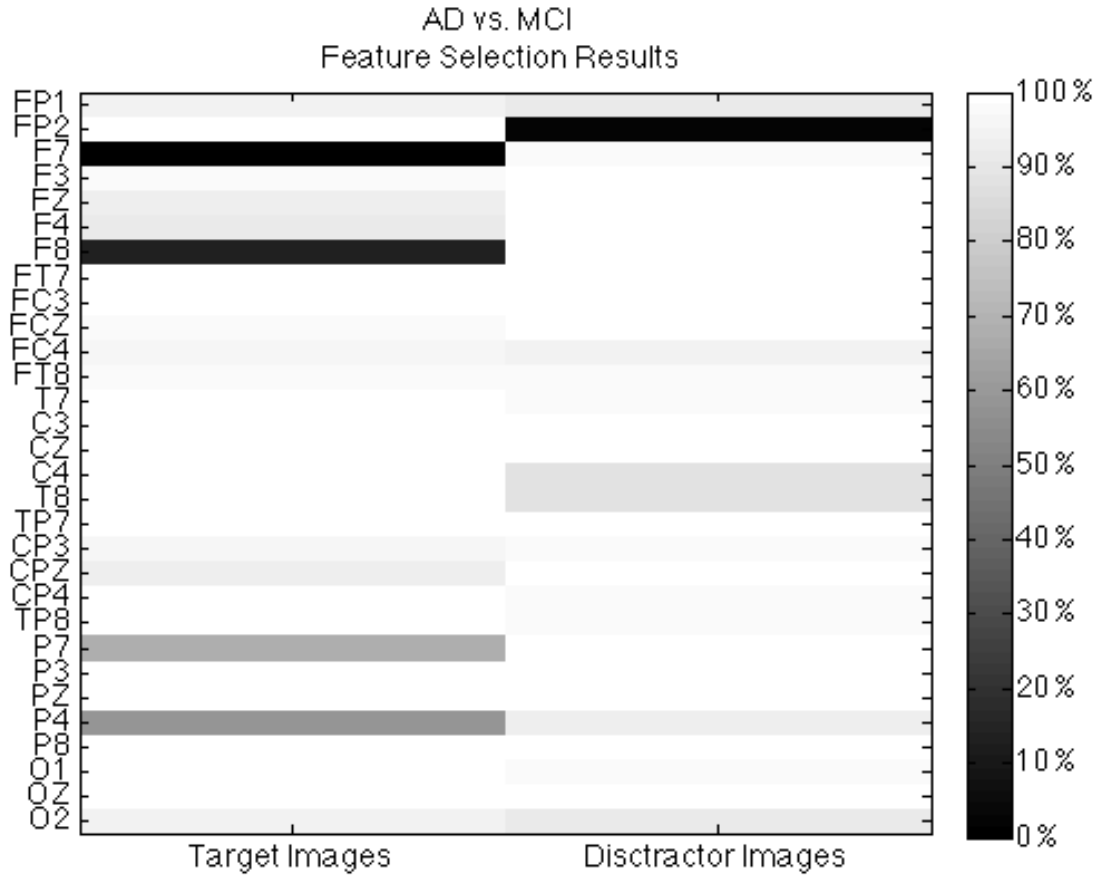
Fig. 3.9. Working Memory MSE Feature Selection Results for AD vs. MCI. Color scale indicates the inclusion of given features in the 200 best performing combinations for the given protocol condition. Note that target image ratios of channels in the frontal and anterior parietal regions appear to best discriminate MCI and NC participants.

Table 3.4. AD vs. MCI Discrimination Results Using Selected Working Memory MSE Ratios

# in combn.	Ratios	Acc. (Sens., Spec.)*	95% CI for p-value
1	$_{MCI}^{AD}R_{F7}^{target}$	80.8% (81.3%, 80.0%)	(0.0024, 0.0029)
2	$_{MCI}^{AD}R_{F7}^{target}$, $_{MCI}^{AD}R_{FP2}^{distract}$	84.6% (87.5%, 80.0%)	<8.016E-4
3	$_{MCI}^{AD}R_{F7}^{target}$, $_{MCI}^{AD}R_{FP2}^{distract}$, $_{MCI}^{AD}R_{F8}^{target}$	88.5% (93.8%, 80.0%)	<3.732E-5
4	$_{MCI}^{AD}R_{F7}^{target}$, $_{MCI}^{AD}R_{FP2}^{distract}$, $_{MCI}^{AD}R_{F8}^{target}$, $_{MCI}^{AD}R_{P4}^{target}$	92.3% (100%, 80.0%)	<4.910E-6
5	$_{MCI}^{AD}R_{F7}^{target}$, $_{MCI}^{AD}R_{FP2}^{distract}$, $_{MCI}^{AD}R_{F8}^{target}$, $_{MCI}^{AD}R_{P4}^{target}$, $_{MCI}^{AD}R_{P7}^{target}$	80.8% (93.8%, 60.0%)	(0.0099, 0.0273)

*acc. = overall LOOCV accuracy; sens. = sensitivity or accuracy in MCI group; spec. = specificity or accuracy in AD group

MCI and AD Non-event-related Results

MCI vs. NC

  MCI vs. NC NER leave-one-out cross-validation discrimination accuracies for individual ratios are presented in a graphical format in Fig. 3.10. Accuracies of up to 75% are possible using only the individual ratios. For the REO condition, differences are greatest for the occipital, frontotemporal, central, and parietal regions. Differences are widespread and more varied during the counting task. During the REC condition, differences are again seen the occipital, frontotemporal, and parietal regions.

  Feature selection results are presented in Fig. 3.11, where a color scale is used to indicate the inclusion of given features in the 200 best-performing feature combinations. Three ratios are clearly highlighted (black bars) in Fig. 3.10; however, 10-12 are ratios also have relatively high inclusivity (gray bars). Note that most of the highly inclusive ratios (ratios that perform best in combination) belong to the REO protocol condition. Ultimately, the five ratios with the highest inclusivity are selected and tested in combination using a quadratic SVM model. Specifically, these ratios are, in descending rank of performance, $^{MCI}_{NC}R^{REO}_{CZ}$, $^{MCI}_{NC}R^{REO}_{FCZ}$, $^{MCI}_{NC}R^{counting}_{FC3}$, $^{MCI}_{NC}R^{REO}_{CP3}$, and $^{MCI}_{NC}R^{REO}_{PZ}$. The results are summarized in Table 3.5. An accuracy of 80.7% (p-value <0.0028) is achieved using the first three selected ratios. Confidence intervals for p-values are estimated using Monte Carlo permutation testing

AD vs. NC

  AD vs. NC NER leave-one-out cross-validation discrimination accuracies for individual ratios are presented in a graphical format in Fig. 3.12. Accuracies of 50-60% are achieved with only individual ratios. As can be seen in the figure, for the REO condition, high accuracies are achieved for ratios of channels in the frontotemporal, parietal, and occipital regions. Well-performing ratios for the counting task and REC condition are more varied.

The feature selection results are presented in Fig. 5.13. The color scale indicates the inclusion of given features in the 200 best-performing feature combinations. Five ratios are clearly highly inclusive in the best-performing combinations. Specifically, these ratios are, in descending rank of performance, $^{AD}_{NC}R^{counting}_{CP3}$, $^{AD}_{NC}R^{REO}_{F3}$, $^{AD}_{NC}R^{REC}_{F3}$, $^{AD}_{NC}R^{REO}_{FCZ}$, and $^{AD}_{NC}R^{counting}_{FP1}$. LOOCV discrimination results are summarized in Table 3.6. An accuracy of 87.5% (p-value <1.322E-4) is achieved using the first four selected ratios. Confidence intervals for p-values are estimated using Monte Carlo permutation testing.

AD vs. MCI

  Results for AD vs. MCI NER leave-one-out cross-validation discrimination of individual ratios are presented in a graphical format in Fig. 3.14. Individual ratios achieve accuracies of up to 65%. For the REO condition, high accuracies are achieved for ratios of channels in the frontotemporal and frontal regions. Well-performing ratios for the counting

task and REC condition are more varied but do include occipital channels, which the REO condition did not.

Figure 3.9 presents the feature selection results, where a color scale is used to indicate the inclusion of given features in the 200 best-performing feature combinations. Five ratios are clearly highlighted in Fig. 3.9 as being highly discriminatory (highly inclusive). The five highlighted ratios are selected and tested in combination using a quadratic SVM model. Specifically, these ratios are, in descending rank of performance, $_{MCI}^{AD}R_{T7}^{counting}$, $_{MCI}^{AD}R_{TP7}^{REO}$, $_{MCI}^{AD}R_{O1}^{REC}$, $_{MCI}^{AD}R_{FCZ}^{REO}$, and $_{MCI}^{AD}R_{FP1}^{counting}$. The results are summarized in Table 3.7. An accuracy of 90.9% (p-value <2.788E-5) is achieved using the first four selected ratios. Confidence intervals for p-values are estimated using Monte Carlo permutation testing.
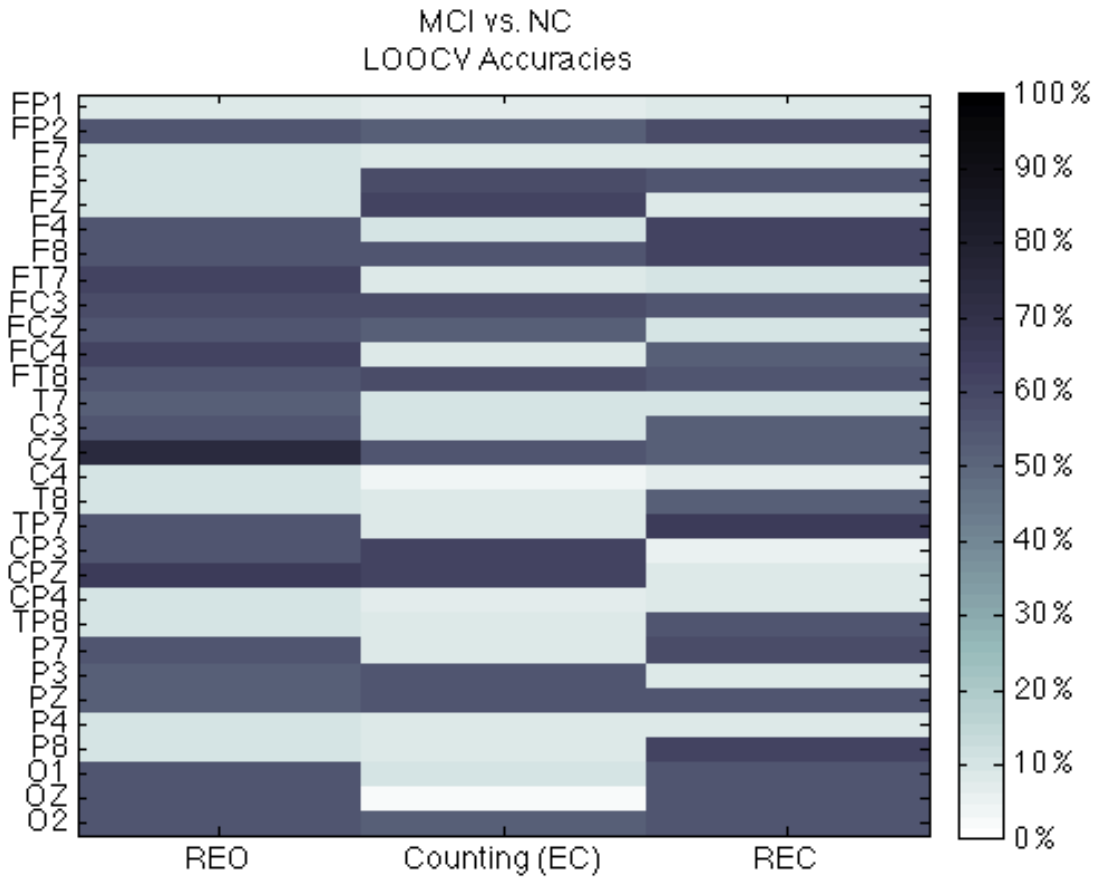
Fig. 3.10. MCI vs. NC LOOCV Accuracies for NER MSE Ratios. REO = resting, eyes open protocol; REC = resting, eyes closed protocol; EC = eyes closed. As can be seen in the figure, for the REO protocol, differences were greatest for the occipital, frontotemporal, central, and parietal regions. Differences were widespread and more varied during the counting task. During the REC protocol, differences were again seen the occipital, frontotemporal, and parietal regions.

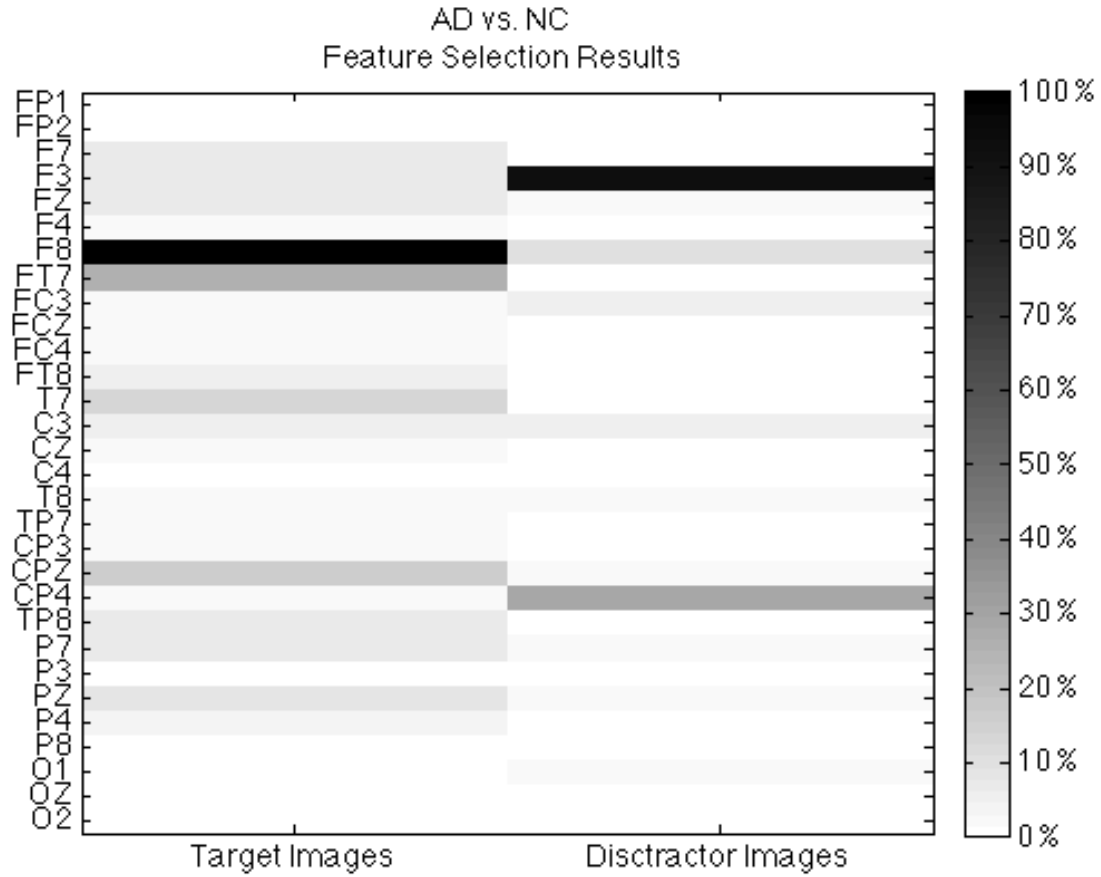56
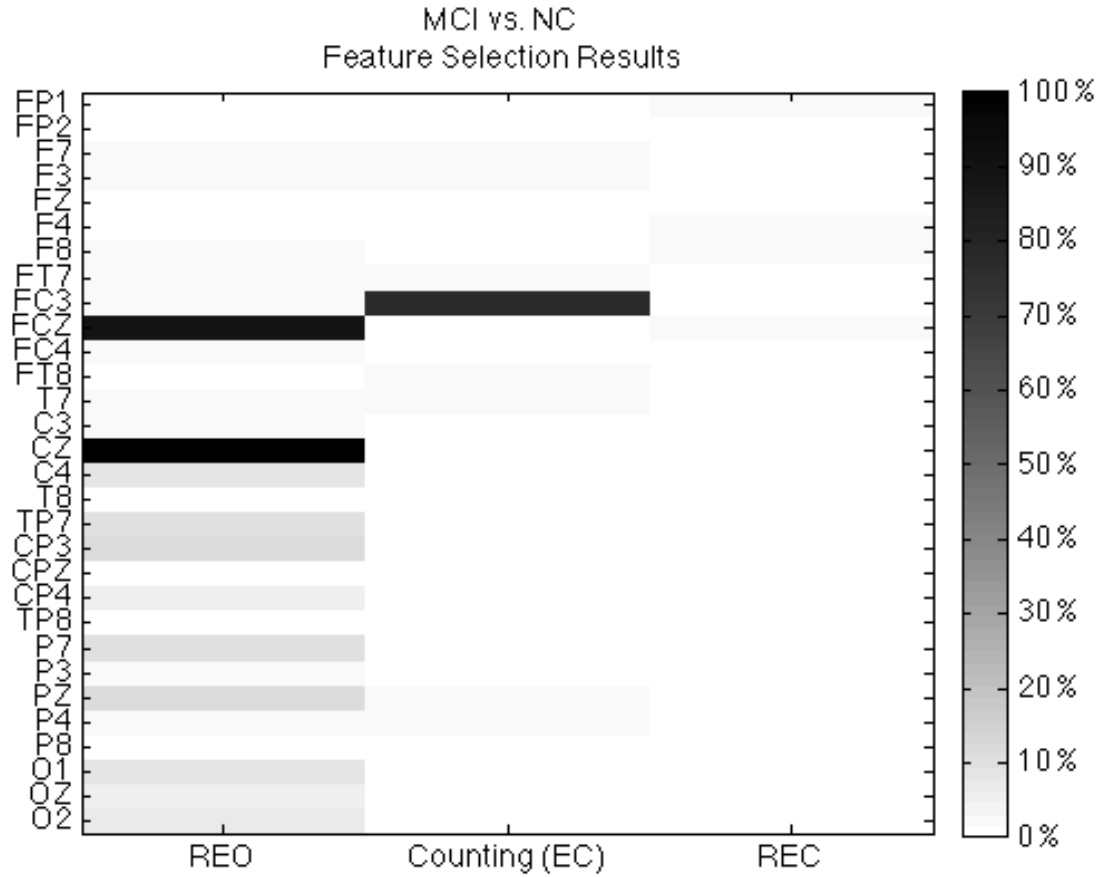
Fig. 3.11. NER MSE Feature Selection Results for MCI vs. NC. Color scale indicates the inclusion of given features in the 200 best performing combinations for the given protocol condition. REO = resting, eyes open protocol; REC = resting, eyes closed protocol; EC = eyes closed. Note that ratios for the REO protocol appear to best discriminate MCI and NC participants.

Table 3.5. MCI vs. NC Discrimination Results Using Selected NER MSE Ratios

# in combn.	Ratios	Acc. (Sens., Spec.)*	95% CI for p-value
1	$_{NC}^{MCI}R_{CZ}^{REO}$	74.2% (81.3%, 66.7%)	(0.0272, 0.0359)
2	$_{NC}^{MCI}R_{CZ}^{REO}$, $_{NC}^{MCI}R_{FCZ}^{REO}$	71.0% (87.5%, 53.3%)	(0.0591,0.0647)
3	$_{NC}^{MCI}R_{CZ}^{REO}$, $_{NC}^{MCI}R_{FCZ}^{REO}$, $_{NC}^{MCI}R_{FC3}^{counting}$	80.7% (87.5%, 73.3%)	(0.0018,0.0028)
4	$_{NC}^{MCI}R_{CZ}^{REO}$, $_{NC}^{MCI}R_{FCZ}^{REO}$, $_{NC}^{MCI}R_{FC3}^{counting}$, $_{NC}^{MCI}R_{CP3}^{REO}$	80.7% (87.5%, 73.3%)	(0.0010,0.0018)
5	$_{NC}^{MCI}R_{CZ}^{REO}$, $_{NC}^{MCI}R_{FCZ}^{REO}$, $_{NC}^{MCI}R_{FC3}^{counting}$, $_{NC}^{MCI}R_{CP3}^{REO}$, $_{NC}^{MCI}R_{PZ}^{REO}$	80.7% (87.5%, 73.3%)	(0.0002,0.0015)

*acc. = overall LOOCV accuracy; sens. = sensitivity or accuracy in MCI group; spec. = specificity or accuracy in NC group
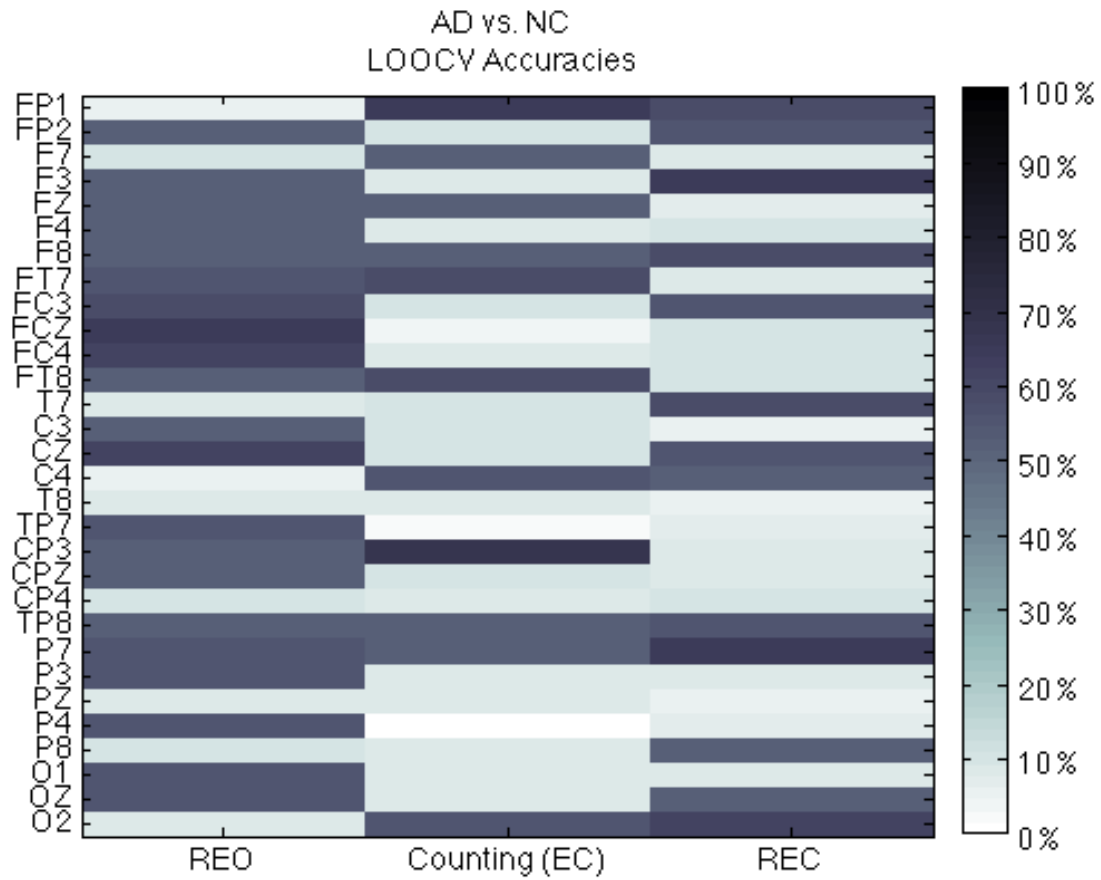
Fig. 3.12. AD vs. NC LOOCV Accuracies for NER MSE Ratios. REO = resting, eyes open protocol; REC = resting, eyes closed protocol; EC = eyes closed. As can be seen in the figure, for the REO protocol, high accuracies are achieved for ratios of channels in the frontotemporal, parietal, and occipital regions. Well-performing ratios for the counting task and REC protocol are more varied.
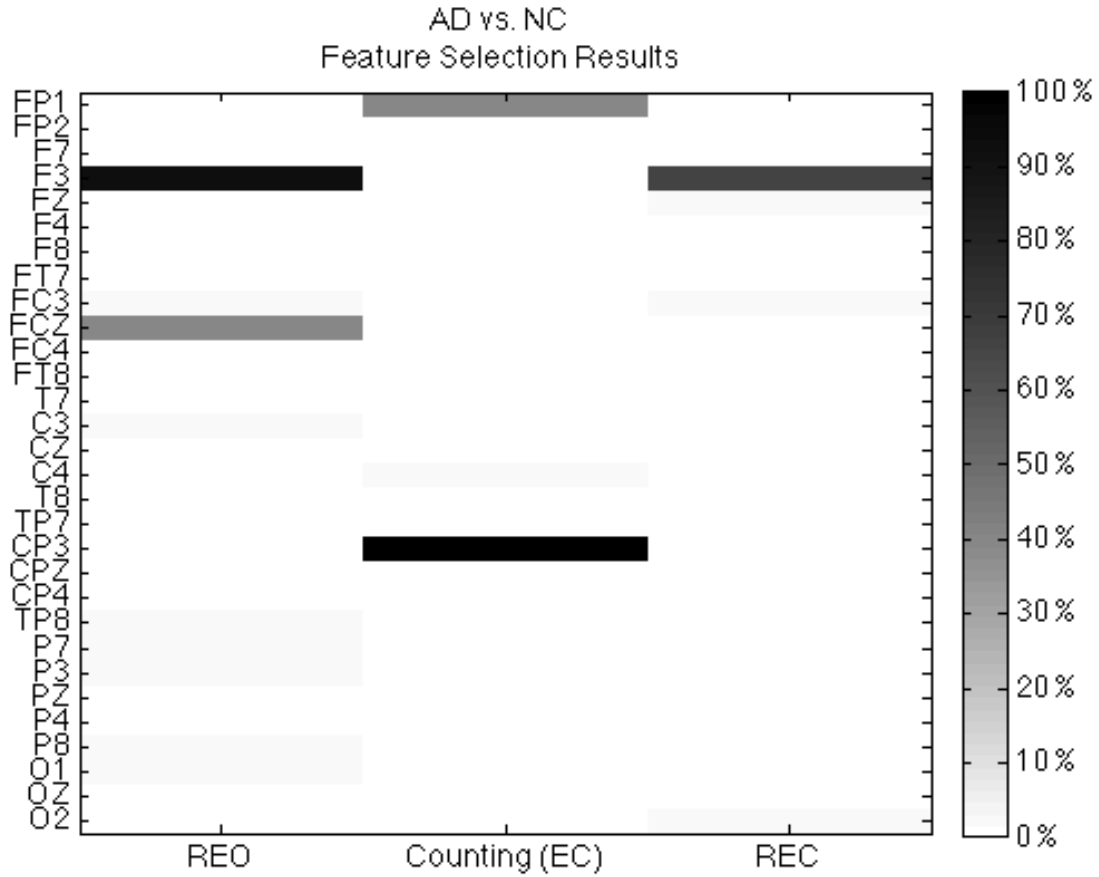
Fig. 3.13. NER MSE Feature Selection Results for AD vs. NC. Color scale indicates the inclusion of given features in the 200 best performing combinations for the given protocol condition. REO = resting, eyes open protocol; REC = resting, eyes closed protocol; EC = eyes closed.

Table 3.6. AD vs. NC Discrimination Results Using Selected NER MSE Ratios

# in combn.	Ratios	Acc. (Sens., Spec.)*	95% CI for p-value
1	$_{NC}^{AD}R_{CP3}^{counting}$	68.8% (47.1%, 93.3%)	(0.0319 0.0755)
2	$_{NC}^{AD}R_{CP3}^{counting}$, $_{NC}^{AD}R_{F3}^{REO}$	75.0% (58.8%, 93.3%)	(0.0091,0.0099)
3	$_{NC}^{AD}R_{CP3}^{counting}$, $_{NC}^{AD}R_{F3}^{REO}$, $_{NC}^{AD}R_{F3}^{REC}$	84.4% (76.5%, 93.3%)	<7.980E-4
4	$_{NC}^{AD}R_{CP3}^{counting}$, $_{NC}^{AD}R_{F3}^{REO}$, $_{NC}^{AD}R_{F3}^{REC}$, $_{NC}^{AD}R_{FCZ}^{REO}$	87.5% (82.4%, 93.3%)	<1.322E-4
5	$_{NC}^{AD}R_{CP3}^{counting}$, $_{NC}^{AD}R_{F3}^{REO}$, $_{NC}^{AD}R_{F3}^{REC}$, $_{NC}^{AD}R_{FCZ}^{REO}$, $_{NC}^{AD}R_{FP1}^{counting}$	75.0% (64.7%, 86.7%)	(0.0073,0.0087)

*acc. = overall LOOCV accuracy; sens. = sensitivity or accuracy in AD group; spec. = specificity or accuracy in NC group
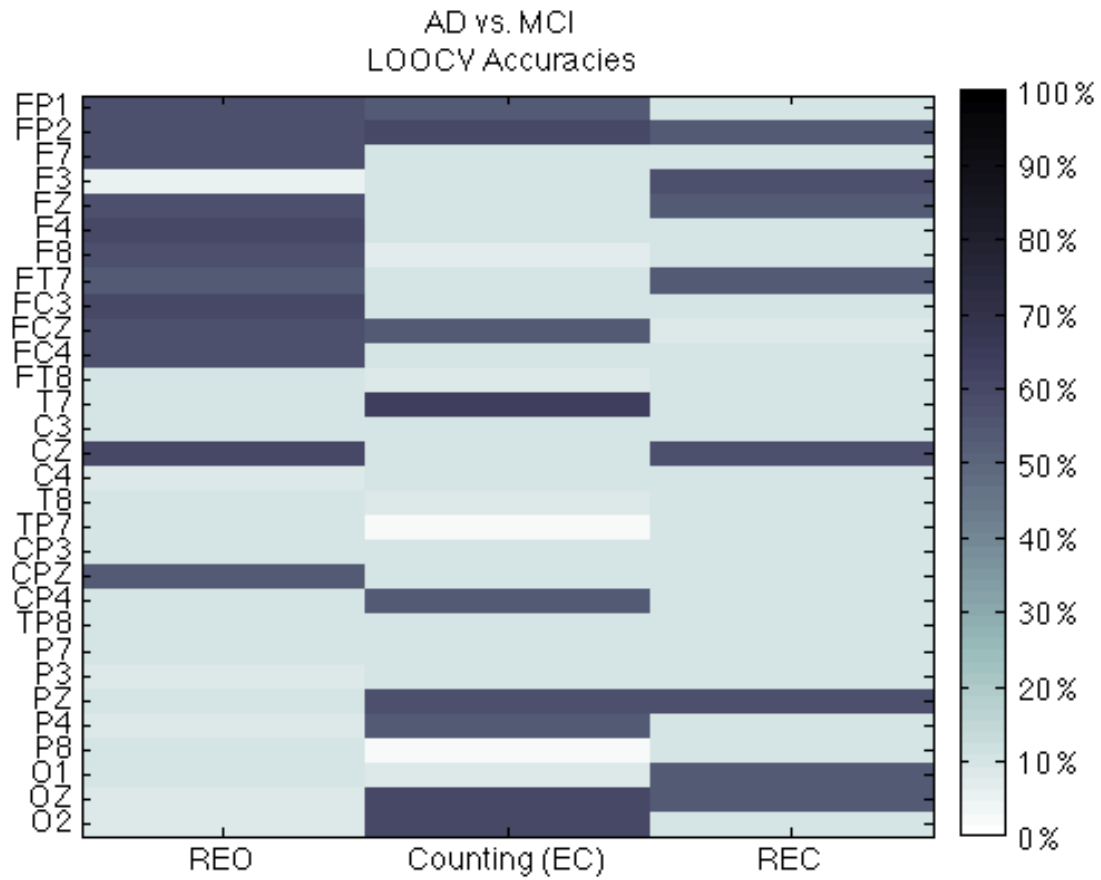
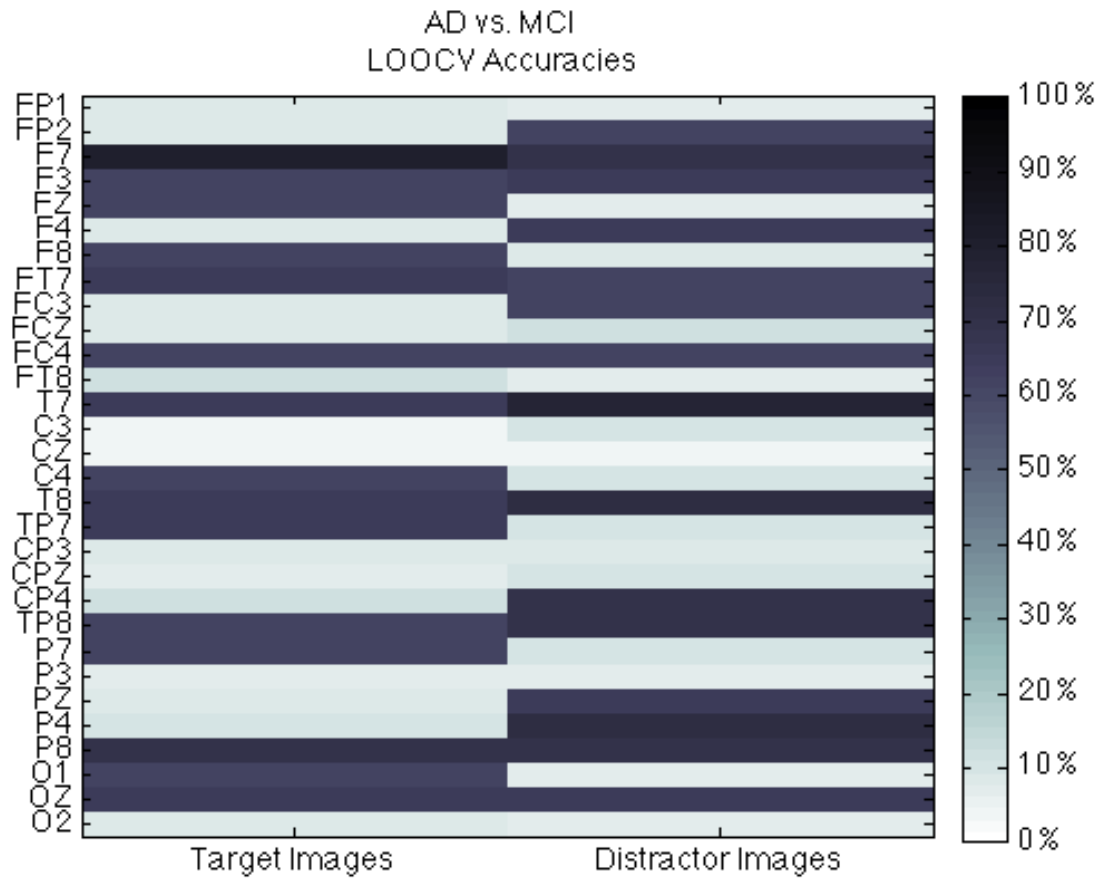**Fig. 3.14.** AD vs. MCI LOOCV Accuracies for NER MSE Ratios. REO = resting, eyes open protocol; REC = resting, eyes closed protocol; EC = eyes closed. As can be seen in the figure, for the REO protocol, high accuracies are achieved for ratios of channels in the frontotemporal and frontal regions. Well-performing ratios for the counting task and REC protocol are more varied but do include occipital channels, which the REO protocol did not.
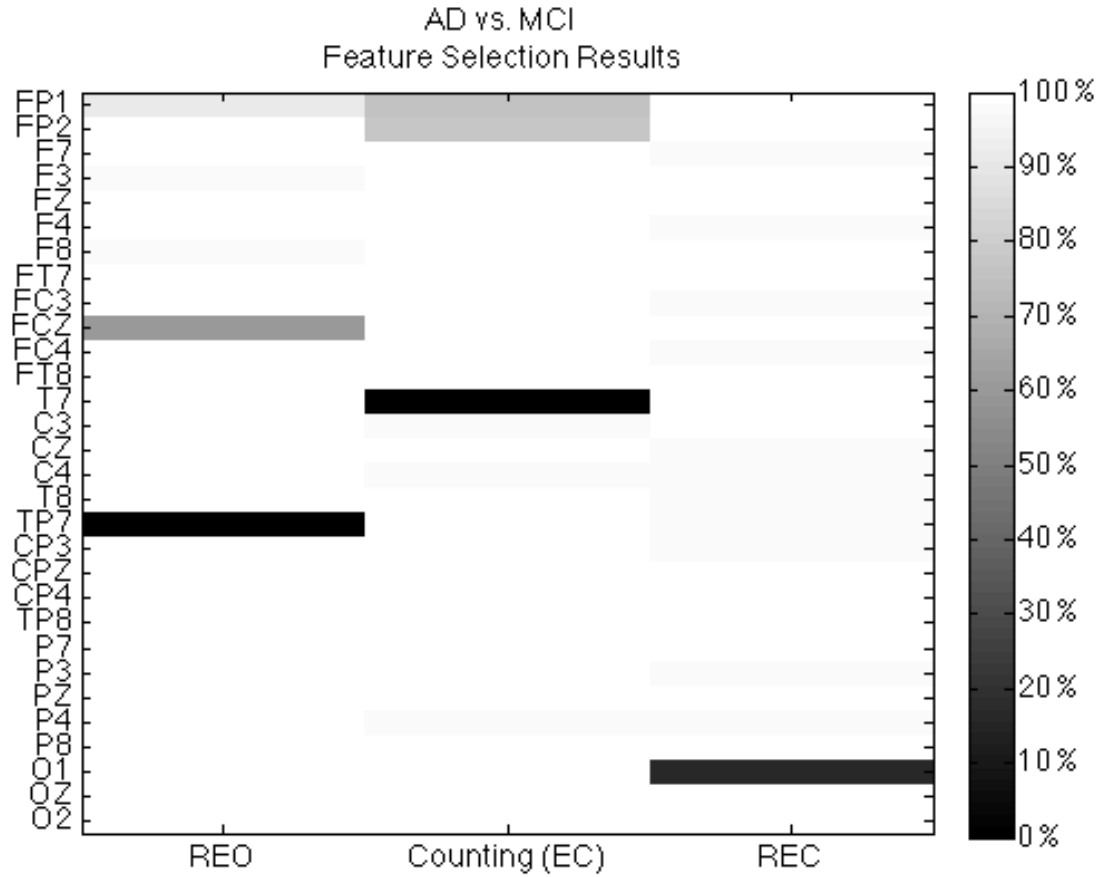
Fig. 3.15. NER MSE Feature Selection Results for AD vs. MCI. Color scale indicates the inclusion of given features in the 200 best performing combinations for the given protocol condition. REO = resting, eyes open protocol; REC = resting, eyes closed protocol; EC = eyes closed.

Table 3.7. AD vs. MCI Discrimination Results Using Selected NER MSE Ratios

# in combn.	Ratios	Acc. (Sens., Spec.)*	95% CI for p-value
1	$_{MCI}^{AD}R_{T7}^{counting}$	63.6% (81.3%, 47.1%)	(0.2153, 0.2990)
2	$_{MCI}^{AD}R_{T7}^{counting}$, $_{MCI}^{AD}R_{TP7}^{REO}$	81.8% (81.3%, 82.4%)	<8.016E-4
3	$_{MCI}^{AD}R_{T7}^{counting}$, $_{MCI}^{AD}R_{TP7}^{REO}$, $_{MCI}^{AD}R_{O1}^{REC}$	87.9% (87.5%, 88.2%)	<1.883E-4
4	$_{MCI}^{AD}R_{T7}^{counting}$, $_{MCI}^{AD}R_{TP7}^{REO}$, $_{MCI}^{AD}R_{O1}^{REC}$, $_{MCI}^{AD}R_{FCZ}^{REO}$	90.9% (87.5%, 94.1%)	<2.788E-5
5	$_{MCI}^{AD}R_{T7}^{counting}$, $_{MCI}^{AD}R_{TP7}^{REO}$, $_{MCI}^{AD}R_{O1}^{REC}$, $_{MCI}^{AD}R_{FCZ}^{REO}$, $_{MCI}^{AD}R_{FP1}^{counting}$	84.9% (87.5%, 82.4%)	<6.603E-4

*acc. = overall LOOCV accuracy; sens. = sensitivity or accuracy in MCI group; spec. = specificity or accuracy in AD group

Discussion and Conclusions

Observations for TBI

Previous research has shown the capability of ERPs recorded during cognitive tasks to reveal cognitive deficits in both the acute and long-term recovery process of TBI. ERP analysis, however, generally requires redundant protocols and multiple trials, making ERP studies inconvenient. In contrast, the MSE method presented here allows for meaningful data to be extracted from a single trial.

As discussed in Chapter 2, previous work by Sneddon *et al.* has demonstrated that event-related entropy measures of EEG can be used to discriminate MCI from normal controls with accuracy comparable of PET scans, and that the accuracy is dependent on the cognitive task employed [126]. The use of ratios of the distances from group average MSE curves presented here is capable of achieving high levels of accuracy (93.3%), comparable to the accuracy reported by Sneddon *et al.* Interestingly, the selected ratios selected via feature selection are from channels located in the frontal and posterior parietal regions of the scalp. In their work, Sneddon *et al.* investigated the ratio of frontal to parietal event-related Tsallis entropy, noting that EEG from those two regions appeared to contain more diagnostically relevant entropy changes in response to visual stimuli [126].

The accuracy in discriminating TBI vs. NC EEG records achieved likely reflects underlying differences resulting from altered neural mechanisms in TBI brains during short-term memory recognition tasks. The ventral stream of the autonomic pathway of visual information processing in the brain is known to involve the occipital, central, parietal, right temporal, and ultimately frontal lobes [121]. The parietal lobe is a hub of neural connections in the brain. Information from visual stimuli passes from the eyes, to the occipital lobe, and then to the parietal lobe before branching out into the sensory-motor cortex, temporal lobes, and frontal lobe [121]. Any observable differences in the parietal lobe may indicative of differences in brain functional organization. Furthermore, the frontal lobe is involved in the contextualizing and analysis of visual information and the temporal lobes are involved in emotion and memory. Keeping these facts in mind, it is interesting to observe that ratios of channels in the frontotemporal and parietal regions of the scalp achieved high LOOCV accuracies for old (studied) images.

The results in this work demonstrate a strong relationship between event-related MSE measures and the presence of moderate to severe TBI. Results suggest that a simple model based on SVM with a quadratic kernel function and the MSE measures presented here may be a viable method for the development of a diagnostic screening tool for evaluation of TBI during the recovery process.

The reported injuries in the TBI participants were widespread across the brain. One limitation of this study is the lack of access to data to allow evaluation of the correlation between the areas of brain injury with MSE results. A future study examining participants

with acute damage in a known area of the brain may be able to provide further insights into area-specific TBI.

Comparison of Event-related and NER Results for MCI and AD

MCI vs. NC

For both the working memory protocol and the NER data, individual ratios are capable of achieving LOOCV accuracies in the 60-75% range for MCI vs. NC discrimination. For the working memory task, ratios corresponding to channels in the occipital, frontal, and central regions (target images) perform the best. Ratios of channels in the frontotemporal and parietal regions also perform well during both of the resting protocols. An accuracy of 87.9% (p-value <1.322E-4) is achieved for the working memory task, while an accuracy of only 80.7% (p-value <0.0028) is achieved for the NER protocols.

AD vs. NC

AD vs. NC LOOCV discrimination accuracies of individual ratios are very high for the working memory protocol (up to 80%) compared to those achieved for the NER protocols (up to 60%). The feature selection process performs poorly for the working memory data (likely due to the fact that so many ratios perform well individually). Ultimately, the five ratios with the highest individual performance are selected. Well-performing ratios in the working memory task corresponded to channels in the frontal and central regions for both image types. For the REO condition, the best performing ratios corresponded to the frontotemporal, parietal, and occipital regions. For the eyes closed protocols, regions do not cluster well-performing ratios. An accuracy of 88.9% (p-value <2.886E-5) is achieved for the working memory task using the first two selected ratios. A comparable accuracy of 87.5% (p-value <1.322E-4) is achieved for the NER data using the first four selected ratios.

AD vs. MCI

Working memory ratios perform better individually for AD vs. MCI discrimination than those derived from NER data. Working memory ratios are capable of achieving LOOCV accuracies in the 70-80% range vs. the 50-65% range achieved by NER ratios. The best-performing working memory ratios correspond to channels in various regions across the scalp. For the REO condition, the well-performing ratios correspond to channels in the frontotemporal and frontal regions. During the eyes closed protocols, the corresponding channels are again in various regions. An accuracy of 92.3% (p-values <4.910E-6) is achieved using the first four selected working memory ratios. A comparable accuracy of 90.9% (p-value <2.788E-5) is achieved using the first four selected NER ratios. While the NER ratios perform more poorly on an individual basis, the accuracy improves dramatically with combinations of only two are considered.

The high accuracy achieved here in discriminating between MCI and NC is encouraging as there is great interest in being able to detect cognitive decline that may be associated with AD at the earliest stages. The results of this work suggest the potential for the use of MSE complexity features representing scalp electrical activity as a means for objectively discriminating between normal, MCI, and AD participants. The current method cannot be readily applied to the clinical setting since it requires 25-30 EEG channels and

takes about 30 minutes to collect the data (including setup time) for the working-memory (event-related) approach. While the validity of the approach has been demonstrated for MCI and AD using a shorter protocol and NER EEG, the same was not performed for TBI. In addition, fewer electrodes would be ideal for more convenient application. Another shortcoming of the current studies is the need for a larger sample size. Furthermore, new test samples would also be needed to further validate the approach before it could be applied in a private practice setting. The methodology presented may be used in future investigations to develop simple and effective means for evaluating the recovery of TBI and the detection of MCI and early-stage AD in the primary care setting.

CHAPTER 4
NER DISCRIMINATION OF MCI AND AD
USING TRANSFER ENTROPY

In this Chapter, a method for quantifying the inter-channel, causal transfer of information in EEG for discrimination of MCI and AD is presented. The EEG records used in this study were recorded during resting states and a simple cognitive task (NER Dataset); see Chapter 1 for more details regarding data collection procedures. This Chapter begins with an introduction to the mathematical theory transfer entropy. Next, the methodology for developing intra- and inter-regional transfer entropy measures capable of characterizing differences in MCI and AD are described. Finally, results obtained for discrimination of MCI and AD EEG records are presented and discussed.

Mathematical Theory of Transfer Entropy

Mutual Information

Recall from Chapter 2 that information can be defined mathematically as that which decreases uncertainty [125]. Entropy, being a measure of the uncertainty in a system, can therefore be used to mathematically quantify the basic amount of information in a time series [125]. For example, the average number of bits required to optimally encode independent samples of a discrete variable x, which follows a probability distribution function p_x, is given by the classical definition for Shannon entropy, as presented in Equation (2.1) and modified for the specific random variable x in Equation (4.1):

$$S = -\sum_{i=1}^{N} p_x(x_i) \log_2[p_x(x_i)], \quad (4.1)$$

where the sum extends over all possible states x_i $(i = 1, \dots, N)$ the random variable x can assume. The base of the logarithm depends only on the units used for measuring information; thus, it will be dropped in further equations. If a different distribution is used, there will be an excess number of bits and the information will not be optimally encoded [118]. The excess number of bits that will be encoded if a different distribution function q is used is given by the Kullback entropy K as presented in Equation (4.2) [79]:

$$K = \sum_{i=1}^{N} p_x(x_i) \log\left[\frac{p_x(x_i)}{q(x_i)}\right] \quad (4.2)$$

The mutual information of two random variables x and y with joint probability distribution function $p_{x,y}$ can be viewed as the excess amount of code produced when the

two variables are assumed to be independent. That is, assuming $p_{x,y}(x_i, y_j) = p_x(x_i)p_y(y_j)$. Mutual information M_{xy} between the variables x and y is thus the Kullback entropy given the assumption of independence between the two variables, as presented in Equation (4.3):

$$M_{xy} = \sum_{i=1}^{N}\sum_{j=1}^{M} p_{x|y}(x_i, y_j) \log\left[\frac{p_{x,y}(x_i, y_j)}{p_x(x_i)p_y(y_j)}\right] \quad (4.3)$$

where the random variable y can assume states y_j ($j = 1, \ldots, M$). Mutual information thus provides an intuitive means for quantifying the deviation from independence of two random variables. Note that mutual information M_{xy} is symmetric under the exchange of x and y and therefore does not contain any information regarding the directional transfer of information (causality).

Transfer Entropy

Suppose that the variables x and y are generated by two separate but coupled systems. An entropy rate S_1 can be defined as the amount of additional information required to represent the current value x_n of the random variable x given the value of both variables at an observation d steps in the past, as presented in Equation (4.4):

$$S_1 = -\sum_{x_n}\sum_{x_{n-d}}\sum_{y_{n-d}} p_{x_n, x_{n-d}, y_{n-d}}(x_n, x_{n-d}, y_{n-d}) \log[p_{x_n|x_{n-d}, y_{n-d}}(x_n|x_{n-d}, y_{n-d})], \quad (4.4)$$

where $p_{x_n, x_{n-d}, y_{n-d}}$ is the joint probability function for the observations x_n, x_{n-d}, and y_{n-d}, and $p_{x_n|x_{n-d}, y_{n-d}}$ is the conditional probability function for x_n given x_{n-d} and y_{n-d}. Further suppose that the value of the current observation x_n of the random variable x is independent of the value of the random variable y observed d steps in the past (y_{n-d}). The entropy rate in this case would then reduce to Equation (4.5):

$$S_2 = -\sum_{x_n}\sum_{x_{n-d}}\sum_{y_{n-d}} p_{x_n, x_{n-d}, y_{n-d}}(x_n, x_{n-d}, y_{n-d}) \log[p_{x_n|x_{n-d}}(x_n|x_{n-d})], \quad (4.5)$$

where $p_{x_n|x_{n-d}}$ is the conditional probability function for x_n given x_{n-d}. The incorrectness of this assumption can then be express as the difference $S_2 - S_1$ between the two entropy rates presented in Equation (4.4) and (4.5). This difference in entropy is then termed transfer entropy $T_{y \to x}^d$, and is presented in Equation (4.6) [118]:

$$T_{y \to x}^d = \sum_{x_n}\sum_{x_{n-d}}\sum_{y_{n-d}} p_{x_n, x_{n-d}, y_{n-d}}(x_n, x_{n-d}, y_{n-d}) \log\left[\frac{p_{x_n|x_{n-d}, y_{n-d}}(x_n|x_{n-d}, y_{n-d})}{p_{x_n|x_{n-d}}(x_n|x_{n-d})}\right] \quad (4.6)$$

Substituting the definitions for the conditional probabilities given in Equations (4.7)—(4.8), Equation (4.6) reduces to Equation (4.9):

$$p_{x_n|x_{n-d},y_{n-d}}(x_n|x_{n-d},y_{n-d}) = \frac{p_{x_n,x_{n-d},y_{n-d}}(x_n,x_{n-d},y_{n-d})}{p_{x_{n-d},y_{n-d}}(x_{n-d},y_{n-d})}, \quad (4.7)$$

$$p_{x_n|x_{n-d}}(x_n|x_{n-d}) = \frac{p_{x_n,x_{n-d}}(x_n,x_{n-d})}{p_x(x_n)}, \quad (4.8)$$

$$T_{y \to x}^d =$$

$$\sum_{x_n} \sum_{x_{n-d}} \sum_{y_{n-d}} p_{x_n,x_{n-d},y_{n-d}}(x_n,x_{n-d},y_{n-d}) \log \left[\frac{p_{x_n,x_{n-d},y_{n-d}}(x_n,x_{n-d},y_{n-d})p_x(x_n)}{p_{x_{n-d},y_{n-d}}(x_n,y_{n-d})p_{x_n,x_{n-d}}(x_n,x_{n-d})} \right], \quad (4.9)$$

where $p_{x_{n-d},y_{n-d}}$ is the joint probability of variables x_{n-d} given y_{n-d}, and $p_{x_n,x_{n-d}}$ is the joint probability of variables x_n and x_{n-d}. The transfer entropy $T_{y \to x}^d$ is explicitly not symmetric since it measures the degree of dependence of x on y and not vice versa. Thus, $T_{y \to x}^d \neq T_{x \to y}^d$.

Generally, transfer entropy is computed for binary sequences, where time series data x and y are converted to binary symbolic sequences r and s using a simple threshold method as discussed in detail in Chapter 5. The most usual means to do this is to convert each signal into a 1/0 symbolic sequence by comparing the signal to the median value of each signal; a signal is larger than its median value, one maps the signal to 1, otherwise, to 0. A code for computing transfer entropy is presented below:

```
% code for computing transfer entropy (y -> x)
x = N x 1 time series
y = N x 1 time series
d = delay % set delay

% convert times series x and y into binary sequences s and r,
% respectively
s = N x 1 zero vector;
indx = find(x>mean(x));
s(indx) = 1;
r = N x 1 zero vector;
indx = find(y>mean(y));
r(indx) = 1;

% compute Px (probX)
% 2 possibilities: 0,1
probX(1) = length(find(s(d+1:N)=0))/(N-d);
probX(2) = 1-probX(1);
```

```
% compute joint probability Px,x-d (probXX)
% 4 possibilities: 0-0, 0-1, 1-0, 1-1
probXX = 4 x 1 zero vector;
for i = 0,1 % x
    for j = 0,1 % x-d
        probXX(i*2+j+1) = length(find(s(d+1:N)=i && …
        s(1:N-d)=j))/(N-d);
    end
end

% compute joint probability Px-d,y-d (probXY)
% 4 possibilities: 0-0, 0-1, 1-0, 1-1
probXY = 4 x 1 zero vector;
for j = 0,1 % x-d
    for k = 0,1 % y-d
        probXY(j*2+k+1) = length(find(s(1:N-d)=j && …
        r(1:N-d)=k))/(N-d);
    end
end

% compute joint probability Px,x-d,y-d (probXXY)
% 6 possibilities: 0-0-0, 0-0-1, 0-1-0, 0-1-1, 1-0-0, 1-0-1,
% 1-1-0, 1-1-1
probXXY = 6 x 1 zero vector;
for i = 0,1 % x
    for j = 0,1 % x-d
        for k = 0,1 % y-d
            probXXY(i*4+j*2+k+1) = length(find(s(d+1:N)=I &&…
            s(1:N-d)=j &&  r(1:N-d)=k))/(N-d);
        end
    end
end

% compute transfer entropy (TE)
TE = 0;
for i = 0,1 % x
    for j = 0,1 % x-d
        for k = 0,1 % y-d
            % for appropriate indices
            TE=TE+probXXY*log2(probXXY*probX/(probXX*probXY))
            end
        end
    end
end
```

Methodology

Peak Inter-regional Transfer Entropy Delays (PITEDs)

Transfer entropies are computed for each directional, pairwise combination of 30 channels (2 ocular channels excluded) for each protocol condition. The first 2 min of data for each protocol condition is used. Entropies are computed for delays of 0.002 through 1 s in 0.002-s steps. The delay at which the transfer entropy is greatest in magnitude is noted as the peak delay.

The 30 channels are grouped into 14 scalp regions based their arrangement and location on the scalp. The regions include: (1) left frontal (LF); (2) right frontal (RF); (3) frontal (F = LF + RF + channel FZ); (4) left temporal (LT); (5) right temporal (RT); (6) left central (LC); (7) right central (RC); (8) central (C = LC + RC + channels FCZ and CZ); (9) left parietal (LP); (10) right parietal (RP); (11) parietal (P = LP + RP + channels CPZ and PZ); (12) left occipital (LO); (13) right occipital (RO); and (14) occipital (O = LO + RO + channel OZ). Note that left and right regions do not include central line channels; see Fig. 4.1 for regional boundaries.

The mean peak delays between regions are computed as follows. For each directional pairing of regions (for example, region X → region Y), the peak delay for each channel in the first region (region X) to those in the second region (region Y) are averaged; see Equation (4.10), where $d_{i \to j}^{peak}$ is the peak delay for channel i in region X to channel j in region Y, N_x is the number of channels in region X, and N_y is the number of channels in region Y. Regional pairings are not made between major regions (C, F, O, P, R) and their sub-regions. For example, the peak inter-regional delays for F→LF or LF→F are not computed. Thus, a total of 166 directional, mean peak inter-regional transfer entropy delays (PITEDs) are determined for each protocol condition.

$$PITED_{x \to y} = \frac{1}{N_x N_y} \sum_{i=1}^{N_x} \sum_{j=1}^{N_y} d_{i \to j}^{peak} \qquad (4.10)$$

Binary Discrimination

Feature Selection
Feature selection is performed for each of three binary discrimination problems (MCI vs. NC, AD vs. NC, and MCI vs. AD) for each protocol condition as follows. Combinations of up to five PITEDs are tested using SVM functions in MATLAB™ [88]. Quadratic kernel functions are used in all discriminations and the cost coefficient is held constant at unity. *Nested* LOOCV loops are used to avoid overfitting while suggesting and testing different combinations of PITEDs as features. The inner loop generated a list of suggested combinations via a forward, high-score, features selection method where combinations are scored using LOOCV accuracy of SVM model predictions from a smaller,
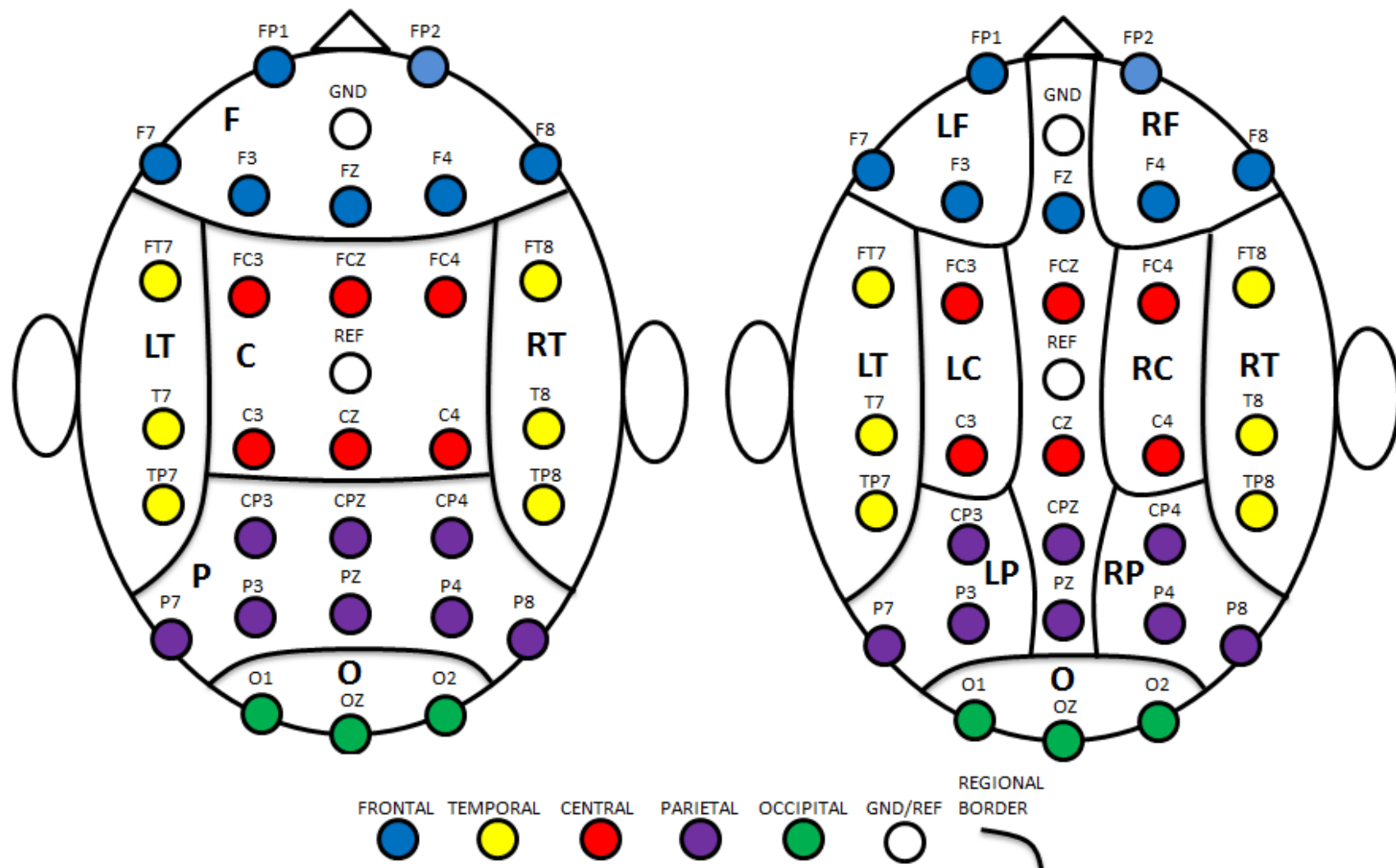
Fig. 4.1. Regional and Subregional Boundaries for Electrodes. Left: major regions; right: subregions. LF=left frontal; RF=right frontal; F=frontal; LT=left temporal; RT=right temporal; LC=left central; RC=right central; C=central; LP=left parietal; RP=right parietal; P=parietal; O=occipital. Note that central line channels (those with Z in the designation) are excluded from L/R subregions.

randomized, subset of records [143]. The outer loop determined the LOOCV accuracy of combinations suggested by the inner loop for *all* available records.

The discriminatory power of individual PITEDs is then assessed based on how often they appeared in the 200 best performing combinations tested in the outer loop simulations. Ultimately, the three PITEDs that appear most often for each binary classifier for each protocol condition are selected to serve as input features. Use of more than three features does not significantly improve results.

Statistical Significance
Monte Carlo permutation testing is used to assess the statistical significance of the LOOCV accuracies of the binary classifiers. Specifically, a random sample of 10,000 permutations of shuffled labels indicating groups (NC, MCI, or AD) is used to estimate 95% confidence intervals for the probabilities that the LOOCV accuracies obtained are due to chance. The p-values presented are determined using this method.

Three-way classification

A three-way classification scheme is constructed for each protocol condition from binary SVM classifiers using the pairwise coupling approach proposed by Hastie and Tibshirani [54]. For a given record, binary SVM classifiers (i.e., MCI vs. NC, AD vs. NC, and MCI vs. AD) are trained using all other available records and then applied to the given record. If two out of three of the SVM binary classifiers classify a record as belonging to class i, then the final decision of the three-way classifier is to classify the record as belonging to class i. Otherwise, the probability that a record belongs to each class, P_i, $i = 1, 2, 3$, is then estimated as follows, and then the final decision of the three-way classifier is to choose the class corresponding to the largest probability, $\mathrm{argmax}_i(P_i)$.

SVM models are binary classifiers that find the hyperplane in the feature space maximizing the minimum (signed) distance between the hyperplane and training points. The distance from the hyperplane for a given set of features $\boldsymbol{x}$ is given by Equation (4.11), where α_k are weights, K is a kernel function (quadratic), $\boldsymbol{s}_k$ are support vectors (selected subset of vectors of training data features), b is the bias, $k = 1, \dots, N_s$, and N_s is the number of support vectors. If $d < 0$, then the classifier classifies $\boldsymbol{x}$ as class -1 (class i), otherwise as class +1 (class j).

$$d = \sum_{k=1}^{N_s} \alpha_i K(\boldsymbol{s_i}, \boldsymbol{x}) + b \;\; = \;\; \sum_{k=1}^{N_s} \alpha_i \left(0.5 + \boldsymbol{s_i^T x}\right)^2 + b \quad (4.11)$$

The observed conditional probability that a given record will be classified as class i by the ij classifier, $c_{ij} = \mathrm{Prob}(i|i \text{ or } j)$, can be estimated via the distance d as follows. Define $z = d - b$ and let m_i and m_j be the means of z for classes i and j, respectively. Furthermore, define Δ as the standard deviation of $z - (m_i + m_j)/2$. The conditional probability c_{ij} for a given record can then be defined by Equation (4.12), where $\varphi(\mu, \sigma)$ denotes the Gaussian density with mean μ and standard deviation σ:

$$c_{ij} = \frac{\varphi\left(b - \frac{(m_i + m_j)}{2}, \Delta\right)}{\varphi\left(b - \frac{(m_i + m_j)}{2}, \Delta\right) + \varphi\left(b + \frac{(m_i + m_j)}{2}, \Delta\right)} \quad (4.12)$$

In order to determine probabilities p_i, one must define a model for the true conditional probability such as

$$\pi_{ij} = \frac{P_i}{P_i + P_j}. \quad (4.13)$$

One can then use an iterative procedure to estimate the probabilities p_i: (1) Start with an initial guess for each class assuming equal probability, with $\widehat{P_1} = \widehat{P_2} = \widehat{P_3} 0.33$. (2) Compute the corresponding $\widehat{\pi}_{ij}$. (3) Update $\widehat{P_i}$ using Equation (4.14), where N_{ij} is the number of training examples for binary classifier ij. (4) Renormalize $\widehat{P_i}$ such that $\sum \widehat{P_i} = 1$. (5) Repeat steps (2)-(4) until convergence $\widehat{P_1} \rightarrow P_i$ is achieved.

$$\widehat{P}_{i,new} = \widehat{P}_{i,old} \frac{\sum_{i \neq j} N_{ij} c_{ij}}{\sum_{i \neq j} N_{ij} \widehat{\pi}_{ij}}. \quad (4.14)$$

Results for Discrimination of MCI and AD Using Transfer Entropy

Binary Discrimination Results

Two-sample Student's t-distribution tests (unequal variance) are performed on group means of PITEDs selected as features for binary classifiers in order to determine if observed differences are significant enough to infer a linear separability at the population level. Such an inference would require large differences between group means and small variation within groups. It should be noted that inferences are dependent on the assumption of representative samples.

MCI vs. NC.
Results for LOOCV accuracies for each binary classifier are presented in Table 4.1 along with the selected features. Accuracies presented are obtained using all three selected features. For the REO condition, MCI participants demonstrate a lower PITED for occipital region to right frontal region coupled with an increased PITED from the frontal region to the left occipital region, compared to normal controls. An increased central-to-frontal PITED is also observed for MCI participants. Selected features for the counting task all include PITEDs involving the parietal region. Specifically, MCI participants have an

increased right frontal-to-left parietal PITED and decreased parietal-to-left temporal and left parietal-to-left occipital PITEDs. For the REC condition, MCI participants are observed to have significantly increased PITED for left occipital and right frontal regions and between the right temporal and right parietal regions. A decrease in the PITED for central and right temporal regions is also observed. Ninety-five percent confidence intervals for the corresponding p-values are determined via Monte Carlo permutation testing.

LOOCV accuracies of   93.6% (p-value <0.0032), 90.3% (p-value <0.0182), and 87.1% (p-value <0.0321) are achieved for MCI vs. NC discrimination for the REO condtion, counting task, and REC condition, respectively.

AD vs. NC

Compared to normal controls, AD participants demonstrate a significantly greater left temporal-to-frontal PITED coupled with a decrease in frontal-to-left temporal PITED during the REO condition. A greater right occipital-to-left central PITED is also observed for AD participants. A LOOCV accuracy of 93.8% (p-value <0.0043) is achieved for the REO condition based on these differences.

During the counting task, AD participants demonstrate significantly increased PITEDs for right parietal-to-left occipital, left frontal-to-left occipital, and right occipital-to-left occipital. These observations allow for a LOOCV accuracy of 90.6% (p-value <0.0110) for AD vs. NC discrimination during the counting task.

When resting with eyes closed, AD participants demonstrated an increase in occipital-to-left frontal PITED and a decrease in left temporal-to-right central PITED coupled with a decrease in left occipital-to-left temporal PTITED. An accuracy of 87.5% (p-value <0.0324) is achieved for the REC condition.

MCI vs. AD

For the REO condition, AD participants demonstrate a significantly greater left temporal-to-left frontal PITED compared to MCI participants. This appears to closely follow the observation of increased left temporal-to-frontal PITED in AD participants compared to normal controls. Interestingly, during the REO condition, the right occipital-to-left central PITED is greater for AD participants compared to NC participants but lower for AD participants compared to MCI participants. There is also an observed increase in parietal-to-left occipital PITED for AD participants. A LOOCV accuracy of 90.9% (p-value <0.0118) for MCI vs. AD discrimination is achieved based on these observations for the eyes open resting condition.

MCI vs. AD LOOCV accuracies of 84.5% (p-value <0.0195) and 81.8% (p-value <0.0373) are achieved for the counting task and REC condition, respectively. During the counting task, AD participants demonstrate significantly increased right occipital-to-left central PITED compared to MCI participants and NC participants. AD participants also have significantly higher right parietal-to-occipital and left frontal-to-left temporal PITEDs. While resting with eyes closed, AD participants and higher right frontal-to-right temporal, left central-to-occipital, and right parietal-to-occipital PITEDs.

Table 4.1. Group Comparisons of Selected Features for Binary Classifiers

Condition	MCI vs. NC		AD vs. NC		AD vs. MCI	
	Selected Features	Group Means	Selected Features	Group Means	Selected Features	Group Means
REO	O→RF	MCI<NC	LT→F	AD>NC	LT→LF	MCI<AD***
	F→LO	MCI>NC	RO→LC	AD>NC	RO→LC	MCI>AD
	C→F	MCI>NC	F→LT	AD<NC	P→LO	MCI<AD
	acc. (sens., spec.): 93.6% (100%, 86.7%)		acc. (sens., spec.): 93.8% (100%, 86.7%)		acc. (sens., spec.): 90.9% (93.8%, 88.2%)	
	95% CI for p-value: (0.0001, 0.0032)		95% CI for p-value: (0.0031, 0.0043)		95% CI for p-value: (0.0097, 0.0118)	
	Selected Features	Group Means	Selected Features	Group Means	Selected Features	Group Means
Counting task	RF→LP	MCI>NC	RP→LO	AD>NC** *	RP→LO	MCI<AD* *
	P→LT	MCI<NC	RO→LO	AD>NC*	RP→O	MCI<AD* **
	LP→LO	MCI<NC	LF→LO	AD>NC*	LF→LT	MCI<AD*
	acc. (sens., spec.): 90.3% (93.8%, 86.7%)		acc. (sens., spec.): 90.6& (82.4%, 100%)		acc. (sens., spec.): 90.9% (88.2%, 93.8%)	
	95% CI for p-value: (0.00138, 0.0182)		95% CI for p-value: (0.0020, 0.0110)		95% CI for p-value: (0.0032, 0.0195)	
	Selected Features	Group Means	Selected Features	Group Means	Selected Features	Group Means
REC	LO→RF	MCI>NC* *	LT→RC	AD<NC	RF→RT	MCI<AD*
	C→RT	MCI<NC* *	O→LF	AD>NC	LC→O	MCI<AD
	RT→RP	MCI>NC	LO→LT	AD<NC	RP→O	MCI<AD
	acc. (sens., spec.): 87.1% (87.5%, 86.7%)		acc. (sens., spec.): 87.5% (82.4%, 93.3%)		acc. (sens., spec.): 81.8% (100%, 64.7%)	
	95% CI for p-value: (0.0057, 0.0321)		95% CI for p-value: (0.0211, 0.0324)		95% CI for p-value: (0.0162, 0.0373)	

* $p < 0.05$ ** $p < 0.01$, ***$p < 0.001$. Feature designations are preceded by regional indices: LF=left frontal; RF=right frontal; F=frontal; LT=left temporal; RT=right temporal; LC=left central; RC=right central; C=central; LP=left parietal; RP=right parietal; P=parietal; LO=left occipital; RO=right occipital; O=occipital; see Fig. 4.1 for regional boundaries. REO = resting with eyes open; REC = resting with eyes closed.

Three-way Classification Results

A confusion table for three-way classification results for the REO condition is presented in Table 4.2. One participant from each group is misclassified using data from the REO condition: one NC participant is misclassified as AD, one MCI participant is misclassified as NC, and one AD participant is misclassified as MCI. Overall, the accuracy is impressive at 93.8%.

A summary of the three-way classification results for the counting task as presented in Table 4.3. All NC participants are correctly classified. Two MCI participants are misclassified as NC participants. Two AD participants are also misclassified, one as MCI and one as NC. Thus, 100% of those predicted as AD are AD, 93.3% of those predicted to be MCI are MCI, and 83.3% of those predicted to belong to the NC group are actually NC participants. The resulting overall accuracy is 91.7%.

Results for the REC condition are very similar to those of the REO condition and are presented in Table 4.4. Comparing Tables 4.2 and 4.4, the only difference is that a NC participant is misclassified as MCI (eyes closed, Table 4.2) instead of being misclassified as AD (eyes open, Table 4.2). The overall accuracy for the REC condition is thus the same as for the REO condition at 93.8%.

Table 4.2. Confusion Table of 3-Way Results for REO Condition Using PITEDs

		Predicted Classes			
		NC	MCI	AD	
True Classes	NC	14	0	1	93.3%
	MCI	1	15	0	93.8%
	AD	0	1	16	94.1%
		93.3%	93.8%	94.1%	Overall Acc.: 93.8%

Table 4.3. Confusion Table of 3-Way Results for Counting Task Using PITEDs

		Predicted Classes			
		NC	MCI	AD	
True Classes	NC	15	0	0	100%
	MCI	2	14	0	87.5%
	AD	1	1	15	88.2%
		83.3%	93.3%	100%	Overall Acc.: 91.7%

Table 4.4. Confusion Table of 3-Way Results for REC Condition Using PITEDs

		Predicted Classes			
		NC	MCI	AD	
True Classes	NC	14	1	0	93.3%
	MCI	1	15	0	93.8%
	AD	0	1	16	94.1%
		93.3%	88.2%	100%	Overall Acc.: 93.8%

Discussion and Conclusions

In this study, the average of delays that maximized transfer entropy between EEG channel of difference scalp regions are examined as potential biomarkers for detection of alterations in brain functional organization associated with the cognitive decline of MCI and early Alzheimer's disease. A feature selection procedure is used to objectively select average peak inter-regional transfer entropy delays (PITEDs) for use as features in SVM models and binary classification. A three-way classification scheme derived from the binary classifiers is also proposed based on pairwise coupling.

The data in this study included scalp EEG recorded during *resting state* conditions and a *simple cognitive task* of counting backwards by ones. A great advantage of resting state protocols and simple cognitive tasks (i.e., counting backwards) is that they eliminate the need for extra training of primary care personnel in administering complex cognitive tasks. The short length of data required for the analyses (two minutes) is also practical for a primary care setting.

Previous studies have explored various EEG features for the detection of cognitive decline due to MCI or AD. Several of these researchers have observed that features that appear to discriminate AD from NC well, do not necessarily perform well when applied to MCI data [13,63,66]. Often, a different set of features may be required for discriminating between NC, MCI, and AD as features rarely appear to function as a sliding scale with NC at one end, AD at the other, and MCI in the middle [15].

Reduced complexity and perturbations in EEG synchrony may be associated with the cognitive decline of MCI and AD. Recent research exploring the potential for diagnosing MCI and AD from EEG has yielded observations suggesting (1) reduced complexity in EEG and (2) perturbations in EEG synchrony may be associated with cognitive decline due to AD [37,130-135].

Analysis of EEG inter-channel transfer entropy allows for observations of patterns in the complexity and synchrony of EEG data. Specifically, the features proposed here are intended to represent trends in the delay of the transfer of the information present in EEG signals between major regions of the scalp. The successful discrimination between the three groups of EEG records (NC, MCI, and AD) are the result of differences in the dynamics of the information distribution in EEG voltages across the scalp in resting states and during a simple cognitive task. It is possible the observed differences in these information dynamics may be influenced by alterations in the functional organization of the brain as a result of cognitive decline.

In this work, participants are classified at the individual level, which is the case when a patient comes into a doctor's office. Individualized analysis allows these EEG markers to be tested against known biomarkers for Alzheimer's disease and with cognitive tests. A goal of EEG research is the identification of easy neural indicators to diagnose and predict cognitive decline pre-clinically, such as among people with subjective memory complaints.

The results for the three-way discrimination presented here are encouraging, especially those for MCI, as detection of MCI at the earliest possible stage is currently of great interest in the field. The three-way classification scheme presented here allows for the differentiation of the three groups without a priori knowledge that individuals fall into two of the three groups.

The results of this pilot study suggest the potential for the use of features representing inter-regional EEG transfer entropy relationships as a means for objectively discriminating between normal older, MCI, and AD participants. The results suggest that a simple discrimination model utilizing SVM and the features presented here may be a viable

basis for future development of a diagnostic screening tool for early MCI and early AD with applicability in the primary care setting.

CHAPTER 5
NER DISCRIMINATION OF MCI AND AD
USING REGIONAL SPECTRAL AND COMPLEXITY FEATURES

In this Chapter, an exploration of common EEG spectral and complexity measures as potential biomarkers of MCI and early AD is presented. The approach developed is applied toward the discrimination of MCI and AD using EEG recorded during resting states and a simple cognitive task (NER Dataset); see Chapter 1 for more details regarding data collection procedures. This Chapter begins by presenting the common EEG spectral and complexity measures being investigated. Next, the methodology for applying these measures is described. Results are then presented and discussed.

Methodology

As discussed in Chapter 1, various spectral and complexity features have been previously investigated in regards to discrimination of MCI and AD using scalp EEG. Generally, researchers have noted a shift in spectral power toward lower frequencies and a decrease in EEG signal complexity in AD [37]. In this study, common spectral and complexity measures previously investigated are computed on a regional basis for preprocessed EEG taken during NER conditions. Features are examined in order to determine which features, regions, and conditions appear to best discriminate MCI and AD.

The spectral and complexity features examined in this study are listed in Table 5.1. In addition to features computed for preprocessed EEG, a few spectral and complexity features are also computed for the first time derivative of the EEG. Investigation of spectral and complexity feature of the first time derivatives is motivated by the fact that time derivatives of the EEG voltages ($V'(t)$) contain indirect information regarding the time-dependent rate of change of impedance ($Z'(t)$) and distribution of charge (rate of change of current flow, $I'(t)$) in the brain, both of which may be affected by disruption of neural pathways due to disease pathology ($V'(t)= Z'(t)I(t) + I'(t)Z(t)$). A total of 32 features are calculated for each channel: 26 for the preprocessed EEG and 6 for the time derivatives. The features can be divided into two main categories: (1) spectral features and (2) entropy and complexity features.

Spectral Features

Relative spectral power in the θ band (P_θ^r, 3.5—7.5 Hz), α_1 band ($P_{\alpha_1}^r$, 7.5—9.5 Hz), α_2 band ($P_{\alpha_2}^r$, 9.5—12.5 Hz), β_1 band ($P_{\beta_1}^r$, 12.5—17.5 Hz), β_2 band ($P_{\beta_1}^r$, 17.5—25 Hz), and γ band (P_γ^r, 25—40 Hz) are computed. Additional spectral features include total spectral power (P_{total}, 3.5—40 Hz), peak α band frequency (f_{peak}^α), median frequency (f_{med}), and spectral entropy (S_{spec}). Peak α band frequency is defined as the frequency in the range

7.5—12.5 Hz at which the power spectral density curve is maximized. Median frequency is defined as the frequency at which the total spectral power is halved. Spectral entropy is defined as Shannon entropy computed over the normalized power spectral density curve. The mathematical definition for S_{spec} is given by Equation (5.1), where $p(f_i)$ is the probability of occurrence of frequency f_i, $P(f_i)$ is the spectral power at frequency f_i, and P_{total} is the total spectral power (3.5—40 Hz).

$$S_{spec} = -\sum_{i=1}^{k} p(f_i) \ln p(f_i) \approx -\sum_{i=1}^{k} \frac{P(f_i)}{P_{total}} \ln \left(\frac{P(f_i)}{P_{total}} \right) \quad (5.1)$$

Three spectral power ratios are also computed. These ratios are used based on previous observations of increased power in the θ band of EEG taken from MCI and AD individuals [124]. The definitions for these ratios are presented in Equations (5.2)—(5.4).

Table 5.1 Spectral and Complexity Features

Relative Spectral Power Features	**Spectral Power Ratios**
(1) P_θ^r: relative power in θ band	(11) R_1: first ratio
(2) $P_{\alpha_1}^r$: relative power in α_1 band	(12) R_2: second ratio
(3) $P_{\alpha_2}^r$: relative power in α_2 band	(13) R_3: third ratio
(4) $P_{\beta_1}^r$: relative power in β_1 band	
(5) $P_{\beta_2}^r$: relative power in β_2 band	**Entropy/Complexity Features**
(6) P_γ^r: relative power in γ band	(14) A: activity
	(15) M: mobility
Additional Spectral Features	(16) C: complexity
(7) P_{total}: total spectral power	(17) S_{samp}: sample entropy
(8) f_{peak}^α: peak α band freq.	(18) C_{LZ}: Lempel-Ziv complexity
(9) f_{med}: median freq.	
(10) S_{spec}: spectral entropy	

First Derivative Features	
(19) $(P_{total})'$: total spectral power of first derivative	(22) $(S_{spec})'$: spectral entropy of first derivative
(20) $(f_{peak}^\alpha)'$: peak α band freq. of first derivative	(23) $(S_{samp})'$: sample entropy of first derivative
(21) $(f_{med})'$: median freq. of first derivative	(24) $(C_{LZ})'$: Lempel-Ziv complexity of first derivative

$$R_1 = \frac{P_\theta}{P_{\alpha_1} + P_{\alpha_2} + P_{\beta_1}} \quad (5.2)$$

$$R_2 = \frac{P_\theta}{P_{\alpha_1} + P_{\alpha_2} + P_{\beta_1} + P_{\beta_2}} \quad (5.3)$$

$$R_3 = \frac{P_\theta}{P_{\alpha_1} + P_{\alpha_2}} \quad (5.4)$$

Spectral features are computed using the power spectral density of individual channels' records as determined by the Welch Modified Averaged Periodogram Method [88]. In applying Welch's method, a signal is split into overlapping segments of a given length. The overlapping segments have a tapering window applied to them in the time domain that tapers the data at either end. Periodograms are then calculated for each segment by computing the discrete Fourier transform and the squared magnitude of the result. The periodograms are then averaged. In calculating spectral features, two-second segments with 50% overlap are used. Each 2-s segment is modified by a Hanning window (50% cosine taper). Periodograms are then calculated for each 2-s segment and averaged. Choice of window length and tapering window are based on methods for computing other common spectral features of EEG presented by previous researchers [124].

Entropy and Complexity Features

Entropy and complexity measures are also computed, including activity (A), mobility (M), complexity (C), sample entropy (S_{samp}), and Lempel-Ziv complexity (C_{LZ}). The definitions for activity, mobility, and complexity are presented in Equation (5.5), where σ_0 is the variance of the signal, σ_1 is the variance of the first derivative of the signal, and σ_2 is the variance of the second derivative of the signal.

$$A = \sigma_0, \quad M = \sqrt{\frac{\sigma_1}{\sigma_0}}, \quad C = \sqrt{\frac{\sigma_2}{\sigma_1} - \frac{\sigma_1}{\sigma_0}} \quad (5.5)$$

Sample entropy is defined as the negative natural log of the conditional probability that time series of length N, having repeated itself within a tolerance of r for m data points, will also repeat itself for $m + 1$ points. Note that this definition excludes self-matches. One can define N^m as the number of matches of length m and N_{m+1}^m as the subset of N^m that also matches for length m +1. Sample entropy can then be defined mathematically by Equation (5.6). Here, the choice of $m = 2$ and $r = 0.2$ times the standard deviation of the signal are based on approaches presented by previous researchers [124].

$$S_{samp} = -\ln\left(\frac{N_{m+1}^m}{N^m}\right) \quad (5.6)$$

Lempel-Ziv complexity C_{LZ} is a commonly used measure for characterizing the randomness of biomedical signals. To compute C_{LZ}, the numerical sequence (signal) must first be transformed into a symbolic sequence S. The most usual means to do this is to convert the signal into a 1/0 symbolic sequence by comparing the signal to a threshold value, usually the median value of the signal. For example, whenever the signal is larger than the median value, one maps the signal to 1, otherwise, to 0. After mapping the signal into its symbolic 1/0 sequence, the sequence can be parsed to obtain distinct "words", and the "words" can be encoded. Lempel-Ziv complexity can then be defined as the length of the encoded sequence L divided by the length of the signal n.

In order to parse the signal, one can sequentially scan the sequence $S = s_1 s_2 \dots s_n$ and rewrite it as a concatenation $W = w_1\text{-}w_2 \dots w_k$ of k "words" chosen such that $w_1 = s_1$ and w_j is the shortest "word" that has not appeared previously. Thus, $w_j = w_i 0$ or $w_i 1$, where $1 \leq i \leq j\text{-}1$. For example, for the sequence S = 1011010100010, W = 1-0-11-01-010-00-10. The "word" sequence W must then be encoded. This can be done as follows. For each "word" use $\log_2 k$ bits to describe the location of the prefix to each "word" and 1 bit to describe the last bit of the "word". For this example, $k = 7$ words. Thus, one would use 3 bits to describe the prefix location for each word, with 000 being the prefix for an empty set. The encoded sequence would then be (000,1)-(000,0)-(001,1)-(010,1)-(100,0)-(010,0)-(001,0). The length of the encoded sequence L is then equal to $k (\log_2 k + 1)$. Lempel-Ziv complexity can then be defined mathematically by Equation (5.7). When the length of the signal n is very large, $k \leq n/\log_2 n$ and Equation (5.7) reduces to Equation (5.8) [124].

Entropy and complexity features are computed using 5-s windows with 50% overlap and then averaged. Choice of window length is based on methods presented by previous researchers [124].

$$C_{LZ} = \frac{L}{n} = \frac{k (\log_2 k + 1)}{n} \quad (5.7)$$

$$C_{LZ} \approx \frac{k \log_2 n}{n} \quad (5.8)$$

Discrimination of EEG Records

As discussed in Chapter 1, the NER Dataset included NC, MCI, and AD EEG records recorded during three NER protocol conditions: the REO condition, the counting task, and the REC condition. Two-minute samples from each of these three conditions are extracted for analyses.

The 24 features described above and presented in Table 5.1 are calculated for the 2-min samples for each protocol condition. Features are computed for each channel used in analyses. The 30 channels are grouped into 12 scalp regions based on their arrangement and location on the scalp. The regions include: (1) left frontal (LF); (2) right frontal (RF); (3) frontal (F = LF + RF + channel FZ); (4) left temporal (LT); (5) right temporal (RT); (6) left central (LC); (7) right central (RC); (8) central (C = LC + RC + channels FCZ and CZ); (9)

left parietal (LP); (10) right parietal (RP); (11) parietal (P = LP + RP + channels CPZ and PZ); and (12) occipital (O). Note that left and right regions do not include central line channels; see Fig. 4.1 for regional boundaries. A global region (G) comprised of all channels is also considered. Each of the 24 features is averaged over each region (including G) for a total of 13 regional average feature groups.

Feature Selection

The three groups of participants (NC, MCI, and AD) in the NER Dataset provided three binary discrimination problems: MCI vs. NC, AD vs. NC, and MCI vs. AD. Twenty-four features are computed for each of the 13 regions described above for each subject for each protocol condition. Feature selection is performed as follows. For each discrimination problem and each condition, combinations of up to eight features are tested using SVM functions in MATLAB™ [88]. Quadratic kernel functions are used in all discriminations and the cost coefficient is held constant at unity. To help avoid overfitting, *nested* LOOCV loops are used to suggest and test different combinations of features. The inner loop is used to generate a list of suggested combinations of features. The outer loop determines the LOOCV accuracy of the combinations of features suggested by the inner loop. The contribution of individual features is then assessed based on how often they appeared in the best 200 performing combinations tested in the outer loop simulations. Ultimately, the eight features that appear most often are selected for each protocol condition and binary classifier.

Statistical Significance

The statistical significance of LOOCV accuracies obtained using selected features is assessed using Monte Carlo permutation testing. Ten thousand (10,000) permutations of shuffled labels are used to estimate 95% confidence intervals for the probabilities that the LOOCV accuracies obtained are due to chance. The p-values presented are determined using this method. For more on Monte Carlo permutation testing, see work by Thomas and Holmes [143].

Results for Discrimination of MCI and AD
Using Regional Spectral and Complexity Features

For each protocol condition, the selected features for each binary classifier are selected for further analyses. Two-sample Student t-distribution tests (unequal variance) are performed on group means of individual features in order to test linear separability at the population level.. Features for which significant linear separation existed, and the significance of the separability, are indicated in Table 5.2. Given the small sample sizes, such inference required large differences between group means and small variation within groups. It should be noted that such tests are dependent on the assumption of representative samples.

Leave-one-out binary classification accuracies are computed for each binary classifier for each protocol condition. In each case, all eight of selected features listed in Table 5.2 are employed in combination using a quadratic SVM model. The results are summarized in Table 5.2 where 95% confidence intervals for corresponding p-values of the resulting LOOCV accuracies are assessed using Monte Carlo permutation testing.

MCI vs. NC

For both the REO protocol condition and the counting task, MCI patients demonstrate a significant increase in total power in the central region (C-P_{total}) compared to normal controls. While resting with eyes open, the MCI group's data show a decrease in alpha and beta activity in the first derivative for the right frontal (RF) and parietal (P) regions, as evidenced by a significant decrease in the median frequency in the right frontal region (RF-f_{med}) and peak alpha frequency in the parietal region (P-$(f_{peak}^{\alpha})'$). A significant decrease in the alpha and beta activity of the first derivative is also observed in the right frontal region (decreased RF-$(f_{med})'$) during the counting task. MCI participants also demonstrate a significant increase in the activity measure (A) in the central region (C) during the counting task. When resting with eyes closed, MCI participants exhibit increased theta activity in the central (C) and left temporal (LT) regions coupled with decreased higher beta band activity in the left frontal (LF) region compared to NC participants, although these differences are not substantial enough to allow statistical inferences regarding linear separability at the population level. Significant differences for MCI participants while resting with eyes closed included a decrease in the sample entropy of the first derivative (C-$(S_{samp})'$), a decrease in total power in the left parietal regions (LP-P_{total}), and an increase in gamma band activity on a global level (G-P_{γ}^{r}).

LOOCV discrimination accuracies of 96.8% (p<0.0014), 83.9% (p<0.0029), and 93.6% (p<0.0003) are achieved for MCI vs. NC discrimination for the REO condition, counting task, and REC conditions, respectively.

AD vs. NC

A LOOCV accuracy of 84.4% (p<0.0043) is achieved for AD vs. NC discrimination during the REO condition. Group differences in selected features indicate a significant increase in the total power of the first derivative in the frontal region (F-$(P_{total})'$) and a decrease in spectral entropy of the first derivative in the left parietal region (LP-$(S_{spec})'$) for AD participants. AD participants also demonstrated an increase in complexity in the left temporal region (LT-C). Increases in theta activity and decreases in alpha and beta activity are also observed in the frontal (F) regions, though groups are not linearly separable at a significant level for these features.

While counting backwards with eyes closed, AD patients are observed to have a significant increase in total power (P_{total}) and activity (A) in the frontal region (F) compared to normal controls, including a significant increase in total power of the first derivative in the right frontal region (RF-$(P_{total})'$). Increases in theta activity are also observed in the left temporal (LT) and parietal (P) regions; however group differences are

not significantly linearly separable. A LOOCV accuracy of 96.9% (p-value<0.0003) is achieved for AD vs. NC discrimination during the counting task.

For the REC condition, the AD group data show significant increases in the total power (LC-P_{total}) and activity (C-A) in the central region compared to normals. In addition, AD participants are also observed to have a significant decrease the total power of the first derivative in the right temporal region (RT-$(P_{total})'$). Increases in theta activity in the central (C) region and a decrease in sample entropy in the occipital (O) region are also observed in AD data, although differences are not linear. A LOOCV accuracy of only 71.9% (p-value<0.0333) is achieved for the REC condition.

AD vs. MCI

Differences between MCI and AD patients while resting with eyes open include a significant increase in total power in the right temporal region (RT-P_{total}), total power of the first derivative in the frontal region (F-$(P_{total})'$), and sample entropy of the first derivative in the left frontal region (LF-$(S_{samp})'$) for AD participants. In addition, AD participants are observed to have lower gamma activity in the right frontal (RF) and left temporal (LT) regions, decreased alpha and beta activity in the left temporal (LT) region, and increased alpha and beta activity in the right parietal (P) and occipital (O) regions. These differences, however, do not significantly deviate in a linear manner from patterns observed for MCI participants. During the counting task, AD participants demonstrate significant increases in total power in the right central region (RC-P_{total}) and activity (A) in the right central (RC) and parietal (P) regions. Less significant differences include increased alpha activity in the central regions and decreases in alpha activity and complexity in the left frontal and occipital regions, respectively. While resting with eyes closed, AD participants again demonstrate significant increases in total power (P_{total}) in the central (C) regions. This is accompanied by a significant increase in activity in the left temporal region (LT-A). AD participants also have decreased beta activity in the right central (RC) and frontal (F) regions.

LOOCV discrimination accuracies of 90.9% (p<0.0136), 90.9% (p<0.0081), and 87.9% (p<0.0063) are achieved for AD vs. MCI discrimination for the ERO condition, counting task, and REC conditions, respectively.

Discussion and Conclusions

In this study, regional spectral and complexity features of scalp EEG recorded during *resting state* conditions and a *simple cognitive task* of counting backwards by ones are explored as potential biomarkers for discriminating among NC, MCI and AD groups. Resting state protocols and a simple cognitive task (i.e., counting backwards) eliminates the need for extra training of primary care personnel in administering complex cognitive tasks. Good results are demonstrated from analyzing short data segments (2 min), practical for a primary care setting.

Table 5.2. Group Comparisons of Selected Spectral and Complexity Features

Condition	MCI vs. NC		AD vs. NC		AD vs. MCI	
	Selected Features	Group Means	Selected Features	Group Means	Selected Features	Group Means
REO	$C\text{-}P_\theta^r$	MCI>NC	$RC\text{-}(f_{peak}^\alpha)'$	AD<NC	$F\text{-}(P_{total})'$	AD>MCI***
	$C\text{-}P_{total}$	MCI>NC***	$RF\text{-}f_{med}$	AD<NC	$LF\text{-}(S_{samp})'$	AD>MCI**
	$RC\text{-}S_{samp}$	MCI<NC	$F\text{-}S_{samp}$	AD>NC	$RF\text{-}P_\gamma^r$	AD<MCI
	$RF\text{-}f_{med}$	MCI<NC	$F\text{-}(P_{total})'$	AD>NC***	$LT\text{-}P_\gamma^r$	AD<MCI
	$RF\text{-}(f_{med})'$	MCI<NC***	$LF\text{-}P_\theta^r$	AD>NC	$LT\text{-}f_{med}$	AD<MCI
	$P\text{-}(f_{peak}^\alpha)'$	MCI<NC**	$LF\text{-}P_{\beta_2}^r$	AD<NC	$O\text{-}P_{\beta_1}^r$	AD>MCI
	$RP\text{-}(P_{total})'$	MCI<NC	$LT\text{-}C$	AD>NC*	$RP\text{-}P_{\alpha_1}^r$	AD>MCI
	$G\text{-}S_{spec}$	MCI<NC	$LP\text{-}(S_{spec})'$	AD<NC**	$RT\text{-}P_{total}$	AD>MCI***
	acc. (sens., spec.): 96.8% (93.8%, 100%) 95% CI for p-value: (0.0002, 0.0014)		acc. (sens., spec.): 84.4% (88.2%, 80.0%) 95% CI for p-value: (0.0021, 0.0043)		acc. (sens., spec.): 90.9% (82.4%, 100%) 95% CI for p-value: (0.0094, 0.0136)	
	Selected Features	Group Means	Selected Features	Group Means	Selected Features	Group Means
Counting task	$C\text{-}P_{\alpha_1}^r$	MCI<NC	$RC\text{-}(f_{peak}^\alpha)'$	AD<NC	$C\text{-}P_{\alpha_1}^r$	AD>MCI
	$C\text{-}P_{total}$	MCI>NC***	$F\text{-}P_{total}$	AD>NC***	$RC\text{-}P_{\alpha_1}^r$	AD>MCI
	$C\text{-}f_{peak}^\alpha$	MCI>NC	$F\text{-}A$	AD>NC***	$RC\text{-}P_{total}$	AD>MCI***
	$C\text{-}A$	MCI>NC***	$LF\text{-}P_{total}$	AD>NC***	$RC\text{-}A$	AD>MCI***
	$LC\text{-}P_{total}$	MCI>NC***	$RF\text{-}f_{peak}^\alpha$	AD>NC	$RC\text{-}S_{samp}$	AD<MCI
	$RC\text{-}R_3$	MCI>NC	$RF\text{-}(P_{total})'$	AD>NC***	$LF\text{-}P_{\alpha_1}^r$	AD<MCI
	$RF\text{-}(f_{peak}^\alpha)'$	MCI<NC**	$LT\text{-}R_3$	AD>NC	$O\text{-}C_{LZ}$	AD<MCI
	$O\text{-}(f_{med})'$	MCI<NC***	$P\text{-}R_1$	AD>NC	$P\text{-}A$	AD>MCI***
	acc. (sens., spec.): 83.9% (93.8%, 73.3%) 95% CI for p-value: (0.0011, 0.0029)		acc. (sens., spec.): 96.9& (100%, 93.3%) 95% CI for p-value: (0, 0.0003)		acc. (sens., spec.): 90.9% (88.2%, 93.8%) 95% CI for p-value: (0.0049, 0.0081)	

Condition	MCI vs. NC		AD vs. NC		AD vs. MCI	
	Selected Features	Group Means	Selected Features	Group Means	Selected Features	Group Means
REC	$C\text{-}R_1$	MCI>NC	$C\text{-}P_{total}$	AD>NC***	$C\text{-}P_{total}$	AD>MCI***
	$C\text{-}(S_{samp})'$	MCI<NC***	$C\text{-}R_1$	AD>NC	$LC\text{-}P_{total}$	AD>MCI***
	$LC\text{-}P_{total}$	MCI>NC***	$C\text{-}R_3$	AD>NC	$RC\text{-}P^r_{\beta_1}$	AD<MCI
	$LF\text{-}P^r_{\beta_2}$	MCI<NC	$C\text{-}A$	AD>NC***	$RC\text{-}P^r_{\beta_2}$	AD<MCI
	$LF\text{-}R_2$	MCI<NC	$LC\text{-}P_{total}$	AD>NC***	$F\text{-}P^r_{\beta_1}$	AD<MCI
	$LT\text{-}R_2$	MCI>NC	$RC\text{-}P_{total}$	AD>NC***	$RF\text{-}(f^\alpha_{peak})'$	AD>MCI
	$LP\text{-}P_{total}$	MCI<NC***	$O\text{-}S_{samp}$	AD<NC	$LT\text{-}A$	AD>MCI***
	$G\text{-}P^r_\gamma$	MCI>NC***	$RT\text{-}(P_{total})'$	AD<NC***	$LP\text{-}(S_{samp})'$	AD>MCI
	acc. (sens., spec.): 93.6% (100%, 86.7%) 95% CI for p-value: (0, 0.0003)		acc. (sens., spec.): 71.9% (64.7%, 80.0%) 95% CI for p-value: (0.0314, 0.0333)		acc. (sens., spec.): 87.9% (88.2%, 87.5%) 95% CI for p-value: (0.0035, 0.0063)	

* p< 0.05 ** p<0.01, ***p<0.001. Feature designations are preceded by regional indices: LF=left frontal; RF=right frontal; F=frontal; LT=left temporal; RT=right temporal; LC=left central; RC=right central; C=central; LP=left parietal; RP=right parietal; P=parietal; O=occipital; G=global. See Table 1 for feature designations; see Fig. 4.1 for regional boundaries. REO = resting eyes open; REC = resting eyes closed.

Previous studies have explored various EEG features for the discrimination of MCI and AD from normal individuals. Several of these researchers have observed that features which appear to discriminate AD from NC well, do not necessarily perform well when applied to MCI data [63,66,159]. While it would be convenient to have features that operate with normals at one extreme value, AD at the other extreme, and MCI somewhere in the middle, thus making the three groups clearly and linearly separable with a clear linear pattern of progression, that is often not the case. Instead, MCI individuals often appear to be spread across boundaries that otherwise clearly discriminate AD from normal participants. A different set of features may, therefore, be required for discriminating between MCI vs. NC, AD vs. NC, and MCI vs. AD [42].

Three generally accepted trends in the literature for MCI and AD discrimination via EEG are: (1) a shift in the power spectrum toward the lower frequencies (delta and theta band) and occasional observations of increased gamma band activity, coupled with a

decrease in alpha and beta band activity; (2) decreased complexity; and (3) decreased synchronization [37,130-135]. These trends, however, are generally reported as global trends observed during REO protocol conditions. Trends in the complexity and spectral power distribution of the first derivative of EEG for MCI and AD are less well established. Furthermore, patterns may differ at different parts of the brain. The features selected to serve as discriminating features for the binary classifiers are examined for trends between groups. For the REC condition, consistent results (i.e., decreased complexity, decreased alpha and beta band activity) are observed, however these trends statistically significant at the population level.

As stated in [37], evidence of the diagnostic utility of resting EEG in dementia and mild cognitive impairment (MCI) is still not sufficient to establish this method for the initial evaluation of subjects with cognitive impairment in the routine clinical practice. In addition, AD EEG studies have been done at the group level. Much work has been done showing group differences, i.e. AD brains differ from those of the normal brains, but differences are not sufficient to categorize individuals. In this work, participants are classified at the individual level, which is the case when a patient comes into a doctor's office. Individualized analysis allows these EEG markers to be tested against known biomarkers for Alzheimer's disease and with cognitive tests. A goal of future work is to be able to use easy neural indicators to diagnose and predict cognitive decline pre-clinically, such as among people with subjective memory complaints.

Previous researchers have attempted to identify globally-averaged spectral features which appear to demonstrate significant robustness in discriminating normal individuals from those with dementia. Unfortunately, dementia can cause different neurological changes in different individuals—especially in the case of more enigmatic diagnoses such as MCI. Such differences may lead to the failure in the generalization of globally-averaged measures to other data sets. While most of the features employed here have been used before on either a global or individual channel basis, here differences in the features' values on a topographical regional basis are examined. The topographical regions do not necessarily correspond to the cortical location of the source of the brain activity; e.g., activity recorded at a central electrode site may reflect a source from the frontal cortex. One goal of this work is to discover regional differences in common EEG features to be potential indicators for cognitive degeneration. In addition, the discriminating power of different features for different protocols, including resting protocols—eyes open and eyes closed—and a simple cognitive task are examined.

This study explores differences in common spectral and complexity measures of EEG on a regional and global basis for the discrimination of preclinical dementia from the normal aging condition. The successful discrimination between the three groups of EEG records (NC, MCI, and AD) are the result of differences in regional electrical activity in specific frequency bands in resting states and during a simple cognitive task.

The observation of increased theta activity and decreases in alpha and beta activity for MCI and AD participants compared to normal controls during the REC condition are consistent with expected trends from the literature [37]. MCI participants demonstrate

increased gamma activity on a global level (G-P_γ^r), coupled with increases in theta activity in the left temporal (LT) and central (C) sites. The AD group demonstrate increased theta activity in the central (C) site coupled with an increase in activity (A) and total power in the central region (C-P_{total}). The alpha waves are typically produced by anyone sitting quietly with eyes closed in the resting state.

The MCI participants demonstrate greater total power (P_{total}) and activity (A) in the central (C) regions, and increased lower frequency activity in the first derivative during the eyes open condition and counting task. When resting with eyes open, the AD group demonstrate few significant differences, however increased theta activity and decreased beta activity compared to normal controls are observed. When counting backwards, AD data demonstrate significant increases in the total power of EEG in the frontal region (F-P_{total}) and its first derivative in the right frontal region (RF-$(P_{total})'$). In addition, increased theta activity is observed in the left temporal (LT) and parietal (P) regions.

The results of this pilot study suggest the potential for the use of regional and global spectral and complexity features representing scalp electrical activity as a means for objectively discriminating between normal older, MCI, and AD participants. The results suggest that a simple discrimination model utilizing SVM and the features presented here may be a viable basis for future development of a diagnostic screening tool for early MCI and early AD with applicability in the primary care setting. Such a rapid, simple, and cost-effective tool could also prove useful in the drug discovery process.

CHAPTER 6
NER DISCRIMINATION OF MCI AND AD
USING INTER-CHANNEL COHERENCE GRAPHICAL NETWORKS

In this Chapter, a method for quantifying differences in EEG inter-channel synchronization for MCI and AD is presented. The method developed involves analyzing inter-channel coherence measures via graph theory. The method is applied toward the discrimination of MCI and early AD using EEG recorded during resting states and a simple cognitive task (NER Dataset); see Chapter 1 for more details regarding data collection procedures. This Chapter begins with a brief introduction to graphical networks. Next, the methodology for developing coherence-based graphical networks of EEG activity and extracting meaningful features capable of characterizing differences in MCI and AD is described. Finally, results obtained for discrimination of MCI and AD EEG records are presented and discussed.

Introduction to Graphical Networks

Graphical Networks in Dementia

Symptoms of dementia are caused by the death of cortical neurons and cholinergic deficits (among other concomitants) that subsequently cause a loss of local and global neuronal connectivity in the brain [25,70,122,127]. The neurons of the brain constitute an extremely complex structural network responsible for phenomena as abstract as consciousness, emotion, and memory. The organization of neurons in the brain provides the physiological basis for information processing. One means of attempting to quantify the structural and functional organization of the brain is the application of graph theory to electromagnetic measures of physiological brain activity such as functional MRI (fMRI) and EEG.

Recent research has demonstrated that the behavior in complex systems (e.g., the human brain) is shaped by the interactions among the network's constituent elements [27]. Brain networks characteristically demonstrate small-world behavior, or clustering [17,47,112,129,133]. Small-world behavior is the occurrence of highly connected clusters of nodes within a larger network. Brain network connections are known to exist on a microscopic level (neurons) and macroscopic level (inter-regional) [27]. Connections between nodes in a graphical network are typically based on some measure of association between nodes. In the brain, the probability of connections existing between nodes in a network representing structural (neuronal) connectivity is highly negatively correlated with the physical spatial distance between nodes [10,23,56]. For network models of functional connectivity, however, the relationship between functional connectivity and physical spatial distance is more weakly correlated, as nonadjacent regions of the brain may function in concert during certain cross-modal tasks. For example, previous

investigations of network graphs derived from fMRI measures have revealed that functionally- and anatomically-related brain regions are more densely connected, suggesting that connection density between nodes is likely a function of both physical spatial distance (anatomical relationships) and level of functional codependence [43,92,116].

In analyzing changes in human brain organization in dementia, fMRI and EEG networks have clear differences. Functional MRI has the best spatial resolution (on the order of millimeters) but poor temporal resolution (on the order of seconds), which restricts measurable bandwidth. Functional MRI measures response-related hemodynamics rather than directly measuring neuronal activity. The nodes used in fMRI networks are anatomically localized regions or voxels in fMRI images. Such nodes allow for various physiological measures for which the association of time series data may be capable of assessing both structural and functional connectivity [27]. Conversely, scalp EEG has poor spatial resolution, but is capable of larger bandwidths (e.g., 0-500 Hz). Typically, EEG electrodes are used as nodes in network graphs. EEG is not well suited to the study of structural organization in the brain. EEG also has its own inherent limitations as a method of quantifying functional brain organization due to diffusion of voltage in EEG—namely, different electrodes at different locations across the scalp may be affected by similar sources. For example, eye blink and other muscular artifacts are commonly found in electrodes' signals regardless of position on the scalp. Despite these limitations, EEG is still capable of measuring patterns in neuronal electrical activity more directly than fMRI [27].

Construction of Graphical Networks

Graphical networks are constructed via the following four steps. First, network nodes are defined. Network nodes can be defined as anatomically defined regions of histological, MRI, or diffusion tensor imaging data. They can also be defined as electroencephalography electrodes in the case of EEG [113]. Defining network nodes is the most essential aspect of creating a graphical network, so care should be taken in choosing nodes that have physiological significance. Time series data should be collected for each node.

Second, a measure of association between the time series of the nodes is defined. The measure of association could be spectral coherence, a causality measure, or simply a correlation coefficient between the two time series. Other examples include connection probability between two regions of diffusion tensor imaging data or a measure of the accuracy in reconstruction one of the node's time series using the other node's time series [113]. The measure of association should be computed for all pairwise combinations of nodes in order to form an association matrix, where each row and column corresponds to a given node. The association matrix will thus be a symmetric (two-way connections) or antisymmetric (one-way connections) matrix and its diagonal will generally be composed of ones (perfect association between a node's time series and itself).

Third, a threshold for the measure of association indicating significantly strong associations should be applied to the association matrix. If an element in the association

matrix is greater/lower than the threshold, then the connection between the two nodes corresponding to that element is said to exist; otherwise, the connection between the two nodes is said to be "severed." If the choice of measure of association allows for positive and negative values, the threshold can also be applied to the absolute value. The choice of threshold is critical, as too lax a threshold allows for a network with potentially many connections while too strict a threshold may cause too few connections for meaningful information to be extracted from the network. Ideally, the choice of threshold value is motivated by other information; however, often a variety of threshold values are tested and a value is chosen empirically. The existing connections (those passing the threshold criterion) may be thought of as roadways in a city map, with nodes being buildings or other landmarks in the city.

Fourth, weights should be assigned to all existing connections in the network. The weight of a connection may simply be the corresponding value of the association matrix or may be a value based on other information. If the weights for the existing connections in a network can have different sign, then the signs are generally interpreted as one-way connections, with positive signs indicating the direction of travel (information flow). Thus, if the weights vary in sign, then the weight matrix will be antisymmetric. If all weights have the same sign, all connections are generally assumed to be two-way and the weight matrix will be symmetric. Using the analogy of the city map, the weights may be interpreted as mileage, toll fees, etc. After having constructed the network, network parameters of interest may by calculated.

Methodology

Coherence Measures

The data used in this analysis include NC, MCI, and AD EEG records from the NER Dataset. As described in Chapter 1, the NER Dataset consisted of three separate protocol conditions: the REO condition, the counting task, and the REC condition. For each protocol condition, samples of 2 min duration are extracted for analyses. Each record contains 30 electrodes (32 channels with 2 ocular channels excluded).

Inter-channel coherence is computed for all pairwise combinations of the 30 electrodes for all 3 protocol conditions using coherence functions in MATLAB™ [88]. Magnitude squatted coherence is defined by Equation (6.1):

$$C_{xy} = \frac{|P_{xy}(f)|^2}{P_{xx}(f)P_{yy}(f)}, \quad (6.1)$$

where P_{xy} is the cross-power spectral density, P_{xx} and P_{yy} are the auto-power spectral densities of electrodes x and y, respectively, and f is frequency. Coherence was computed using the Welch Modified Averaged Periodogram Method with windows of 2 s and 50%

overlap. A 50% cosine taper is applied to each window. Choice of window length and tapering window are based on methods for computing other common spectral features of EEG presented by previous researchers [124].

Mean coherence values ($\bar{C}_{xy}$) are determined for 4 physiologically relevant frequency bands: (1) delta-theta (δ, 0—7.5 Hz), (2) alpha (α, 7.5—12.5 Hz), (3) beta (β, 12.5—25 Hz), and gamma (γ, 25—40 Hz). These four mean coherence values are used to determine connections in graphical network representations of inter-channel coherence.

Inter-Channel Coherence Networks

A graphical network representation of inter-channel coherence is constructed for each of the four frequency bands. Nodes in each network are defined as the EEG electrode channels. Mean coherence values for coherence values for corresponding frequencies are used as measures of associations between nodes. Weights are assigned to all pairwise connections in the networks and are equal to the complement of the mean coherence values. For example, for a mean coherence value between channels x and y among α band frequencies ($\bar{C}_{xy}^{\alpha}$), the corresponding weight $w_{xy}^{\alpha} = 1 - \bar{C}_{xy}^{\alpha}$. Thus, the *lower* the weight, the *stronger* the coherence of the given frequency activity between two electrodes. Thresholds of 0.567, 0.481, 0.402, and 0.303 are applied to weights of the δ, α, β, and γ band networks, respectively. Connections with weights *below* these thresholds are included while connections with weights greater than these thresholds are severed. The choice of thresholds is based on the observation that 75% of weights among all participants are above the thresholds.

Sixteen features are computed for each of the 4 network graphs corresponding to the 4 frequency bands for a total of 64 features; see Table 6.1 for a list of network features computed. The set of features includes 4 global network features and 12 regional network features.

Global Network Features
The first global network feature is connection density (D). Connection density is defined as the percentage of possible connections that passed the threshold significance criterion and are actually present in the network (existing connections). Other global features include statistical features summarizing the distribution of existing connections' weights. Specifically, the maximum likelihood estimates of the scale (A) and shape (B) parameters for a Weibull distribution fit of the weights' probability density function (PDF) are determined. These parameters allow for analysis of the general trends in the strength of coherence between significant (existing) connections.

An additional global network feature is the mean number of nodes ($\bar{N}$) in the shortest existing pathways between nodes. Given the severing of connections via the threshold criterion, a pathway did not necessarily exist between any two given nodes. Furthermore, given that the length of a pathway is equal to the sum of the weights of connections in a pathway and that the weights are equal to the complement of the

Table 6.1. Inter-Channel Coherence Graphical Network Features

(1)	D	Connection density
(2)	A	Scale parameter of Weibull distribution fit of weights
(3)	B	Shape parameter of Weibull distribution fit of weights
(4)	$\overline{N}$	Mean number of nodes in shortest existing pathways
(5)	H_C	Mean hub order in central (C) region
(6)	H_F	Mean hub order in frontal (F) region
(7)	H_L	Mean hub order in left temporal (L) region
(8)	H_O	Mean hub order in occipital (O) region
(9)	H_P	Mean hub order in parietal (P) region
(10)	H_R	Mean hub order in right temporal (R) region
(11)	K_C	Mean clustering coefficient in central (C) region
(12)	K_F	Mean clustering coefficient in frontal (F) region
(13)	K_L	Mean clustering coefficient in left temporal (L) region
(14)	K_O	Mean clustering coefficient in occipital (O) region
(15)	K_P	Mean clustering coefficient in parietal (P) region
(16)	K_R	Mean clustering coefficient in right temporal (R) region

coherence between nodes, the shortest pathway between two nodes is also the pathway of strongest coherence between constituent nodes in the pathway. Because coherence is a measure of the correlated general trends of two time series at a given frequency, it is also a measure of mutual information between frequency activities of the two time series. Viewed in this context, the shortest pathway between two nodes is both the pathway of strongest coherence and the pathway of greatest mutual information in the specific frequency band for the given start and end nodes. The mean number of nodes in the shortest existing pathways is therefore an average measure of the interdependence of mutual information among connected nodes in the given frequency range.

Regional Network Features

In addition to the four global network features just described, hub order and clustering coefficients are also examined on a regional basis. Hub order (H) for a given node is defined as the number of existing shortest pathways that include the node while excluding pathways that begin or end at the given node. Clustering coefficient (K) for a given node is a measure of the connection density among local nodes. In this study, clustering coefficient for a given node is defined as the number of direct connections between the directly connected nodes divided by the number of possible connections between directly connected nodes. Both hub order and clustering coefficients are computed for each of the 30 nodes and are averaged over the same 6 scalp regions used in the event-related Tsallis entropy analyses: central (C), frontal (F), left temporal (L), parietal (P), occipital (O), and right temporal (R). See Fig. 2.1 for a diagram of the region boundaries.

Implications of Network Features' Values

The implications of the values of the chosen network features regarding the EEG electrical activity are summarized in Table 6.2, where the superscript (f) denotes the frequency band and the subscript (r) denotes the region (if applicable). A low connection density (D) value is indicative of low global coherence and implies diverse sources for the recorded electrical activity in the given frequency band. Conversely, high D is indicative of high global coherence and greater uniformity in the electrical activity in the given frequency band.

The weight's PDF scale parameter (A) has the opposite relationship, with a low value implying high coherence and a high value implying low coherence. The PDF shape parameter (B) is indicative of the variation in coherence values, with a low value suggesting low variation and a high value suggesting high variation. The mean number of

Table 6.2. Implications of Inter-channel Coherence Graphical Network Features' Values

Feature	Value	Direct implications for coherence	Implications for f band electrical activity
(1) D^f	low	low global coherence	lower uniformity
	high	high global coherence	greater uniformity
(2) A^f	low	high mean coherence	greater uniformity
	high	low mean coherence &/OR high variation in coherence	low uniformity
(3) B^f	low	low variation in coherence	--
	high	high variation in coherence	--
(4) $\bar{N}^f$	low	high interdependence of coherence	greater uniformity
	high	low interdependence of coherence	low uniformity
(5)-(10) $\bar{H}_r^f$	low	coherence in region r has low interdependence of with other regions	low uniformity &/OR possible localized source of f band activity near/ within region r
	high	coherence in region r has high interdependence of with other regions	greater uniformity
(11)-(16) $\bar{K}_r^f$	low	low coherence within region r	--
	high	high coherence within region r	possible localized source of f band activity near/within region r

nodes in the shortest existing pathways ($\bar{N}$), as mentioned previously, serves as a measure of the interdependence of coherence values, with a larger mean number of nodes indicating lower interdependence. Generally, low interdependence in coherence values can be interpreted as implying low uniformity in electrical activity in the given frequency band.

Regional mean hub orders ($\bar{H}_r^f$) also indicate interdependence of coherence, but on a regional rather than global scale. These values can be interpreted as indicating the relative interdependence of the given region's coherence with the other regions. Thus, low $\bar{H}_r^f$ could imply low global uniformity in electrical activity or a possible localized source of electrical activity in the given frequency band near or within the specific region. High $\bar{H}_r^f$ is indicative of greater global uniformity in the given frequency band activity.

Finally, regional mean clustering coefficients ($\bar{K}_r^f$) serve as indicators of intraregional coherence, with high values suggesting the possibility of a localized source for given frequency activity.

Discrimination of EEG Records

Feature Selection
The three groups of participants (NC, MCI, and AD) in the NER Dataset provided three binary discrimination problems: MCI vs. NC, AD vs. NC, and MCI vs. AD. Sixteen network features are computed for four network graphs based on mean inter-channel coherence for δ, α, β, and γ frequency bands. Thus, a total of 64 features are computed for each subject for each protocol condition. Feature selection is performed in order to assess the contribution of individual features to discrimination performance for each binary discrimination problem and each protocol condition. Feature selection is performed as follows. For each discrimination problem and each condition, combinations of up to 8 of the 64 features are tested using SVM functions in MATLAB™ [88]. Quadratic kernel functions are used in all discriminations and the cost coefficient is held constant at unity. To help avoid overfitting, *nested* LOOCV loops are used to suggest and test different combinations of features. The inner loop is used to generate a list of suggested combinations of features. The outer loop determined the LOOCV accuracy of the combinations of features suggested by the inner loop. The contribution of individual features is then assessed based on how often they appear in the best 200 performing combinations tested in the outer loop simulations. Ultimately, the six features that appear most often are then tested in combination.

Statistical Significance
The statistical significance of results obtained using the six selected features chosen via feature selection is assessed using Monte Carlo permutation testing. Random samples of 10,000 permutations of shuffled labels are used to estimate 95% confidence intervals for the probabilities that the LOOCV accuracies obtained are due to chance. The p-values presented are determined using this method. For more on Monte Carlo permutation testing, see work by Thomas and Holmes [143].

Results for Discrimination of MCI and AD
Using Inter-channel Coherence Graphical Network Features

A summary of the feature selection results is presented in graphical form in Fig. 6.1, where a color scale is used to indicate the inclusion of given features in the 200 best performing combinations. For example, 100% would indicate that a given feature is included in all of the 200 best performing combinations; 50% indicates inclusion in half of the 200 best performing combinations; etc. As can be seen in Fig. 6.1, for most binary classification problems and conditions, a few features are clearly highlighted as being highly discriminatory (highly inclusive). One notable exception is the discrimination of MCI vs. NC participants while counting backwards with eyes closed. As seen in Fig. 6.1, no set of features is capable of clearly distinguishing the two groups' EEG frequency activity during the given task. Statistical analyses reveal that this failure is due to high variability among feature values within each group, suggesting that the task of counting backwards with eyes closed may be ill-suited for discriminating between MCI and NC participants based patterns on inter-channel coherence relationships.

For each protocol condition and discrimination problem, the six features with the highest inclusivity among feature selection results are selected for further analyses. Firstly, all six features are tested in combination. The results are summarized in Table 6.3. Ninety-five percent confidence intervals for corresponding p-values of the resulting LOOCV accuracies are estimated using Monte Carlo permutation testing.

Additionally, two-sample student t-distribution tests (unequal variance) are performed on group means of individual features in order to determine whether differences between the given samples are great enough to statistically infer linear separability in the groups' populations (90% confidence). Features for which such an inference can be made are indicated with † in Table 6.3. Given the small sample sizes, such inference require large differences between group means and small variation within groups. It should be noted that such tests are dependent on the assumption of representative samples.

Finally, the potential implications of differences in EEG electrical activity between groups are assessed for each feature for which differences in population means could be inferred with statistical significance. These observations are summarized in Table 6.3.

MCI vs. NC Results
When resting with eyes open, MCI participants demonstrate greater interdependence of α activity in the central region with other regions, greater interdependence of β activity of the frontal region with other regions, and greater localization of β activity in the occipital region compared to normal controls. These observations suggest overall greater uniformity in α activity and greater localization in β activity for MCI participants compared to NC participants. The REO condition also
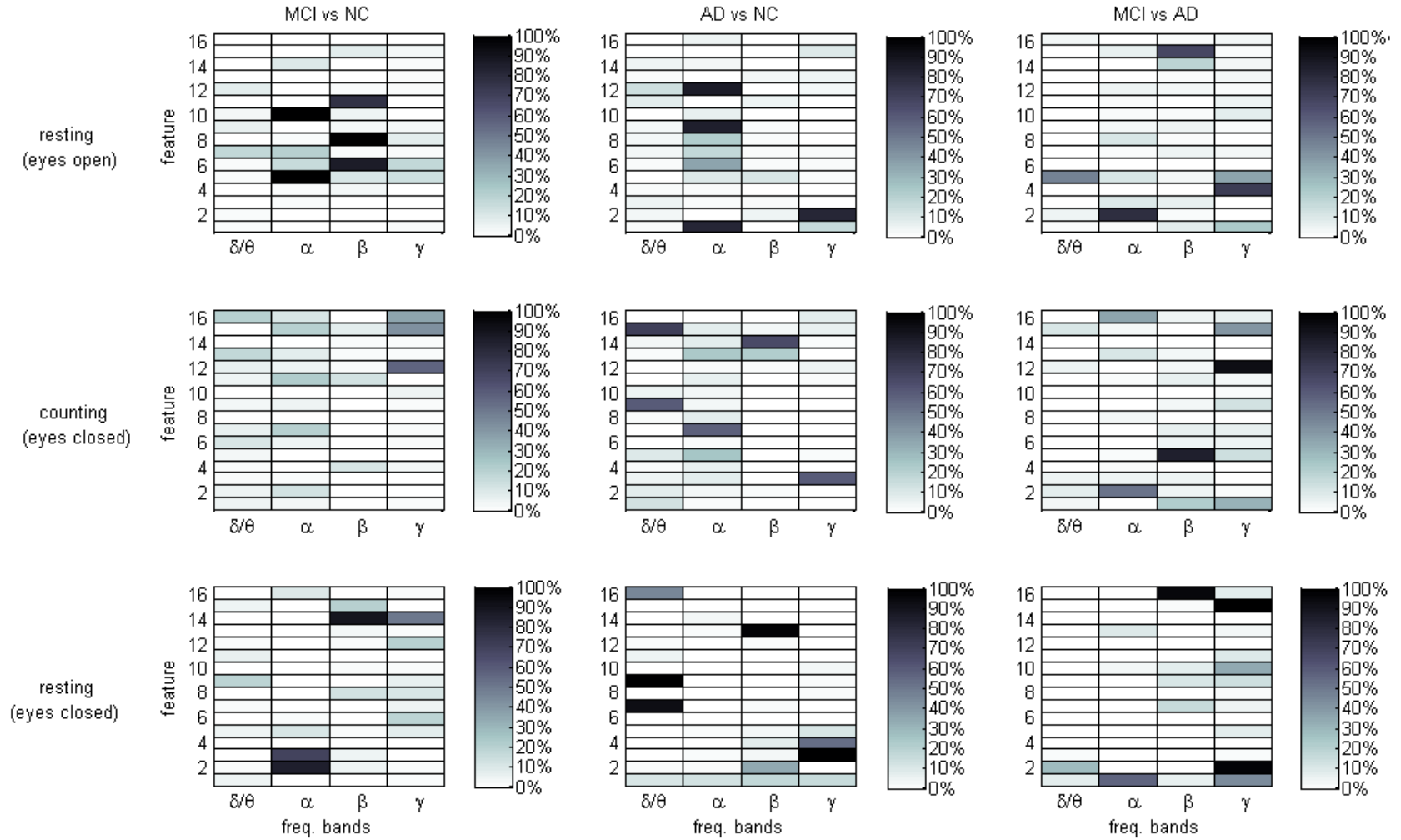
Fig. 6.1. Inter-Channel Coherence Graphical Networks' Feature Selection Results. Color scale indicates the inclusion of given features in the 200 best performing combinations for the given protocol condition and binary discrimination problem.

demonstrated the greatest accuracy in MCI vs. NC discrimination, with a LOOCV accuracy of 93.6% (p<0.0003) using 6 selected features. Results for MCI vs. NC discrimination while counting backwards with eyes closed are inconclusive, with feature selection failing to suggest likely discriminating features among those tested. While resting with eyes closed, MCI participants as a whole demonstrated higher mean coherence in α activity and greater localization of γ activity in the frontal region. A LOCV accuracy of 87.1% (p<0.0012) is achieved during the REC condition using 6 selected features.

AD vs. NC Results

A LOOCV accuracy of 81.3% (p<0.0042) is achieved for AD vs. NC discrimination during the REO condition. Group differences in selected features indicate greater interdependence of α activity of the frontal region with other regions and higher mean coherence in γ activity for AD participants. LOOCV accuracies of 93.8% (p<0.0003) and 90.6% (p<0.0003) are achieved using 6 selected features for the counting task and REC conditions, respectively. Lower global uniformity of δ activity and lower coherence of β activity in the occipital region is observed for the AD participants during the counting task. When resting with eyes closed, AD participants clearly demonstrate greater localization of δ activity in the left temporal region and significantly higher variability in γ activity.

MCI vs. AD Results

The highest discrimination accuracy for MCI vs. AD is observed during the REO condition, with a LOOCV accuracy of 97.0% (p<0.0003) using 6 selected features. Statistical analyses of the selected features indicate greater uniformity in δ activity and lower uniformity in α and γ activity in AD participants compared to MCI participants. AD participants also demonstrate greater localization of γ activity in the central region. A LOOCV accuracy of 87.9% (p<0.0008) is achieved for the counting backward task using 6 selected features. Those features point to lower uniformity in α and γ activity and greater uniformity in β activity in AD participants compared to MCI participants. Gamma activity features also appear to have greater discriminatory power for the REC closed condition. A LOOCV accuracy of 87.9% (p<0.0007) is also achieved for the REC condition using 6 selected features.

Discussion and Conclusions

In this study, inter-channel coherence graphical network features of scalp EEG recorded during *resting state* conditions and a *simple* cognitive task are explored as a means of effectively and accurately NC, MCI and AD groups. Resting state protocols and simple cognitive tasks (e.g., counting backwards) have several benefits compared to working memory tasks, including more efficient data collection procedures and robustness of analyses regarding patients' state of mind. Interestingly, while the best discrimination between AD and NC participants is achieved during the counting backward condition, the best results in discriminating MCI from NC and AD participants is achieved during the REO

Table 6.3. Group Comparisons and Implications of Selected Inter-Channel Coherence Graphical Network Features

	MCI vs. NC			AD vs. NC			MCI vs. AD		
	Selected Feature	**Group Means**	**Implications**	**Selected Feature**	**Group Means**	**Implications**	**Selected Feature**	**Group Means**	**Implications**
REO	**S** $\bar{H}_C^\alpha$ $\bar{H}_L^\alpha$ $\bar{H}_R^\alpha$ $\bar{H}_F^\beta$ $\bar{H}_O^\beta$ $\bar{K}_C^\beta$	MCI>NC† MCI>NC MCI>NC MCI>NC† MCI<NC† MCI>NC	greater uniformity in α, β activity; greater localization of β activity in O region	**S** D^α $\bar{H}_F^\alpha$ $\bar{H}_O^\alpha$ $\bar{H}_P^\alpha$ $\bar{K}_F^\alpha$ A^γ	AD<NC AD>NC† AD<NC AD>NC AD<NC AD>NC†	greater uniformity in α, γ activity	**S** $\bar{H}_C^\delta$ A^α $\bar{K}_P^\beta$ D^γ $\bar{N}^\gamma$ $\bar{H}_C^\gamma$	MCI<AD† MCI<AD† MCI>AD MCI>AD† MCI>AD MCI>AD†	greater uniformity in δ activity in AD; lower uniformity in α, γ activity in AD; greater localization of γ activity in C region in AD
	acc. (sens., spec.): 93.6% (93.8%, 93.3%) 95% CI for p-value: (0, 0.0003)			acc. (sens., spec.): 81.3% (82.4%, 80.0%) 95% CI for p-value: (0.0020, 0.0042)			acc. (sens., spec.): 97.0% (93.8%, 100%) 95% CI for p-value: (0, 0.0003)		
counting task	no dominant features available		results inconclusive	$\bar{H}_P^\delta$ $\bar{K}_P^\delta$ $\bar{H}_C^\alpha$ $\bar{H}_L^\alpha$ $\bar{K}_O^\beta$ B^γ	AD<NC† AD<NC† AD>NC AD<NC AD<NC† AD>NC	lower uniformity in δ activity; lower coherence of δ activity in P region; lower coherence of β activity in O region	A^α $\bar{K}_R^\alpha$ $\bar{H}_C^\beta$ D^γ $\bar{K}_F^\gamma$ $\bar{K}_P^\gamma$	MCI<AD† MCI<AD MCI<AD† MCI>AD† MCI>AD† MCI>AD†	lower uniformity of α, γ activity in AD; greater uniformity of β activity in AD; greater localization of γ activity in F, P regions in AD
				acc. (sens., spec.): 93.8% (100%, 86.7%) 95% CI for p-value: (0, 0.0003)			acc. (sens., spec.): 87.9% (81.3%, 94.1%) 95% CI for p-value: (0.000008, 0.0008)		
REC	A^α B^α $\bar{K}_O^\beta$ $\bar{K}_P^\beta$ $\bar{K}_F^\gamma$ $\bar{K}_O^\gamma$	MCI<NC† MCI<NC MCI<NC MCI<NC MCI>NC† MCI>NC	greater uniformity in α activity; greater localization of γ activity in F region	$\bar{H}_L^\delta$ $\bar{H}_P^\delta$ $\bar{K}_R^\delta$ $\bar{K}_L^\beta$ B^γ $\bar{N}^\gamma$	AD<NC† AD<NC AD<NC AD<NC AD>NC† AD>NC	greater localization of δ activity in L region; higher variation in coherence of γ activity	C^α $\bar{K}_R^\beta$ D^γ A^γ $\bar{H}_R^\gamma$ $\bar{K}_P^\gamma$	MCI<AD MCI>AD MCI<AD MCI<AD† MCI>AD† MCI>AD	lower uniformity in γ activity in AD
	acc. (sens., spec.): 87.1% (93.8%, 80.0%) 95% CI for p-value: (0.0007, 0.0012)			acc. (sens., spec.): 90.6% (94.1%, 86.7%) 95% CI for p-value: (0, 0.0003)			acc. (sens., spec.): 87.9% (81.3%, 94.1%) 95%CI for p-value: (0, 0.0007)		

† p-value <0.10 for two-sample student t-distribution test (unequal variance) of difference in population means

condition, suggesting that cognitively taxing tasks may indeed be unnecessary for eliciting detectable differences in EEG activity for MCI diagnosis.

Previous studies have observed that EEG features that appear to discriminate AD from normal controls well, do not necessarily perform well when applied to MCI participants [42,63,100]. Often, MCI individuals appear to be spread across boundaries that otherwise clearly discriminate AD from normal participants. These difficulties are likely due to the nature of MCI diagnoses. By definition, neurological symptoms caused by amnestic MCI do not significantly interfere with normal daily activities. In contrast, when patients are diagnosed with AD, their symptoms have generally progressed significantly. Thus, the diagnosis of MCI constitutes a gray area between normal, age-related cognitive decline (NC) and AD. The high accuracy achieved here in discriminating between MCI and AD on the basis of γ activity is encouraging as there is great interest in being able to distinguish between these two related cognitive disorders.

Previous studies have also demonstrated the applicability of synchronization, coherence, and other association measures between scalp EEG electrodes in the discrimination of normal individuals and those with dementia [37]. Typically, researchers have attempted to identify individual local association measures (e.g., coherence between two specific channels at a specific frequency) or a few globally averaged association measures that appear to demonstrate significant robustness in discriminating normal individuals from those with dementia. Unfortunately, dementia can cause different neurological changes in different individuals—especially in the case of more enigmatic diagnoses such as MCI. Such differences may lead to the failure in the generalization of local or globally averaged association measures to other data sets.

This study presents a method for analyzing coherence measures between EEG electrodes via graphical analysis. The success of SVM discrimination between binary groupings of the three groups of EEG records (NC, MCI, and AD) are the result of differences in uniformity of electrical activity in specific frequency bands during resting states and a simple cognitive task. Specifically, MCI participants demonstrate greater uniformity in α and β activity than NC participants when resting with eyes open. AD participants also demonstrate greater uniformity in α and γ activity when resting with eyes open. When counting backwards, differences between MCI and NC participants are inconclusive; however, AD participants demonstrate lower uniformity of δ and β activity in the parietal and occipital regions, respectively, compared to NC participants. When resting with eyes closed, MCI participants demonstrate greater uniformity in α activity and greater localization in γ activity in the frontal region while AD participants demonstrate greater localization of δ activity in the left temporal region and higher variation in γ coherence. Differences between MCI and AD participants are primarily observed with regards to γ activity in all three conditions. It is possible that these differences may be the results of characteristic changes in brain network functional organization (e.g., compensatory mechanisms) as a result of neurological degeneration.

The results of this work suggest the potential for the use of network graphs representing scalp electrical activity relationships as a means for objectively discriminating

between normal, MCI, and AD patients. Results suggest that a simple discrimination model utilizing SVM and the network features presented here may be a viable basis for future development of a diagnostic screening tool for MCI and early AD with applicability in the primary care setting.

CHAPTER 7
CHANNEL RECONSTRUCTION OF BIOMEDICAL SIGNALS USING ARTIFICIAL NEURAL NETWORKS

Signal corruption or loss of data—for example, due to the loss electrode adhesion—is a common issue in biomedical signal acquisition and analysis. Thus, the ability to accurately predict/reconstruct lost signals could greatly impact medical research and application. In this Chapter, methods for reconstruction missing data in multivariate biomedical signals using artificial neural networks are presented. This Chapter begins with a brief introduction to artificial neural networks. Next, a method for reconstructing missing data in ICU machine signals using artificial neural networks is presented. Similar methods to those applied to the reconstruction of ICU signals are then adapted for the reconstruction of normal aged EEG. A method of applying neural network models designed for the reconstruction of normal aged EEG to MCI and AD EEG records as a means of detecting dementia is presented. Finally, results obtained for ICU channel reconstruction and discrimination of MCI and AD EEG records is presented and discussed.

Introduction to Artificial Neural Networks

Artificial neural networks (ANNs) are mathematical models that are designed to function similar to the human nervous system. ANNs consist of interconnected layers of nodes, known as neurons, emulating the functional organization of human nervous tissue. Neurons are the basic processing units of a network and their functionalities are derived from observations of the biological neuron, the basic building block of nervous tissue. Each neuron constitutes a simple mathematical model (function) comprised of three simple steps: (1) multiplication, (2) summation, and (3) activation [78]. In the first step of each artificial neuron's function, the inputs to the neuron are weighted (multiplied by a weighting factor). The weights for the inputs are known as synaptic weights, being based on the responsiveness (weighting) biological neurons attribute to stimulation (inputs) from adjacent neurons. During the second step, the weighted inputs are summed along with a bias. The last step consists of passing the sum of weighted inputs and bias through a specified transfer function. The transfer function defines the properties of an artificial neuron and can be any mathematical function. The most common transfer functions are the step function, a linear function (`purelin`), and nonlinear sigmoid function (`tansig`) [78]. This process is presented in mathematical form in Equation (7.1):

$$y = F\left(\sum_{i=1}^{N} w_i x_i + b\right), \quad (7.1)$$

where y is the output from the neuron, F is the transfer function, x_i are the inputs to the neuron, w_i are the input weights, and b is the bias of the neuron [78].

Although the working principles of an individual artificial neuron may seem trivial, the potential computational power of artificial neurons cannot truly be appreciated until multiple neurons are interconnected in order to construct an ANN; see Fig. 7.1 for a schematic of a simple artificial neural network. In order to take full advantage of the benefits of the mathematical complexity inherent in ANNs, artificial neurons are generally not connected randomly. Previous researchers have developed several standardized topographies, which can be divided into two major categories: feed-forward neural networks, where information is transferred from inputs to outputs in only one direction, and neural networks with recurrent topologies, where some of the information flows from input to outputs as well as from outputs to inputs. Here, discussion is limited to feed-forward ANNs; for more information regarding recurrent topographies, see work by Gurney [53].

Feed-forward ANNs (ffANNs) are designed on the premise that information must flow from input to output in only one direction. There are no limitations to the number of layers, type of transfer function used in individual neurons, or the number of connections between individual neurons. When multiple layers of neurons are used, a simple ffANN can lead to highly nonlinear functions between inputs and outputs.

Before an ANN can be applied to a specific problem, it must be trained. ANNs may be trained in a supervised or unsupervised fashion. The method of training is typically chosen on the same basis as the topography in order to best fit a given application [78]. Supervised learning is a machine learning technique that sets parameters of an ANN based on example training data. The training data consist of pairs of input and desired output values. Various optimization techniques exist for adjusting weights and biases of ANNs in order to accurately map inputs to outputs. Unsupervised learning is a machine learning technique that adjusts the weights and biases of ANNs based on given data and a cost function, which is to be minimized [78]. The cost function is generally based on the formulation of the task for which the ANN is being trained. Generally, unsupervised learning is used to train ANNs for applications of estimation, such as statistical modeling, compression, filtering, and clustering. The primary difference in unsupervised learning is that the provided training data is unlabeled. A common form of unsupervised learning is clustering, where data is categorized into different clusters based on similarities. The most commonly used unsupervised learning algorithm is self-organizing maps [78].

Neural networks can be trained to perform a wide variety of tasks. Previous research has demonstrated their capabilities in application modeling, prediction, classification, control, function approximation, data preprocessing, filtering, clustering, compression, robotics, regulations, and decision making, to name a few [78*,89].
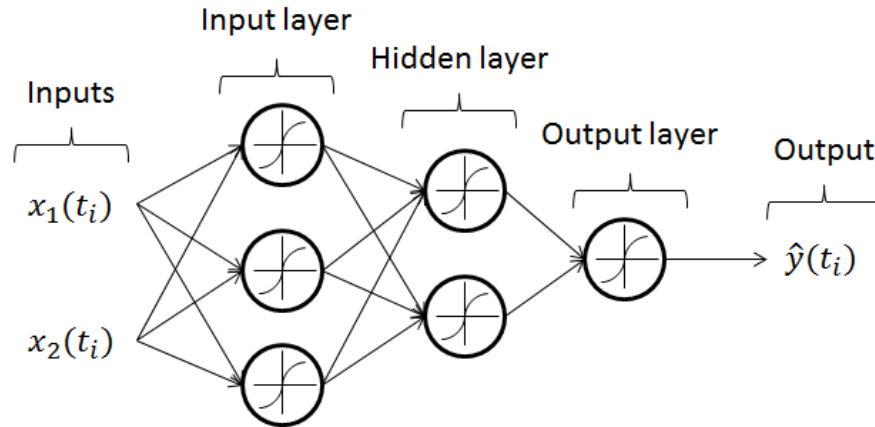
Fig. 7.1. Schematic of Simple Feed-Forward Artificial Neural Network (ffANN). Neurons' nonlinear transform functions are indicated by the plot of the sigmoid function within each neuron. Note that output $\hat{y}$ has a hat above it, indicating that it is an approximation of the true output y based on training.

Reconstruction of ICU Signals Using Artificial Neural Networks

PhysioNet 2010 Challenge

In the Computing in Cardiology/PhysioNet 2010 Challenge: Mind the Gap (http://physionet.org/challenge/2010), participants were asked to reconstruct segments of signals that had been artificially removed from multi-parameter recordings of patients in ICUs, using any combination of available prior and concurrent information. Data for the Challenge were selected from ICU patient monitor recordings collected by the MIMIC II project [49,115]. Each record was 10 min long and contained 6 to 8 simultaneous and continuous signals, which were discretized at 125 Hz. Thus, each record contained 75,000 observations for each signal. Different records contained different signals. The possible signals included ECG, arterial blood pressure (ABP), central venous pressure (CVP), respiration (RESP), raw fingertip plethysmogram outputs (PLETH), and occasionally other signals. In each 10-minute record, the final 30 s (3750 observations) of a randomly chosen signal were replaced by a flat line signal. Fig. 7.2 shows an example of the last minute of a record. The goal of the Challenge was to reconstruct this missing 30-s target signal in each record.

The Challenge provided 300 records, which were randomly assigned to 1 of 3 datasets such that each dataset contained 100 records. Set A was used for training. The target signals were provided for records in this set. Participants in the Challenge were able to obtain quality scores for reconstructions of records in this set at any time, which allowed participants to tune their algorithms. The scores for set A were not included in the final rankings of Challenge entries. Target signals for set B were withheld from participants;
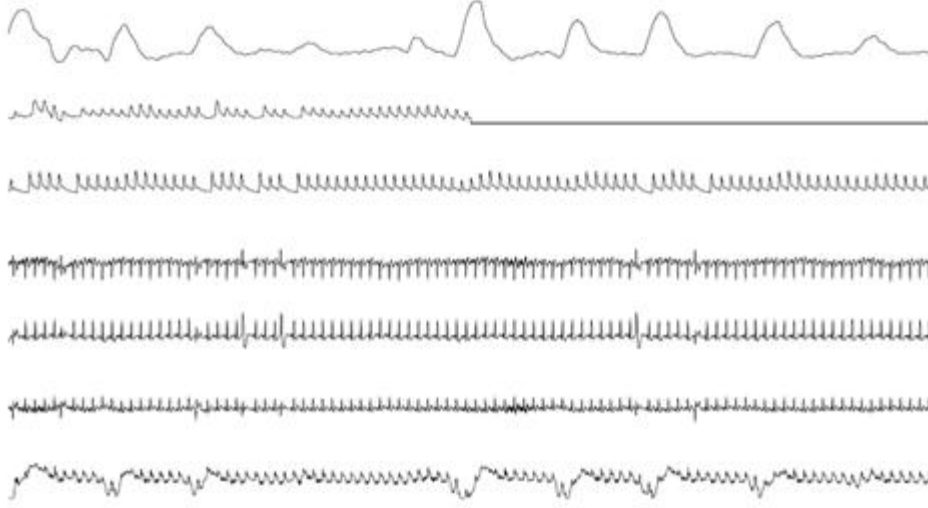
Fig. 7.2. Last Minute of a Typical Record in PhysioNet2010 Challenge; Figure Copied from [93]. From top to bottom, the signals are RESP, PLETH, BP, ECG lead II, ECG lead "V" (an unspecified precordial lead), ECG lead VR, and CVP. Note that PLETH is the target signal, the final 30 s of which is replaced by a flat line.

however, participants were able to obtain scores for set B reconstructions at any time using the PhysioNet website. Like set A, set B scores were not included in the final rankings of Challenge entries. Target signals in set C were withheld from the participants. Set C scores were used to determine the final rankings and the winners of the Challenge [93].

Two quality scores were used in the Challenge to evaluate the accuracy of reconstructions. The first quality score Q_1 is defined by Equation (7.2):

$$Q_1 = max\left[1 - \frac{MSE}{\sigma^2}, 0\right], \quad (7.2)$$

where σ represents the standard deviation of the actual data $y(t)$ and MSE represents the mean squared error (i.e., the average of the squared difference between the reconstructed signal $\hat{y}(t)$ and the actual data $y(t)$). Thus, Q_1 is the larger value between the R-squared value and zero. The second quality score Q_2 is defined by Equation (7.3):

$$Q_2 = max\left[\frac{Cov[y(t), \hat{y}(t)]}{\sigma\hat{\sigma}}, 0\right], \quad (7.3)$$

where $\hat{\sigma}$ represents the standard deviation of the reconstructed signal $\hat{y}(t)$ and $Cov[y(t), \hat{y}(t)]$ represents the covariance between the actual data $y(t)$ and the reconstructed signal $\hat{y}(t)$. In other words, Q_2 is the larger value between the correlation coefficient and zero.

106

The method presented in this study achieves outstanding scores for all three datasets [89]. Since target signals were only available for set A, data in set A is used to illustrate the efficacy of the methodology presented here.

Methodology

Formulation of Reconstruction Problem for ffANN

The methodology presented here is based on application of ffANNs. The channel containing the target signals (missing information) are treated as the output and the remaining channels of a record are treated as input channels. Thus the output channel can be represented by a scalar time series $\{y_n\}$ and the input channels by a vector time series $\{x_n\}$, where the vector x_n contains signals from all input channels at observation n. The goal is thus to find a mapping function that relates a target signal to input signals as presented in Equation (7.4):

$$y_n = F\left(x_{n-d_1}, x_{n-d_2}, \ldots, x_{n-d_M}\right), \qquad (7.4)$$

where F is the mapping function and $d_i \geq 0, i = 1, \ldots, M$ represent delays in the input channels. For later convenience, a delay vector is introduced as follows: $d = \{d_1, d_2, \ldots, d_M\}^T$. For example, a delay vector $d = \{0,1,2\}^T$ corresponds to the input consisting of the observations x_n, x_{n-1}, and x_{n-2}. The notation $d = start : step : end$ is here introduced to represent a vector whose elements increase at an increment from $start$ to end in steps of length $step$. Note that the delay vector is unitless and represents sample indices. Recall that the sampling frequency was 125 Hz. Thus, the delay vector $d = 0 : 1 : 10$ means data up to 0.08-s old is used. To convert Equation (7.4) into a feed-forward form, an augmented vector z is introduced in Equation (7.5):

$$z_n^T = \left\{x_{n-d_1}^T, x_{n-d_2}^T, \ldots, x_{n-d_M}^T\right\} \qquad (7.5)$$

Using the augmented vector, it follows that Equation (7.4) can be rewritten as a function between y_n and z_n with a new mapping function G:

$$y_n = G(z_n) \qquad (7.6)$$

The relationship presented in Equation (7.6) is the framework of a ffANN.

Structure and Design of ffANN

Simulations in this study are carried out using the neural network toolbox in MATLAB™ [88]. The computer programs are executed on a high performance computing cluster located at the University of Tennessee [96]. Default parameters listed in Table 7.1 are used in all simulations unless otherwise stated. A ffANN with two hidden layers is used (input layer and output layer). A hyperbolic tangent sigmoid transfer function (`tansig`) is used in neurons in the first layer (input layer), and a linear transfer function (`purelin`) for neurons in the second hidden layer (output layer). The first layer has 10 neurons and the second layer has 1 neuron. The 5 min of data immediately prior to the missing signal

Table 7.1. Default Parameters Used in Neural Network Simulations
For PhysioNet 2010 Challenge

Number of hidden layers	2
Number of neurons	10 for the 1st hidden layer and 1 for the 2nd hidden layer
Transfer functions	Tansig for 1st hidden layer and purelin for 2nd hidden layer
Training data	5 minutes of data immediately prior to the missing signals
Training epochs	40
Performance function	Mean squared normalized error (MSNE)
Delay vector d	0:10:100 (numbers from 0 to 100 in steps of 10)

are used to train the network for 40 epochs. The mean squared normalized error (MSNE) is used as the performance function of the network model. A default delay vector of $d = 0:10:100$ is used. All other parameters adopt their default values in MATLAB.

Iterative Retraining and Accumulated Averaging

Based on ffANNs, an iterative retaining technique and an accumulated averaging technique are developed in order to improve the accuracy of reconstructions. Recall that each record was 10 min long and sampled at 125 Hz. Thus, each record consisted of 75,000 observations for every signal. First, a 10-minute record is divided into 20 segments, each 30 s long (3750 observations). Input data in each segments are denoted by X_1, X_2,..., X_{20}. Note that the notation X_n represents a vector time series. Likewise, the corresponding output channel data in each segment are denoted by Y_1, Y_2,..., Y_{20}. Note that the notation Y_n represents a scalar time series. Thus, time series Y_{20} was the target signal to be predicted. The iterative retraining process is carried out for a given record via the following steps:

(1) An ffANN is trained using a training set, where the input data consist of X_{10}, X_{11},..., X_{19} and the corresponding output data consist of Y_{10}, Y_{11},..., Y_{19}.

(2) The ffANN trained in step (1) is applied to the input data X_{20} to predict the target signal Y_{20}. For later convenience, the predict signal is denoted by Z.

(3) A new ffANN is trained using a training set, where the input data consisted for X_{11}, X_{12},..., X_{20} and the corresponding output data consisted of Y_{11},..., Y_{19}, Z.

(4) The ffANN trained in step (3) is applied to the input data X_{20} to generate new predictions. Z is then updated using the new predicted target signal computed in this step.

(5) Steps (3) and (4) are repeated until the desired number of iterations is reached.

To illustrate the method of accumulated averaging, suppose the N iterations of retraining have been conducted and denote the predictions from each of these iterations by $Z^{(1)}$, $Z^{(2)}$,..., $Z^{(N)}$. This sequence of predictions is averaged accumulatively to generate a new sequence: $A^{(1)}$, $A^{(2)}$,..., $A^{(N)}$. Here, $A^{(N)}$ is the average of the first N iterations: $Z^{(1)}$, $Z^{(2)}$,..., $Z^{(N)}$.

Results for ICU Machine Signal Reconstruction

Results for Various Techniques
The techniques described in the previous section are applied to PhysioNet records in set A. Aggregate Q_1 and Q_2 scores for all 100 records in set A obtained using the default parameters listed in Table 7.1 are presented in Fig. 7.3. In Fig. 7.3, results marked with triangles (blue) are obtained using straightforward simulation of ffANNs. Note that computations are repeated for 25 trials. In most trials, the aggregate Q_1 scores are within the range 73 to 75 whereas the aggregate Q_2 scores are in the range of 85.5 to 86.5. Results marked with stars (black) are obtained using the iterative retraining mechanism. The retraining algorithm is applied for 25 iterations. Note that the retraining algorithm starts from the first iteration that is obtained from a straightforward prediction using the ffANN. In subsequent iterations, predictions from the previous iteration are used to retrain a new network, which is then used to produce prediction for the current iteration. As seen in Fig. 7.3, the results from retraining are consistently more accurate than those from straightforward simulations. Nevertheless, both aggregate Q_1 and Q_2 scores of retraining results demonstrate fluctuations from iteration to iteration. On average, the retraining mechanism improves the aggregate Q_1 score by about 3 points and the aggregate Q_2 score by about 1.5 points. It is interesting to note that the retraining results are further improved using accumulated averaging; see circles (red) in Fig. 7.3. Here the average of predictions of the first n iterations is computed. Thus, the average accumulates when n increases. Moreover, aggregate Q_1 and Q_2 scores of the accumulated averaging mechanism smoothly converge as the number of iterations is increased. The converged Q_1 score is improved by about 2.5 points and the converged Q_2 score is improved by about 1.5 points compared to results of iterative retraining. Extensive simulations are conducted using various parameters and it is consistently observed that iterative retraining and accumulated averaging significantly improve the accuracy of the predictions. Trends are similar to those shown in Fig. 7.3.

Results for Different Types of Target Signals
The results from straightforward simulations, iterative retraining, and accumulated averaging are further compared by examining their scores for different types of targets; see Table 7.2. The 100 records in set A included 5 different types of target signals: blood pressure (BP), CVP, ECG, PLETH, and RESP. Note that the BP targets included nine ABP targets and one pulmonary arterial pressure target. First, the scores for each record are averaged using 25 trials (for straightforward ffANN simulations) or 25 iterations (for iterative retraining). The scores for accumulated averaging are computed using the reconstructions from the accumulated averaging of the first 25 iterative retraining predictions as described in previously. The mean and standard deviations for scores of
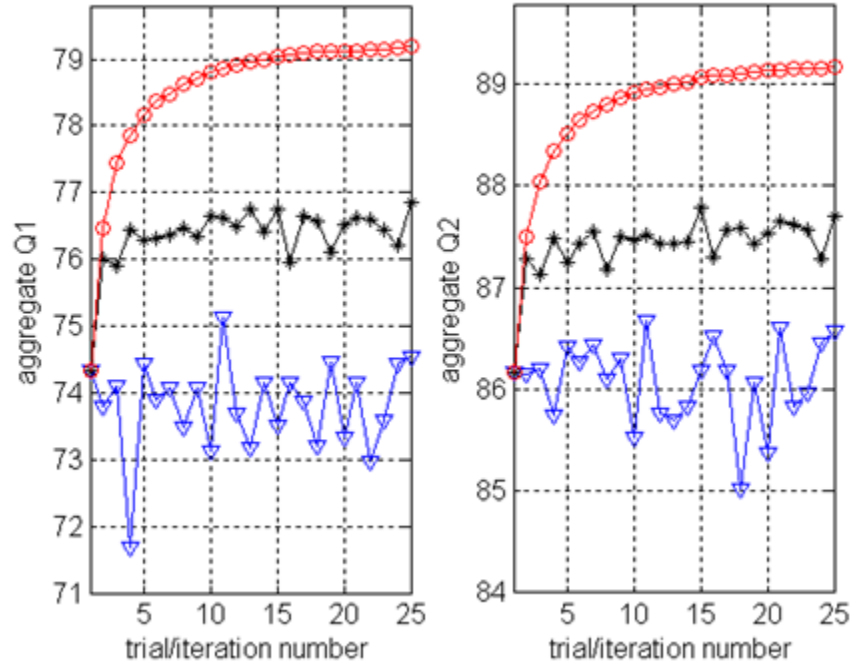
Fig. 7.3. Aggregate Scores for Records in Set A [89]. Straightforward simulations (triangles), iterative retraining mechanism (stars), and accumulated averaging (circles).

Table 7.2. Results for Set A Records for Different Target Signals

Target types	Straightforward simulation		Iterative retraining		Accumulated averaging		No. Rec.
	Q1	Q2	Q1	Q2	Q1	Q2	
BP	0.888 ± 0.104	0.957 ± 0.046	0.906 ± 0.090	0.963 ± 0.039	0.924 ± 0.082	0.972 ± 0.037	10
CVP	0.638 ± 0.340	0.830 ± 0.177	0.684 ± 0.304	0.848 ± 0.164	0.729 ± 0.266	0.870 ± 0.145	10
ECG	0.910 ± 0.187	0.945 ± 0.146	0.925 ± 0.157	0.954 ± 0.135	0.934 ± 0.154	0.958 ± 0.133	44
PLETH	0.608 ± 0.283	0.758 ± 0.249	0.637 ± 0.282	0.775 ± 0.242	0.666 ± 0.281	0.794 ± 0.237	15
RESP	0.446 ± 0.313	0.727 ± 0.153	0.485 ± 0.306	0.748 ± 0.147	0.551 ± 0.304	0.794 ± 0.138	21
All	0.738 ± 0.312	0.861 ± 0.191	0.763 ± 0.292	0.874 ± 0.181	0.792 ± 0.274	0.892 ± 0.169	100

Averages ± standard deviations of scores using different techniques.

different types of target signals are then calculated.

For all types of target signals, accumulated averaging produces the best scores and straightforward simulations produce the worst scores. The differences among scores for different methods are most dramatic in CVP, PLETH, and RESP signals. For example, relative to the results of straightforward simulations, the accumulated average technique improves the scores of CVP by 14.3% in Q_1 and 4.8% in Q_2; the cores of PLETH are improved by 9.5% in Q_1 and 4.8% in Q_2; and the scores of RESP are improved by 23.5% in Q_1 and 9.2% in Q_2. On the other hand, the improvements of scores by retraining and averaging are minimal in ECG and BP signals. Overall, when comparing between straightforward simulations and accumulated averaging, aggregate scores are improved by 5.4% in Q_1 and 3.6% in Q_2. Moreover, retraining and averaging also had reduced magnitudes of standard deviations for all signals. The results of accumulated averaging are extremely accurate for BP and ECG target signals. The reconstructions of RESP signals are the worst, with average scores being Q_1 = 0.564 and Q_2 = 0.778. This was likely due to the fact that the frequency of RESP is much lower than those of other signals. Thus, the high frequency variations in signals such as ECG appear as spikes in the reconstructed signals.
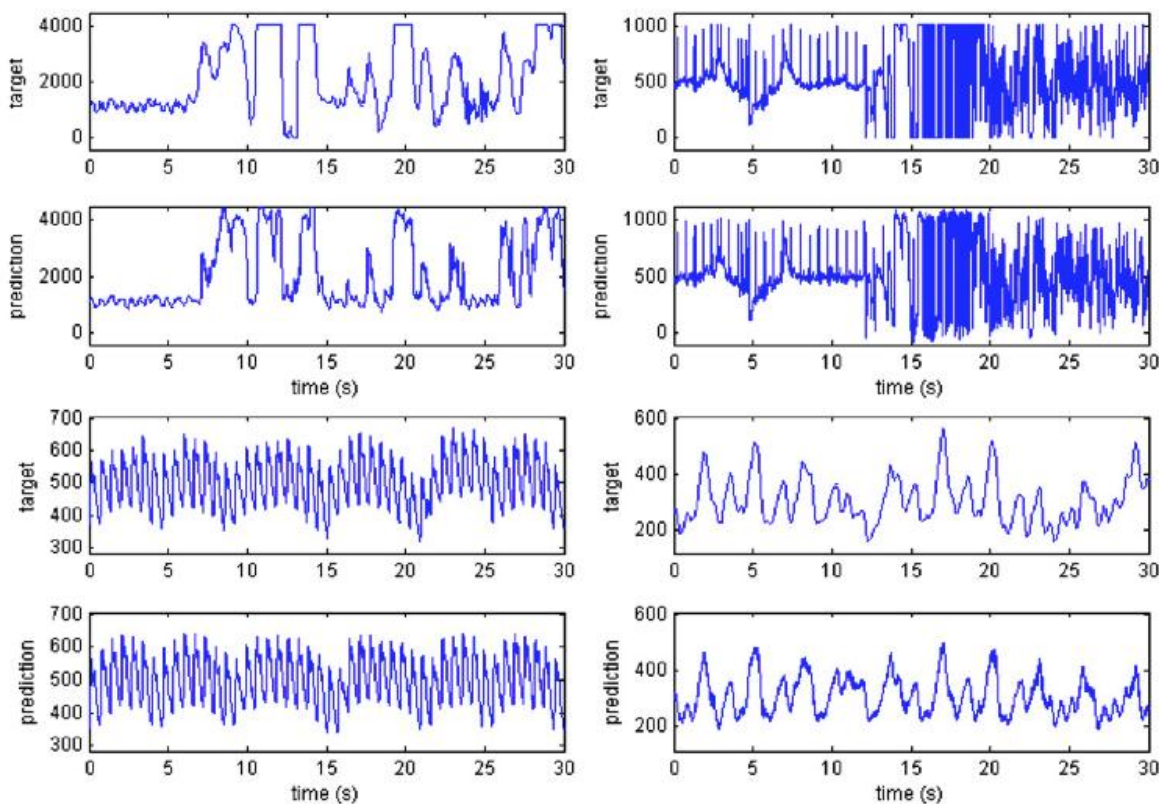

Fig. 7.4. Selected Examples of Target Signals and Reconstructions [89]. CVP (top-left, Q_1 =0.8095 and Q_2 = 0.9042); ECG (top-right, Q_1 =0.9512 and Q_2 = 0.9756); PLETH (bottom-left, Q_1 =0.8688 and Q_2 = 0.9344); and RESP (bottom-right, Q_1 =0.7085 and Q_2 = 0.8444).

Figure 7.4 shows the time histories of the actual targets and the predicted targets of a few selected records. All reconstructions in Fig. 7.4 are obtained from accumulated averaging. The top-left panel shows a CVP target. Here, the recordings in the actual target are flattened out by the upper limit of the machine used to record the signal. Although the network model is not able to recover the flat saturation in the signal, it faithfully captures the overall trend, producing scores of Q_1 =0.8095 and Q_2 = 0.9042. The top-right panel shows the time history of an ECG target, which showed a transition from normal rhythms to abnormal rhythms. The second half of the record clearly shows saturation in reading and chaotic patterns of arrhythmias. The model produces a strikingly accurate reconstruction with Q_1 =0.9512 and Q_2 = 0.9756. The bottom-left panel shows a PLETH signal, which exhibited a quasiperiodic behavior, where a high frequency oscillation is modulated by a low frequency envelope. An accurate reconstruction is obtained with Q_1 =0.8688 and Q_2 = 0.9344. The bottom-right panel shows a RESP signal. The dominant frequency of the RESP signal (reflecting the breathing rate) is lower than the frequency of the other signals in the record (e.g., ECG signals). Therefore, while the true RESP signal was a smooth curve, the predicted RESP signal exhibits artificial fluctuations induced by fast rhythms in other signals used to construct the prediction. It is noted, however, that increasing the length of the delay vector to cover an entire cycle of the RESP signal improves the accuracy of the prediction; see Fig. 7.6. Although the target signal shows very irregular patterns the reconstruction achieved good accuracy with Q_1 =0.7085 and Q_2 = 0.8444. It is interesting to note that the ffANN models are capable of accurately reconstructing physiological records even when the signals were highly random and irregular.

Influence of Various Parameters

Influence of the Delay Vector

The delay vector proves to be an important parameter in signal reconstructions. A good choice of delay vector has the potential to significantly improve the accuracy of predictions. The default delay vector is selected because it is a mix of short-term memory—data points immediately prior to the target—and long-term memory—data points that are relatively far from the target. To illustrate the influence of the delay vector, simulations are conducted using a different delay vector $d = 0: 1: 10$. This delay vector is termed the short-term memory delay vector because all delays are close to the target and they only represent what occurred in the near past. Aggregate scores using the short-term memory delay vector are presented in Table 7.3, where statistical analyses for different target types are presented. Here, scores for straightforward simulations are the average of the scores for 25 trials. The scores for iterative retraining are the average scores from the first 25 iterations. The scores for accumulated averaging are the scores computed using the reconstructions from the accumulated averaging of the first 25 iterations. Comparing Tables 7.2 and 7.3 shows that the mixed memory (default delay) performs better than the short-term memory delay in almost all types of target signals, with the exception of ECG. In particular, reconstructions of PLETH and RESP targets are significantly improved using the mixed memory delay vector. Moreover, the improvement of scores is consistent for all three different techniques (straightforward simulations, iterative retraining, and accumulated averaging).

Table 7.3. Results for Set A Records Using Short-Term Memory Delay

Target types	Straightforward simulation		Iterative retraining		Accumulated averaging		No. Rec.
	Q1	Q2	Q1	Q2	Q1	Q2	
BP	0.851 ± 0.118	0.941 ± 0.048	0.863 ± 0.111	0.946 ± 0.047	0.884 ± 0.100	0.956 ± 0.042	10
CVP	0.633 ± 0.349	0.820 ± 0.183	0.652 ± 0.335	0.833 ± 0.171	0.698 ± 0.295	0.860 ± 0.152	10
ECG	0.931 ± 0.157	0.959 ± 0.121	0.938 ± 0.153	0.963 ± 0.115	0.943 ± 0.151	0.966 ± 0.113	44
PLETH	0.546 ± 0.294	0.721 ± 0.265	0.556 ± 0.289	0.723 ± 0.269	0.582 ± 0.289	0.738 ± 0.273	15
RESP	0.327 ± 0.271	0.612 ± 0.197	0.348 ± 0.261	0.628 ± 0.196	0.411 ± 0.248	0.676 ± 0.184	21
All	0.709 ± 0.334	0.835 ± 0.222	0.721 ± 0.326	0.842 ± 0.218	0.747 ± 0.303	0.860 ± 0.204	100

Averages ± standard deviations of scores using different techniques.

In addition, comparisons are made of results obtained using six different delay vectors: 0:10:100, 0:10:200, 0:10:300, 0:10:400, 0:10:500, and 0:10:600. Figure 7.5 shows the aggregate scores of various target signal types under the variation of delay vector. It can be seen that the best scores are obtained at different delays for different types of target signals. Overall, a short delay vector is preferred for BP, CVP, and ECG targets whereas a long delay vector improves prediction accuracies for PLETH and RESP targets. Thus, a delay vector chosen according to the type of the target signal is capable of leading to better results.

Influence of the Number of Neurons

The influence of the number of neurons on the accuracy of predictions is also studied. In order to reduce computational time, the length of training data is reduced to 2 min, the number of epochs to 20, and number of iterations to 10. The number of neurons in the second hidden layer is kept fixed while the number of neurons in the first hidden layer (the input layer) is varied. All other parameters are the same as the default parameters. Figure 7.6 shows the influence of the number of neurons. When the number of neurons is decreased, the aggregate scores do not change significantly until the number of neurons is fewer than five. It is interesting to note that with only one neuron in the first hidden layer, the ffANN is still able to produce reasonably good results with aggregate $Q_1 > 70$ and aggregate $Q_2 > 82$. Indeed, these scores are comparable to those obtained by other participants in the PhysioNet Challenge who employed Kalman filters and adaptive filters [93]. The advantage of fewer neurons is increased computational efficiency. The right panel in Fig. 7.6 shows that the average computational time (for 10 iterations) for a record

113

increases linearly as the number of neurons increases. When the number of neurons is decreased from 10 to 1, the computational time is decreased by several folds. Specifically, it takes less than 40 s to finish 10 iterations when 1 neuron is used. This observation is of great significance for real-time application of data reconstruction.
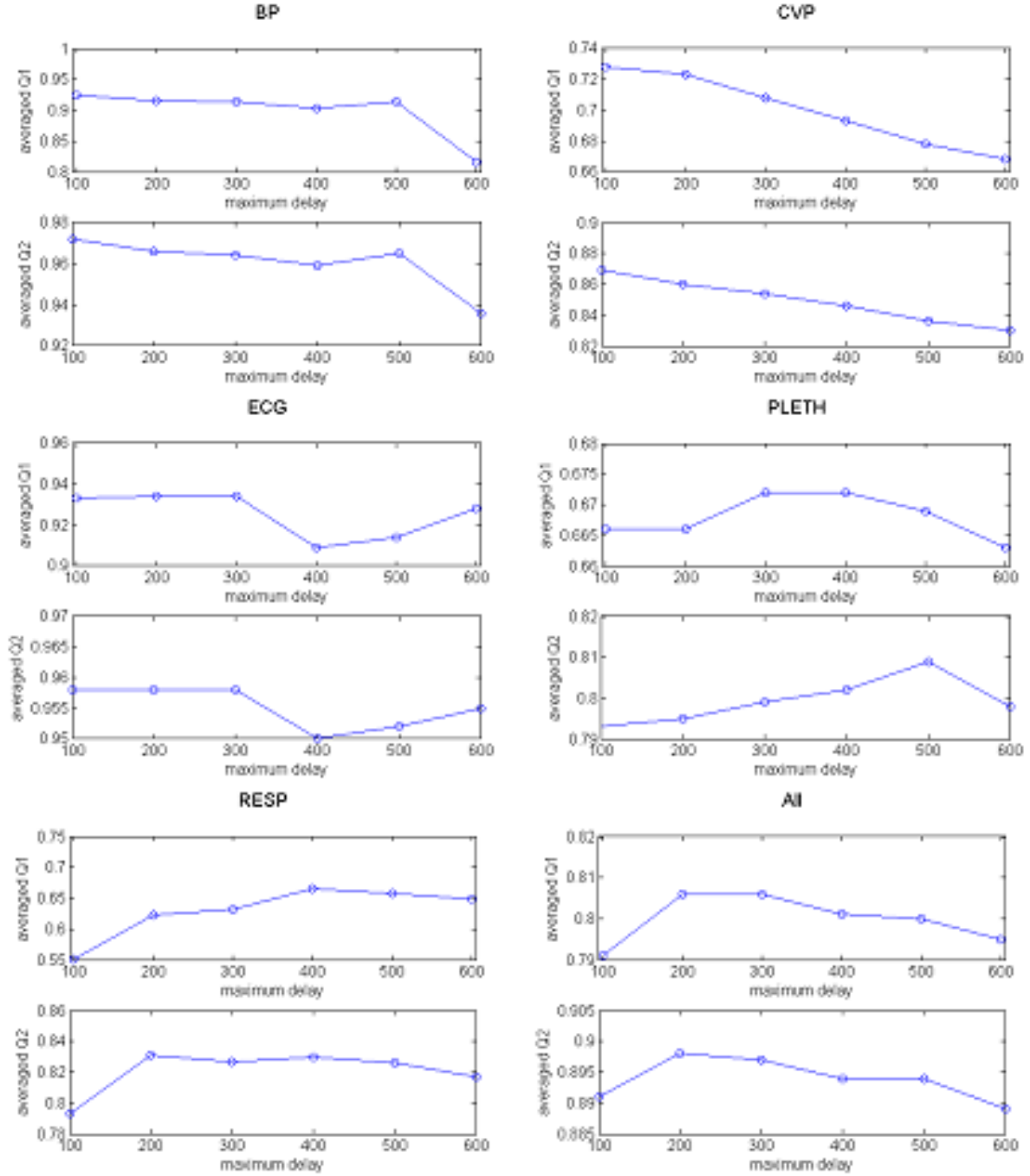
Fig. 7.5. Comparison Between Six Different Delay Vectors [89]. Delay vectors include 0:10:100, 0:10:200, 0:10:300, 0:10:400, 0:10:500, and 0:10:600. All other parameters are identical.
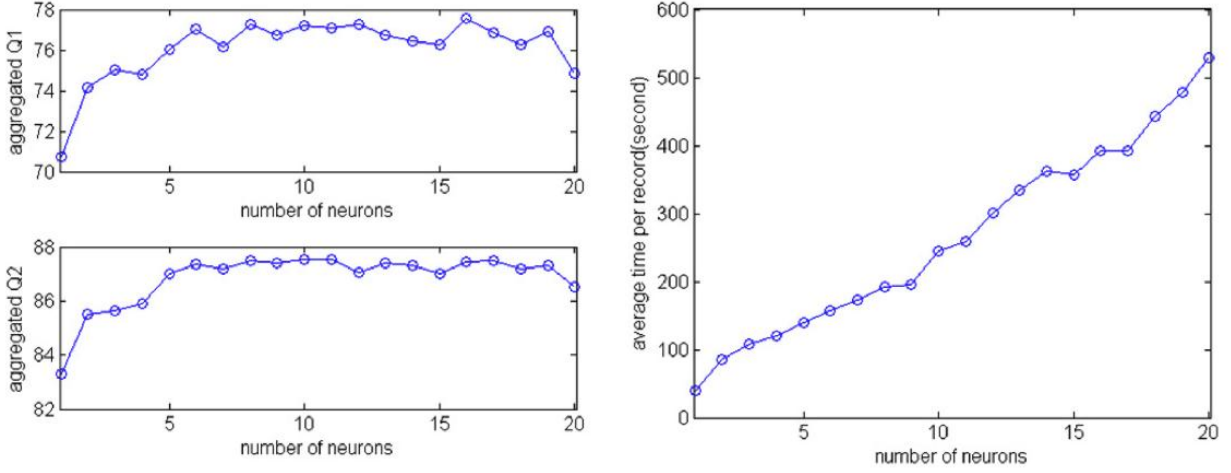
Fig. 7.6. Influence of the Number of Neurons [89]. Number of neurons in the first hidden layer (input layer) was varied. Left panel: variation of aggregate Q_1 and Q_2; right panel: variation of the average computational time for each record (10 iterations).
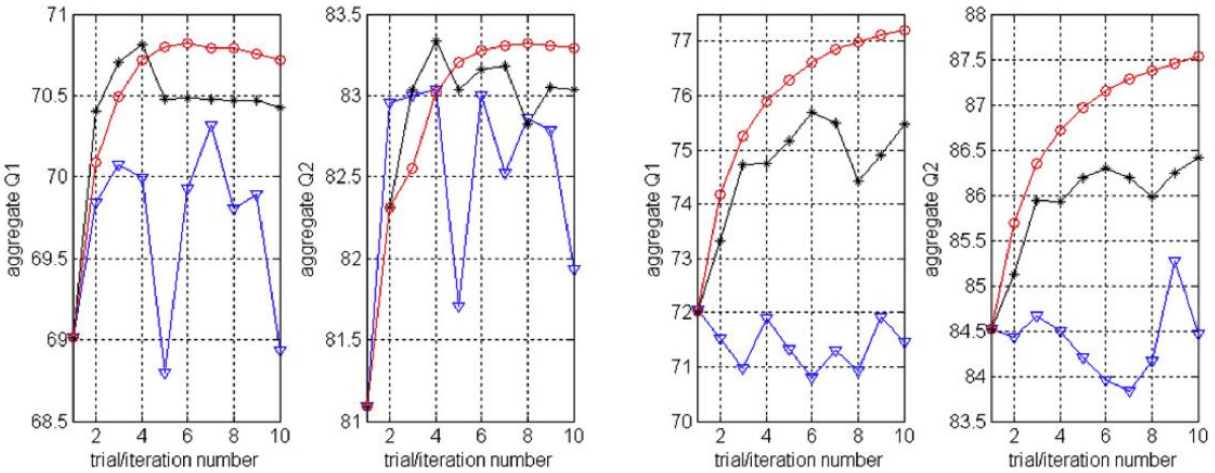
Fig. 7.7. Comparison Between Aggregate Scores Using 1 and 10 Neurons in Input Layer [89]. Left panel: 1 neuron in first hidden layer; right panel: 10 neurons in first hidden layer. Straightforward simulations (triangles); iterative retraining (stars); accumulated averaging (circles). Results obtained using 2 min of training data and 10 training epochs.

Figure 7.7 shows a comparison between results obtained using 1 neuron and 10 neurons in the first hidden layer, respectively left to right. It is interesting to note that even with just one neuron in the first hidden layer, the iterative retraining and the accumulated averaging techniques are still capable of improving the accuracy of reconstructions, though to a minor degree. As seen in Fig. 7.7, the effect of iterative retraining and accumulated averaging depends on the underlying model. Nevertheless, the accumulated averaging of

115

retraining shows consistent convergence, indicating that the technique is robust against different models and parameters.

Influence of Nonstationary Properties of Physiological Data

Physiological data are often nonstationary signals with time-varying characteristics [41,105]. The nonstationarity properties of the data in set A are examined by analyzing the dependence of the accuracy of reconstructions on the relative time lapse between training data and target signals. Specifically, the 10 min records are divided into 20 segments of 30 s each. Network models are then trained using data of the first 5 min and applied to predict 30 s segments of target signals in the next 10 segments. The target channels are the same as those chosen by the PhysioNet Challenge. The Q_1 and Q_2 scores are computed for each 30 s target segment. This process is repeated 50 times. Box plots of aggregate Q_1 and Q_2 scores are shown for each target segment in Fig. 7.8. As can be seen in Fig. 7.8, segments that immediately followed the training data are predicted with much greater accuracy than those that were farther away. Thus, data close to the target of reconstruction are better for training than data from the more distant past. The implication of this observation in practice is that a new model would need to be constructed for each time period with missing signals since the model essential becomes "out of date" after a certain time.
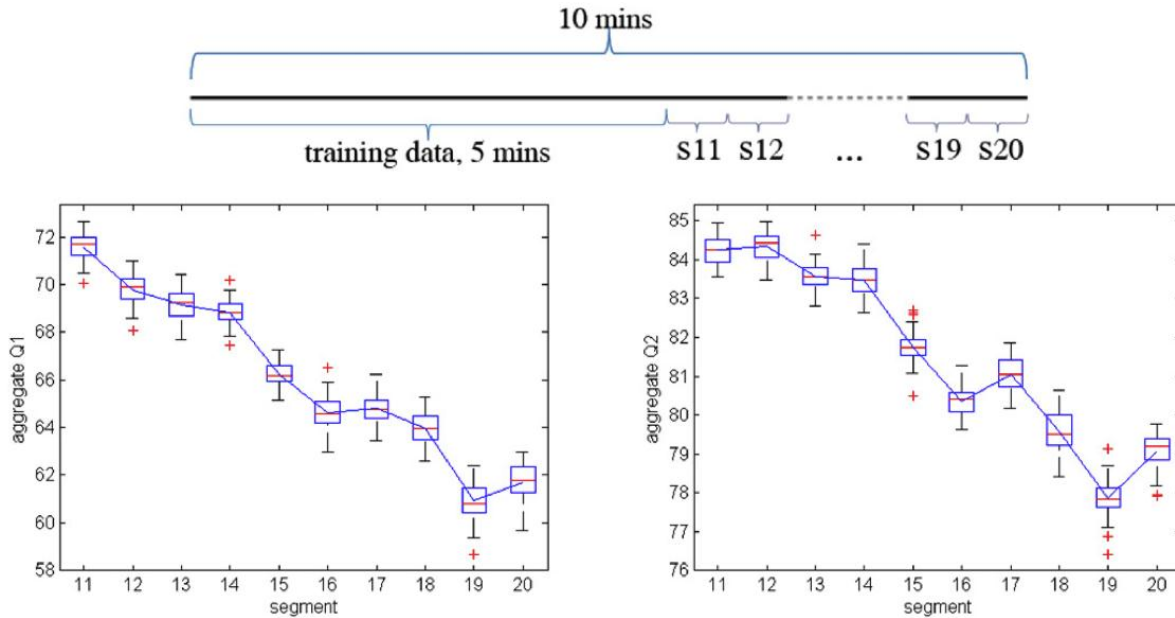
Fig. 7.8. Dependence of Accuracy of Prediction on Nonstationarity Properties of Data [89]. Top: organization of data, where S1, S2,…, S20 denote 30 s segments of last 5 min of data. Bottom: aggregate scores for segments based on 50 repetitions. Boxplots show the 25th percentile, median, and 75th percentile of scores; whiskers indicate lower and upper extremes; crosses indicate outliers (those greater than 1.5 times the standard deviation from the median). Curves connect means of scores.

Detection of Dementia Using EEG Signal Reconstruction
via Artificial Neural Networks

Motivation and Synopsis

This study investigates a new method for detecting the differences in EEG associated with changes in neurological functional organization due to MCI and early AD by applying the concept of Sugihara causality to EEG. In contrast to Granger causality, Sugihara causality is based on theory of nonlinear state space reconstruction to study the causation that characterizes deterministic dynamics of the system. Sugihara causality indicates that nearby points on the manifold of one variable can be used to estimate nearby points on the manifold of another variable [137]. Here, Sugihara causality analysis is employed to estimate the time series in one EEG channel using the other channels of the same EEG record.

The results of the study of the PhysioNet 2010 Challenge data presented in the previous section demonstrate that in the case of multi-channel physiological signal recordings, there exists an inherent relationship between channels that can be modeled using ANNs [89]. This relationship is a real-world example of the theory of Sugihara causality [54].

Motivated by the successful application of neural network models for the reconstruction of missing ICU machine data, in this study ANN models are developed for the reconstruction of artificially deleted information from EEG recordings of normal aged, MCI, and AD individuals. This study explores scalp-EEG based biomarkers for MCI and early AD. Results of this work are based on data from the NER Dataset. As described in Chapter 1, the NER Dataset consisted of three separate protocol conditions: the REO condition, the counting task, and the REC condition. Each record contained 30 electrodes (32 channels with 2 ocular channels excluded).

First, a reconstruction model is developed for each channel of the EEG record, predicting the signal in the current channel using concurrent data of the other 29 channels. A reconstruction model can be trained using records in the NC, MCI, and AD groups, respectively, which produce corresponding NC, MCI, and AD models.

Next NC, MCI, and AD models ware then applied to an EEG record and quality scores are computed to measure the closeness between the predicted signal and the original signal in a given channel. To avoid information leak, the reconstruction models are trained based on the leave-one-out principle.

Finally, the quality scores are studied for their potential as biomarkers to distinguish between the different cognitive groups. The dimension of the quality scores is reduced to two principal components. A three-way classification scheme using the principal components demonstrates accuracies of 95.8%, 95.8%, and 97,9% for the REO condition, counting task, and REC conditions, respectively. The quality scores based on Sugihara causality analysis captures characteristic changes in EEG activity due to cognitive

deficits and demonstrates potential in the detection of pathophysiological changes in early AD.

Methodology

Networks for EEG Reconstruction

Neural network models are developed for the reconstruction of artificially "deleted" information from EEG records for each of the three groups of participants (i.e., NC, MCI, and AD). The procedure for training models for a given group is detailed for the NC-based model as follows. Thirty neural networks are constructed, one for each of the 30 EEG channels used in analyses. Each network consists of a single hidden layer of five neurons, each with a `tansig` transfer function, and a single output node with a `purelin` transfer function; see Table 7.4 for a list of all default parameters. A schematic of the network structure is presented in Fig 7.9. For each network, *concurrent* data from the remaining 29 channels is used to generate a reconstruction for the given channel. The 30 neural networks thus constitute a collection of networks, or model, designed to reconstruct missing data from any of the 30 channels. A different model is developed for each protocol condition. All neural network simulations in this work are carried out using the neural network toolbox in MATLAB™ [88].

Each model is trained using 2-min samples from NC records taken during the given protocol condition. In order to avoid the potential for intra-participant bias, (information leak) a different collection of neural networks is trained for each NC participant using data from all other NC participants via the leave-one-out principle. A pseudo code for this leave-one-out approach is presented below. In addition, a separate collection of networks is trained using 2-min samples for *all* available NC participants during the given protocol condition. This set of networks is then applied to MCI and AD, for which intra-participant bias is not a concern. An analogous procedure was used to develop models based on MCI and AD participants.

```
% pseudo code for NC-based models applied to NC participants
for i in 1,2, ...,30 % there are 30 channels
    for j in 1,2, ..., 15 % there are 15 NC subjects
        assemble training set using data of NC subjects except j
        % reconstruct channel i from other channels
        train the reconstruction model using training set
        apply the model to channel i of participant j
        evaluate quality of reconstruction
    end
end
% pseudo code for NC-based models applied to MCI/AD subjects
for i in 1,2, ...,30 % there are 30 channels
    assemble training set using data of all NC subjects
    for j in 1,2, ..., 33 % there are 16 MCI, 17 AD subjects
        % reconstruct channel i from other channels
        train the reconstruction model using training set
```

```
        apply the model to channel i of participant j
        evaluate quality of reconstruction
    end
end
```


Quality Scores for Reconstructions

      The models just described are used to reconstruct 2-min samples of artificially "deleted" data for each participant for each protocol condition. The reconstructed channel $\hat{y}(t)$ is then compared to the actual data for the given channel $y(t)$ and the quality of the reconstruction is evaluated using the Q_1 quality score implemented in the PhysioNet 2010 Challenge. The quality score used is defined by Equation (7.2), where σ represents the standard deviation of the actual data $y(t)$ and MSE represents the mean squared error (i.e., the average of the squared differences between the reconstructed signal $\hat{y}(t)$ and the actual data $y(t)$). Thus, the quality score, Q, is the larger value between the R-squared value and 0.

      For each protocol condition, the three group-based models are applied and quality scores are computed for each channel for all participants. The 30 channels used in analyses are grouped into 6 scalp regions based on their arrangement and location on the scalp. The regions include: (1) central (C); (2) frontal (F); (3) left temporal (L); (4) occipital (O); (5) parietal (P); and (6) right frontal (R); see Fig.2.1 for regional boundaries. For each group-based model, the quality scores are averaged over each scalp region, for a total of 18 (3 group-based models and 6 regions) regional average quality scores for the each protocol condition.

Principal Component Analysis

      For each protocol condition, a 48 x 18 matrix R of regional average quality scores for all participants is arranged as shown in Equation (7.7):

$$R = \begin{bmatrix} q_1 \\ \vdots \\ q_{48} \end{bmatrix}, \quad (7.7)$$

where $q_i = [Q_C^{NC}, Q_F^{NC}, Q_L^{NC}, Q_O^{NC}, Q_P^{NC}, Q_R^{NC}, Q_C^{MCI}, Q_F^{MCI}, Q_L^{MCI}, Q_O^{MCI}, Q_P^{MCI}, Q_R^{MCI}, Q_C^{AD}, Q_F^{AD}, Q_O^{AD}, Q_P^{AD}, Q_R^{AD}]$ is a row vector of regional average quality scores for participant i ($i = 1, \ldots, 48$), superscripts denote the model-basis group, and subscripts denote region. The mean is subtracted from the matrix R and the resulting matrix θ is then decomposed via singular value decomposition into the three matrices U, S, and V, as shown in Equation (7.8):

Table 7.4. Default Parameters Used in Neural Networks for EEG Channel Reconstruction

|	
Number of hidden layers	2
Number of neurons	5 for the first hidden layer and 1 for the second hidden layer
Transfer functions	`tansig` for 1st hidden layer and `purelin` for 2nd hidden layer
Training data	
For Group A participants	2 minutes of data from all but current Group A participants for given protocol condition
For other participants	2 minutes of data from all Group A participants for given protocol condition
Training epochs	40
Performance function	Mean squared normalized error (MSNE)
	No delay vector will be used; only concurrent data
Delay vector d	
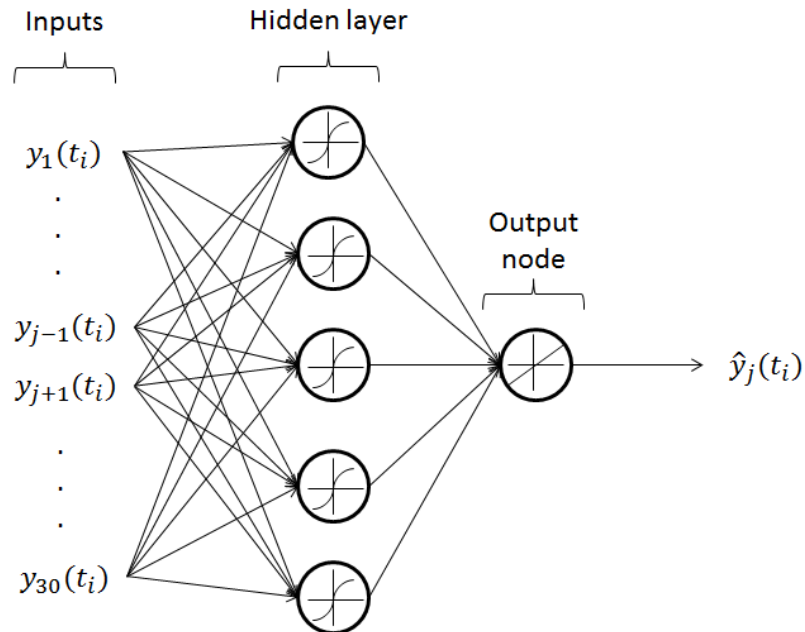
Fig. 7.9. Schematic of Neural Network Used in Reconstructing EEG. Note that inputs to the network are *concurrent* data (data at time t_i) from all EEG channels except channel j (N = 30 channels – 1 = 29 inputs; output of the network is a reconstruction $\hat{y}_j$ of actual data y_j from channel j).

$$\theta = USV^T, \quad (7.8)$$

where U and V are unitary matrices such that $UU^T = I$ and $VV^T = I$ and S is a diagonal matrix, the diagonal of which is comprised of singular values s_j that indicate the relative energy ($E_j = s_j / \sum s_j$) in the corresponding principal components p_j, $j = 1, \dots, 18$. The principal components p_j of the regional average quality score matrix R are then defined by Equation (7.9), where v_j is the jth column of V. For each protocol condition, the first two principal components (p_1, and p_2) of the matrix θ were used as features in a three-way classification scheme based on binary SVM models.

$$p_j = \theta v_j, \quad (7.9)$$

Three-way Classification via Binary Classifiers

For each protocol condition, a three-way classification scheme ss constructed based on binary SVM classifiers using the pairwise coupling approach proposed by Hastie and Tibshirani [54]. For a given record, binary SVM classifiers (i.e., MCI vs. NC, AD vs. NC, and MCI vs. AD) are trained using all other available records and then applied to the given record via the leave-one-out principle. If two out of three of the SVM binary classifiers classify a record as belonging to class i, then the final decision of the three-way classifier is to classify the record as belonging to class i. Otherwise, the probability that a record belongs to each class, P_i, $i = 1, 2, 3$, is then estimated as follows, and the final decision of the three-way classifier is to chose the class corresponding to the largest probability, $\operatorname{argmax}_i(P_i)$.

Results for Discrimination of MCI and AD Using EEG Channel Reconstruction Quality Measures

LOOCV accuracies for binary model-basis group vs. other groups for individual regional averages are summarized in Table 7.5. As can be seen in Table 7.5, the LOOCV accuracies appear to be relatively consistent across protocol conditions for most regional averages. Higher LOOCV accuracies may be interpreted as indicating greater within-group similarity for the model-basis group. This is perhaps more clearly seen in Fig. 7.10, where group average quality scores for each model and protocol condition are plotted.

The energies corresponding to principal components for all three conditions are presented in Fig.7.11. The first two principal components account for 37.4-38.4% of the total energy. The entries of vectors v_1 and v_2 corresponding to the 18 regional quality scores are presented in Fig.7.12. Interestingly, the entries in v_1 corresponding to NC- or MCI-based regional quality scores have opposite sign to those corresponding to AD-based regional quality scores. This pattern suggests that the first principal component somehow reflects differences between AD-based regional averages from NC- or MCI-based regional averages. The entries in v_2 corresponding to NC-based regional averages have opposite sign to those entries corresponding to MCI- or AD-based regional averages, suggesting that the second principle component reflects differences between NC-based regional averages and MCI- or AD-based regional averages.

NC, MCI, and AD participants' data are plotted on principal component axes in Fig.7.13, Fig.7.14, and Fig.7.15 for the REO condition, counting task, and REC condition, respectively. As can be seen in the figures, the groups are clearly separable in the 2D space, with the exception of one normal participant whose data appears in the AD regions for all three conditions.

Three-way classification results for the REO condition are presented in Table 7.6. Of those records classified as NC, 93.3% are NC; of those records classified as MCI, 93.8% are MCI; and of those classified as AD, 100% are AD. Of all the normal participants, 93.3% of them are correctly identified; of all the MCI participants, 93.8% are correctly identified; and of all the AD participants, 100% are correctly identified. Overall, the prediction accuracy is 95.8%.

Table 7.5. Discriminatory Power of Individual Regional Average EEG Reconstruction Quality Scores

	Q_C^{NC}	Q_F^{NC}	Q_L^{NC}	Q_O^{NC}	Q_P^{NC}	Q_R^{NC}
NC-Based Model Regional Averages'						
NC vs. MCI/AD Leave-one-out Cross-Validation Accuracies						
Resting Eyes Open	83.3%	75.0%	68.8%	85.4%	83.3%	64.6%
Counting Eyes Closed	89.6%	72.9%	75.0%	91.7%	91.7%	85.4%
Resting Eyes Closed	85.4%	83.3%	75.0%	87.5%	89.6%	75.0%

	Q_C^{MCI}	Q_F^{MCI}	Q_L^{MCI}	Q_O^{MCI}	Q_P^{MCI}	Q_R^{MCI}
MCI-Based Model Regional Averages'						
MCI vs. NC/AD Leave-one-out Cross-Validation Accuracies						
Resting Eyes Open	75.0%	87.5%	77.1%	83.3%	77.1%	77.1%
Counting Eyes Closed	85.4%	95.4%	79.2%	79.2%	70.8%	81.3%
Resting Eyes Closed	77.1%	89.6%	75.0%	72.9%	68.8%	85.4%

	Q_C^{AD}	Q_F^{AD}	Q_L^{AD}	Q_O^{AD}	Q_P^{AD}	Q_R^{AD}
AD-Based Model Regional Averages'						
AD vs. NC/MCI Leave-one-out Cross-Validation Accuracies						
Resting Eyes Open	79.2%	70.8%	81.3%	81.3%	75.0%	79.2%
Counting Eyes Closed	81.3%	64.6%	70.8%	64.6%	64.6%	77.1%
Resting Eyes Closed	72.9%	81.3%	58.3%	70.8%	72.9%	75.0%

LOOCV accuracies obtained using SVM classifiers with quadratic kernel function. Q = regional average quality scores, where superscripts denote the model-basis group, and subscripts denote region
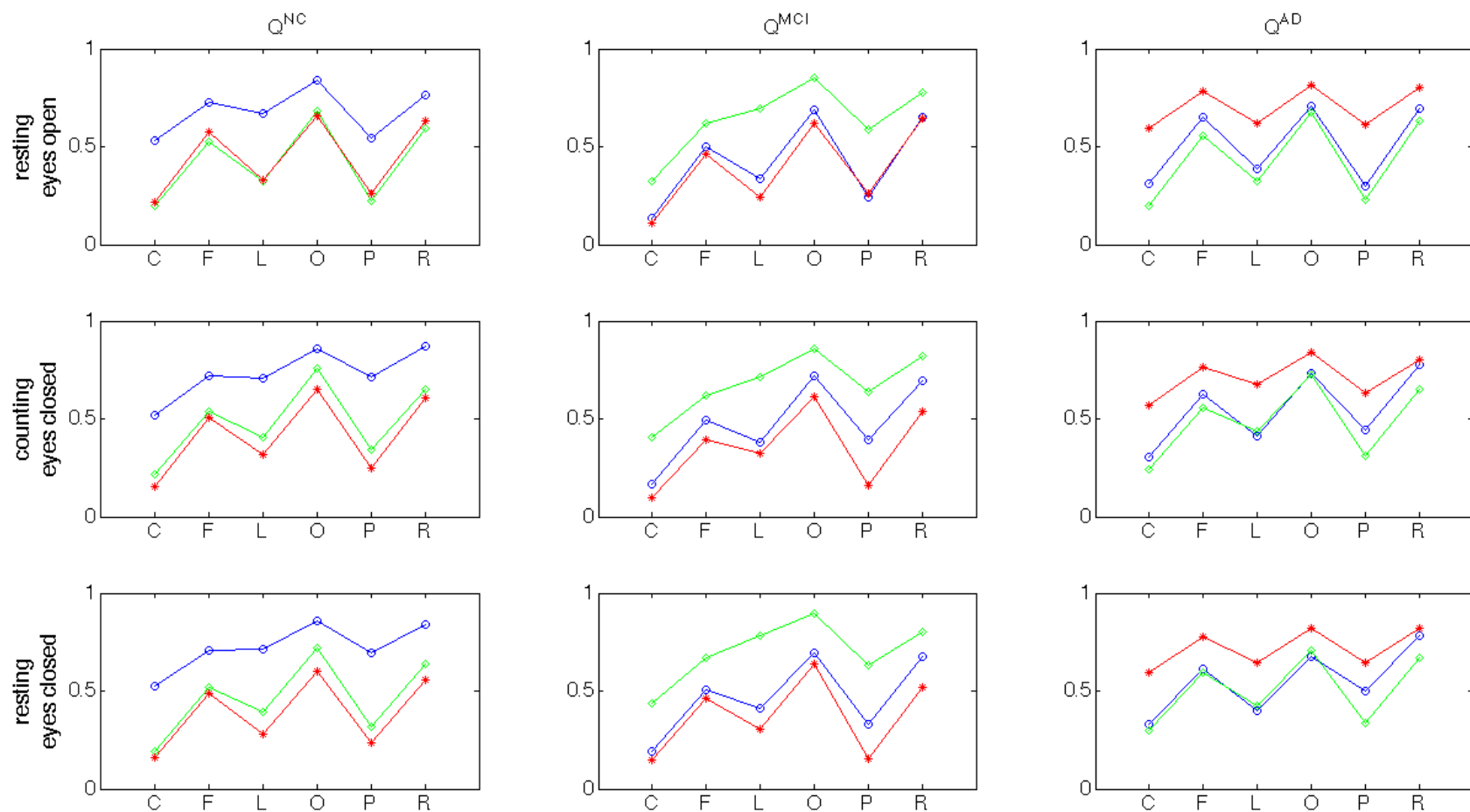
Fig. 7.10. Regional Average Quality Scores. Blue circles correspond to average of NC participants, green diamonds correspond to average of MCI participants, and red stars correspond to average of AD participants. Each row of plots presents the regional average quality scores for one of the three protocol conditions. Each Column of plots corresponds to a different group used to generate the reconstruction models. For example, the first column of plots presents regional averages obtained using a reconstruction model trained on data from normal participants. Note that, on average, the qualities of reconstructions for participants other than those belonging to the group used to train the model are significantly lower. Recall that models were trained in a leave-one-out manner.

Fig.7.11. Energies of Principal Components of Regional Averages. Note that for all three protocol conditions the first two principal components account for approximately 37% of the energy.

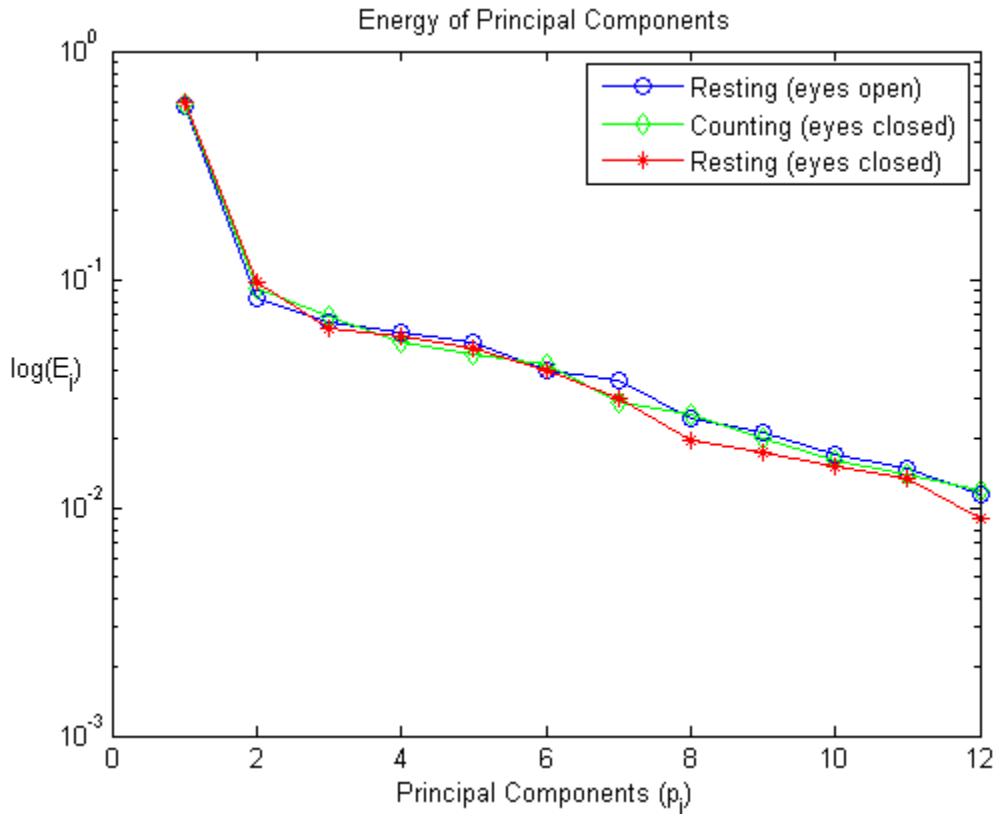Three-way classification results for the counting task are presented in Table 7.7. Of those records classified as normal, 93.3% are normal; of those classified as MCI, 100% are MCI; and of those classified as AD, 94.4% are AD. 93.3% of normal participants, 93.8% of MCI participants, and 100% of AD participants are correctly identified. Overall, the prediction accuracy is 95.8%.

Three-way classification results for the REC condition are presented in Table 7.8. Of those records classified as normal, 100% are normal; of those classified as MCI, 100% are MCI; and of those classified as AD, 94.4% are AD. 93.3% of normal participants are classified as normal, and 100% of MCI and AD participants are classified as MCI or AD correctly. The overall accuracy is 97.9%.

The REO and counting task three-way classifiers perform equally well in overall accuracy while the REC classifier performed the best. Misclassified NC participants are classified as MCI or AD, misclassified MCI participants are classified as NC, and no AD participants are misclassified.
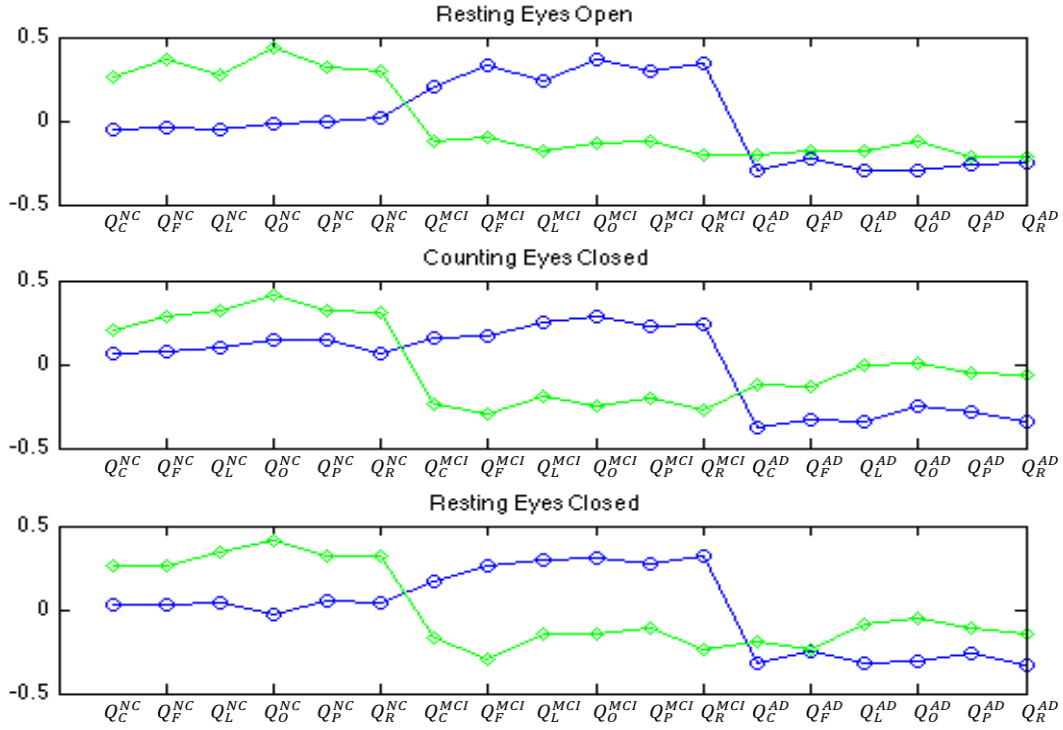
Fig.7.12. Entries of Vectors Used to Compute Principal Components. Indices 1- 6 correspond to regional averages using NC models; indices 7-12 correspond to regional averages using MCI models; indices 13-18 correspond to regional averages using AD models. Note that entries in v_1 (circles) used to compute the first principal component have opposite and/or lesser magnitude sign for NC- and MCI-based regional averages compared to AD-based regional averages; entries in v_2 (diamonds) have opposite sign for NC-based regional averages compared to MCI- and AD-based regional averages

Discussion and Conclusions

Application of ANNs for Physiological Signal Reconstruction

Earlier in this Chapter, methods for the reconstruction of physiological signals using iterative retraining and accumulated averaging of artificial neural networks are developed. Extensive numerical investigations using physiological records from the PhysioNet 2010 Challenge demonstrate that these techniques can significantly improve the accuracy of reconstructions. To the author's best knowledge, these techniques have not been applied to neural networks before.

Fig.7.13. 2D Representation of Regional Average Quality Scores for REO Condition.

Table 7.6. Confusion Table of 3-Way Results for REO Condition

		Predicted Classes			
		NC	MCI	AD	
True Classes	NC	14	1	0	93.3%
	MCI	1	15	0	93.8%
	AD	0	0	17	100%
		93.3%	93.8%	100%	Overall Acc.: 95.8%

126

Fig.7.14. 2D Representation of Regional Average Quality Scores for Counting Task.

Table 7.7. Confusion Table of 3-Way Results for Counting Task

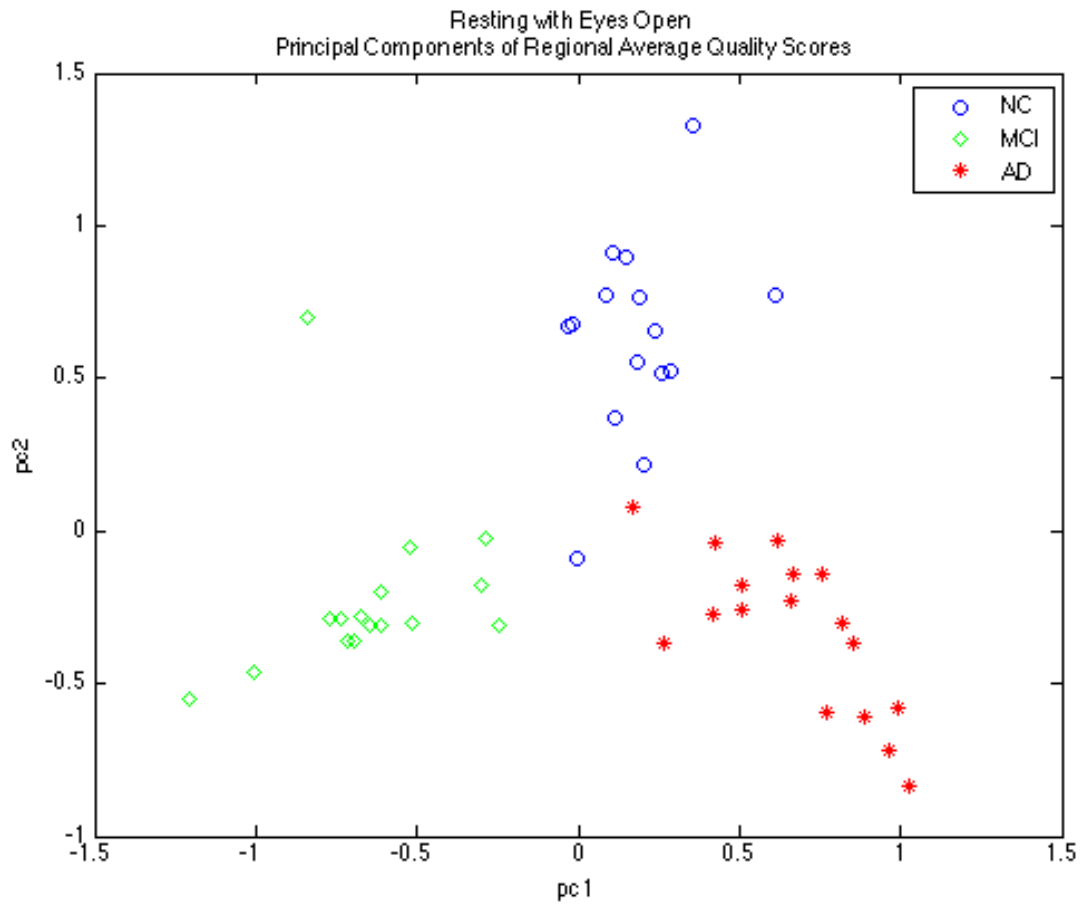|		Predicted Classes			
		NC	MCI	AD	
True Classes	NC	14	0	1	93.3%
	MCI	1	15	0	93.8%
	AD	0	0	17	100%
		93.3%	100%	94.4%	Overall Acc.: 95.8%

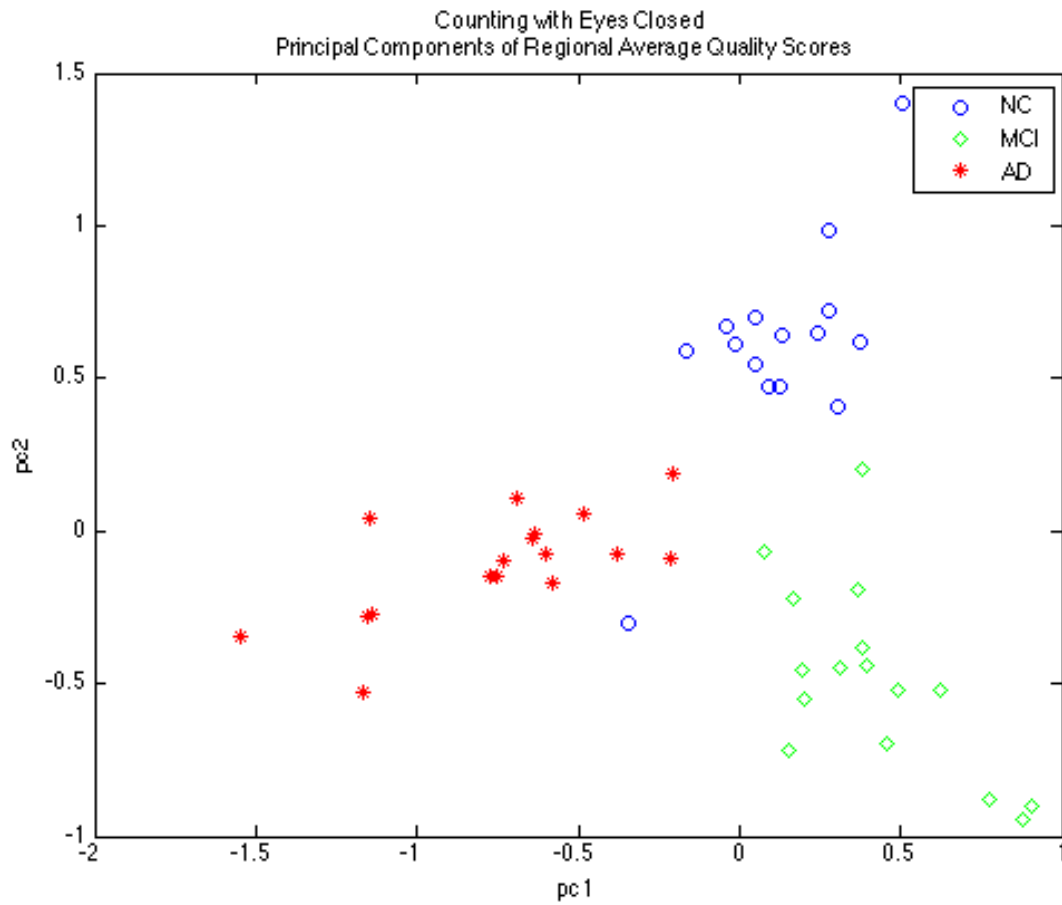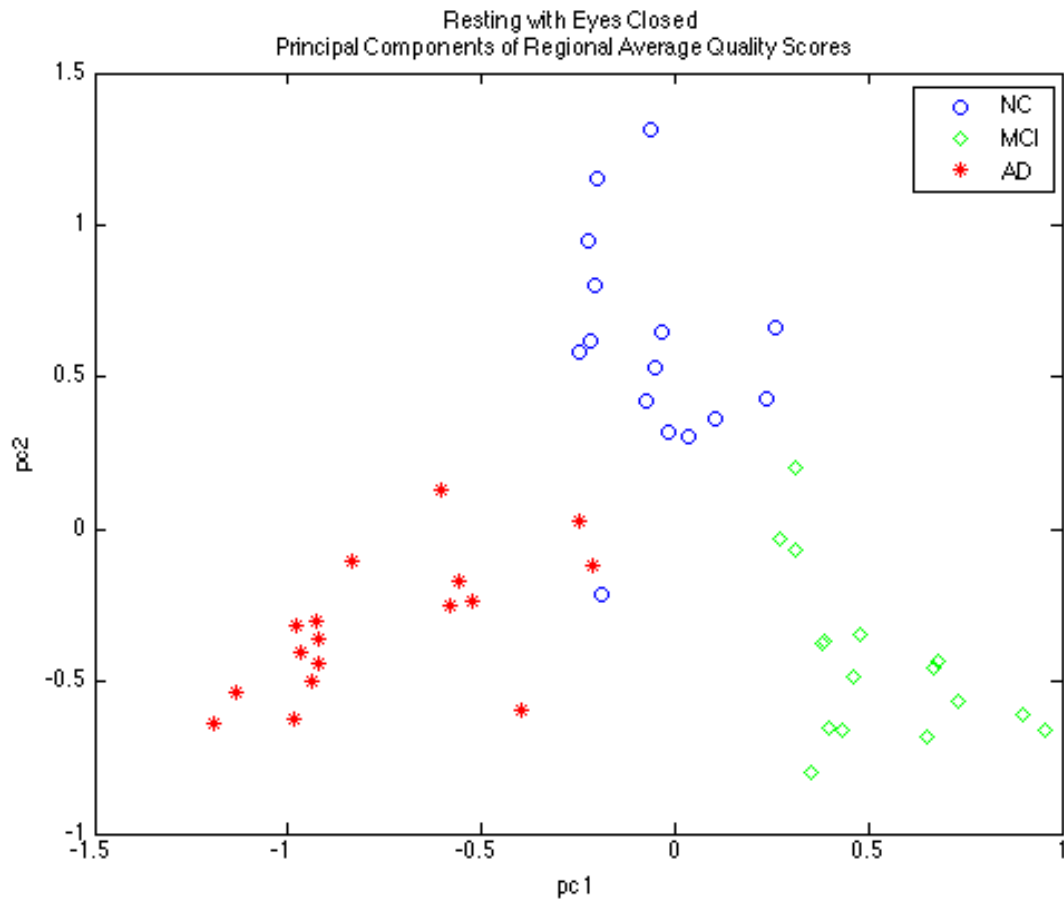**Fig.7.15.** 2D Representation of Regional Average Quality Scores for REC Condition.

Table 7.8. Confusion Table of 3-Way Results for REC Condition

		Predicted Classes			
		NC	MCI	AD	
True Classes	NC	14	0	1	93.3%
	MCI	0	16	0	100%
	AD	0	0	17	100%
		100%	100%	94.1%	Overall Acc.: 97.9%

Empirical studies demonstrated that the iterative retraining and the accumulated averaging techniques are effective for various target signals and are robust under variations of network parameters. It is shown that short-term memory works the best for ECG targets while mixed memory can improve the accuracy for other signals. Furthermore, it is demonstrated that increasing the length of the delay vector may lead to better reconstructions for some targets.

It is interesting to note that the reconstruction results depend on the number of neurons in the network. While more neurons may lead to more accurate reconstructions, the results using just a few neurons are still comparable with those obtained from many other techniques. Meanwhile, reducing the number of neurons can reduce computational time to a few seconds. This indicates the potential of the developed models for real-time reconstruction applications.

Impressive reconstructions are obtained, even for signals with random fluctuations, chaotic features, and saturations. Further theoretical investigations on these algorithms will be useful in determining the full potentials and limitations. These techniques could see future application for detection of changes in patient state, recognition of intervals of signal corruption, and derivation critical physiological parameters when primary signals become unavailable or unreliable [93]. These methods have many applications in settings ranging from sleep studies to surgery to sports medicine to intensive care.

Application of ANN Signal Reconstruction to Detection for Cognitive Deficits
In the previous section of this Chapter, neural network models are developed to reconstruct missing information from EEG of cognitively normal older adults and those with MCI or early AD. Models are developed for each of the three groups (NC, MCI, and early AD) and applied to all participants in order to reconstruct artificially "deleted" 2-min samples of EEG taken during rest and a simple cognitive task. The qualities of reconstructions were evaluated for accuracy on a regional basis. Principal components of regional average quality scores for the three models are used as features in an SVM model in order to discriminate between groups. The nonlinear channel reconstruction metrics presented here allow for accurate discrimination between the three groups.

The high discrimination accuracy achieved here is due to the fact that, on average, models perform more poorly in reconstructing EEG records of participants belonging to groups other than the model-basis group. For example, the NC-based model produces significantly more accurate reconstructions, on average, for NC participants than for MCI or early AD participants. While the reason for the poorer quality of reconstructions for MCI and AD participants is unclear, it may be hypothesized that the relationships between EEG channels mapped by neural network models trained on normal aged individuals are less applicable to MCI and AD EEG records. That is, EEG nonlinear inter-channel correlation patterns appear to exhibit greater within-group similarities than between-group similarities. The differences between groups' relationships of EEG channels may reflect differences in functional organization of information processing in the brain. To the authors' best knowledge, the application of neural networks designed to reconstruct

missing information from EEG has not been previously investigated as a potential diagnostic tool for detecting dementia.

The high accuracy achieved here is possible through the use of relatively simple neural networks, comprised of only one hidden layer with five neurons. Choice of structure for the network is based on previous investigations by the authors who examined the reconstruction of missing ICU machine signals as presented in the second section of this Chapter. While the use of more neurons may lead to more accurate reconstructions, the results presented here using only a handful of neurons suggest that only a few neurons are sufficient for discriminating MCI and AD from normal controls and each other.

Neuroimaging tools such as structural MRI can detect changes in the brain structure critical to cognitive ability long before clinical diagnosis of cognitive decline. Other biomarkers of the AD pathology cascade can signal early progression of the disease before MRI detection [37]. EEG technology is sensitive to cellular changes in brain functions that are likely earlier biomarkers compared to structural MRI indicators. The results of this work suggest the possible use of neural network reconstructions of scalp EEG as a means for objectively discriminating among normal, MCI, and AD participants and assessing an individual's risk profile for cognitive impairment. Results suggest that a simple discrimination model utilizing SVM and the features presented here may be a viable basis for future development of a diagnostic screening tool for MCI and early AD with applicability in the primary care setting. Such a rapid, simple, and cost-effective tool could also prove useful in the drug discovery process.

CHAPTER 8
SUMMARY, CONTRIBUTIONS, AND RECOMMENDATIONS
FOR FUTURE WORK

Chapter 1

In Chapter 1, a detailed background is provided, including: an introduction to the physiological mechanisms involved in EEG; the pathology of TBI, MCI, and AD; current methods used to diagnose and evaluate these disorders; a summary of the current literature regarding diagnosis via EEG; and details of the EEG data used for the studies presented.

Chapter 2

In Chapter 2, an exploration of event-related Tsallis entropy measures as potential biomarkers of neurological disease is presented. The approach developed is applied toward the discrimination of TBI and MCI using EEG recorded during working memory tasks. En lieu of complex ERP analysis, which generally requires redundant protocols and multiple trials, the method presented here using event-related Tsallis entropy demonstrates that analysis of EEG data from a single trial has the potential to successfully discriminate TBI vs. NC and MCI vs. NC. The results in this work demonstrate a strong correlation between Tsallis entropy-based TEFs and the presence of moderate to severe TBI and MCI.

Chapter 3

In Chapter 3, an exploration of event-related MSE measures as potential indicators of neurological disease is presented. The approach developed is applied toward the discrimination of TBI, MCI, and AD using EEG recorded during working memory tasks. The method is also adapted for NER data in order to discriminate MCI and AD using EEG recorded during resting states and a simple cognitive task. The results in this work demonstrate a strong relationship between event-related MSE measures and the presence of cognitive deficits. For MCI and AD discrimination, the method appears to be significantly more effective using working memory compared to NER data. The high accuracy achieved here in discriminating between MCI and NC is encouraging as there is great interest in being able to detect cognitive decline that may be associated with AD at the earliest stages. The results of this work suggest the potential for the use of MSE complexity features representing scalp electrical activity as a means for objectively discriminating between normal, MCI, and AD participants.

Chapter 4

In Chapter 4, a methodology for developing intra- and inter-regional transfer entropy measures capable of characterizing differences in NER EEG of MCI and AD individuals is described. Specifically, the features proposed here are intended to represent trends in the delay of the transfer of the information present in EEG signals between major regions of the scalp. The successful discrimination between the three groups of EEG records (NC, MCI, and AD) are the result of differences in the dynamics of the information distribution in EEG voltages across the scalp in resting states and during a simple cognitive

task. It is possible the observed differences in these information dynamics may be influenced by alterations in the functional organization of the brain as a result of cognitive decline. The results for the three-way discrimination presented here are encouraging, especially those for MCI, as detection of AD at the earliest possible stage is currently of great interest in the field. The three-way classification scheme via binary classifiers presented here allows for the differentiation of the three groups without a priori knowledge that individuals fall into two of the three groups.

Chapter 5

In Chapter 5, a study explores differences in common spectral and complexity measures of EEG on a regional and global basis for the discrimination of preclinical dementia from normal aging during NER conditions. The successful discrimination between the three groups of EEG records (NC, MCI, and AD) are the result of differences in regional electrical activity in specific frequency bands in resting states and during a simple cognitive task. The observation of increased theta activity and decreases in alpha and beta activity for MCI and AD participants compared to normal controls during the REC condition are consistent with expected trends from the literature [37].

Chapter 6

In Chapter 6, a method for quantifying differences in EEG inter-channel synchronization for MCI and AD is presented. The method involves analyzing inter-channel coherence measures via graph theory. The success of SVM discrimination between binary groupings of the three groups of EEG records (NC, MCI, and AD) are the result of differences in uniformity of electrical activity in specific frequency bands during resting states and a simple cognitive task. It is possible that these differences may be the results of characteristic changes in brain network functional organization (e.g., compensatory mechanisms) as a result of neurological degeneration.

Chapter 7

In Chapter 7, methods for reconstruction missing data in multivariate biomedical signals using artificial neural networks are presented. New techniques of signal reconstruction based on iterative retraining and accumulated averaging of neural networks are presented. The effectiveness and robustness of these techniques are demonstrated using data records from the Computing in Cardiology/PhysioNet Challenge 2010. The influences of a few important parameters on the accuracy of reconstructions are also explored. The developed techniques may be used to detect changes in patient state and to recognize intervals of signal corruption.

Also in Chapter 7, novel EEG biomarkers for discriminating normal aging from MCI and early AD using Sugihara causality are presented. Sugihara causality extends to systems that are not covered by the current Granger causality paradigm. First, a reconstruction model is developed for each EEG channel, which predicts the signal in the current channel using data of the other available channels. The reconstruction model of the target channel is trained using NC, MCI, or AD records to generate a NC-, MCI-, or AD-specific model, respectively. To avoid information leak, the training is based on the leave-one-out

principle. When the reconstruction model is applied to an EEG record, a score is computed to represent the quality of prediction by comparing the predicted signal and the original signal. The quality scores capture characteristic changes in EEG activity due to cognitive deficits. Compared to other EEG biomarkers, the quality scores have excellent potential as individualized biomarkers in detection of pathophysiological changes in early AD.

Contributions

Significant contributions of the work presented here include:

(1) Novel entropy-based methods for analyzing event-related EEG data that may be applied toward the evaluation of neurological disorders.

(2) Recommendations for which common spectral and complexity features currently used in characterizing EEG appear to best discriminate MCI and AD, including which scalp regions and data collection procedures provide the greatest benefit.

(3) Development of novel artificial neural network techniques for the reconstruction of missing data in multivariate physiological that have a multitude of possible applications.

(4) Presentation of an innovative design of EEG biomarkers using Sugihara causality as basis for detection of changes in functional organization of the brain due to dementia. To the author's best knowledge, this is the first application of Sugihara causality in biomedical data.

(5) Indexing of observations from current work may provide insight for future researchers.

Limitations and Recommendations for Future Work

The reported injuries in the TBI participants were widespread across the brain. One limitation of this study is the lack of access to data to allow evaluation of the correlation between the areas of brain injury with TEF results. In a future study, examining participants with acute damage in a known area of the brain may be able to provide further insights into area-specific TBI.

The current methods cannot be readily applied to the clinical setting since they require 25-30 EEG channels and take about 30 min to collect the data (including setup time for working memory methods). A shorter protocol and fewer electrodes would be required for more convenient application. In addition, larger sample sizes and new test samples would also be needed to further validate the approaches before they could be applied in a private practice setting.

The goal of this work is to provide a meaningful addition to basic research in the current literature regarding the application of EEG for the detection, evaluation, and monitoring of cognitive deficits.

LIST OF REFERENCES

[1] Abásolo, D., J. Escudero, R. Hornero, C. Gómez, and P. Espino. Approximate entropy and auto mutual information analysis of the electroencephalogram in Alzheimer's disease patients. Med. Biol. Eng. Comput. 46(10): 1019-1028, Oct. 2008.

[2] Abásolo, D., R. Hornero, P. Espino, D. Álvarez, and J. Poza. Entropy analysis of the EEG background activity in Alzheimer's disease patients. Physiol. Meas. 27(3): 241-253, Mar. 2006.

[3] Abásolo, D., R. Honero, P. Espino, J. Poza, C. Sánchez, and R. de la Rosa. Analysis of regularity in the EEG background activity of Alzheimer's disease patients with approximate entropy. Clin. Neurophysiol. 116(8): 1826-1834, Aug. 2005.

[4] Abou-Saleh, M., C. Katona, and A. Kumar. Principles of Geriatric Psychiatry. West Sussex, UK: Wiley and Sons, 2011.

[5] Ancona, N, D. Marinazzo, and S. Stramaglia. Radial basis function approach to nonlinear Granger causality. Phys.. Rev. E. Stat. Nonlin. Soft. Matter Phys. 70(5 Pt. 2): 056221, Nov. 2004.

[6] Angelakis, E., J. Lubar, S. Stathopoulou, and J. Kounios. Peak alpha frequency: an electroencephalographic measure of cognitive preparedness. Clin. Neurphysiol. 115(4): 887-897, Apr. 2004.

[7] Anghinah, R., P. Kanda, M. Jorge, E. Lima, L. Pascuzzi, and A. Melo. Alpha band coherence analysis of EEG in healthy adults and Alzheimer's type dementia. Arg. Neuropsiquiatr. 58(2A): 272-275, Jun. 2000. [Article in Portuguese.]

[8] Anoop, A., P. Singh, R. Jacob, and S. Maji. CSF biomarkers for Alzheimer's disease diagnosis. Int. J. Alzheimer Dis. 2010: 1-12, Jun. 2010.

[9] Ariza, M., J. Serra-Grabulosa, C. Junqué, B. Ramírez, M. Mataró, A. Poca, N. Bargalló, and J. Sahuquillo. Hippocampal head atrophy after traumatic brain injury. Neuropsychologia. 44(10): 1956-1961, Dec. 2006.

[10] Averbeck, B., and M. Seo. The statistical neuroanatomy of frontal networks in the macaque. PLoS comput. Biol. 4(4): e1000050, Apr. 2008.

[11] Aviyente, S. A measure of mutual information on the time-frequency plane. Proc. IEEE ICASSP. 4: 481-484, Mar. 2005.

[12] Aviyente, S. Information-theoretic signal processing on the time-frequency plane and applications. Proc. EUSPIPCO 2005.

[13] Babiloni, C., R. Ferri, G. Binetti, A. Cassarino, G. Forno, M. Ercolani, F. Ferreri, G. Frisoni, B. Lanuzza, C. Miniussi, F. Nobili, G. Rodriguez, F. Rundo, C. Stam, T. Musha, F. Vecchio, and P. Rossini. Fronto-parietal coupling of brain rhythms in mild cognitive impairment: a multicentric EEG study. Brain. Rex. Bull. 69(1): 63-73, Mar. 2006.

[14] Babiloni, C., G. Frisoni, M. Pievani, F. Vecchio, R. Lizio, M. Buttiglione, C. Geroldi, C. Fracassi, F. Eusebi, R. Ferri, and P. Rossini. Hippocampal volume and cortical sources of EEG alpha rhythms in mild cognitive impairment and Alzheimer disease. Neuroimage. 44(1): 123-135, Jan. 2009

[15] Baker, M., K. Akrofi, R. Schiffer, and M. O'Boyle. EEG patterns in mild cognitive impairment (MCI) patients. Open Neuroimag. J. 2: 52-55, Aug. 2008.

[16] Bartzokis, G., P. Lu, and J. Mintz. Quantifying age-related myelin breakdown with MRI: novel therapeutic targets for preventing cognitive decline and Alzheimer's disease. J. Alzheimer Dis. 6(6 Suppl.): S53-S59, Dec. 2004.

[17]   Basset, D, and E. Bullmore. Small-world brain networks. Neuroscientist. 12(6): 512-523, Dec. 2006.

[18]   Berzerianos, A., S. Tong, and N. Thakor. Time-dependent entropy estimation of EEG rhythm changes following brain ischemia. Ann. Biomed. Eng. 31(2): 221-232, Feb. 2003.

[19]   Besthorn, C., H. Fröstl, C. Geiger-Kabish, H. Sattel, T. Gasser, and U. Schreiter-Gasser. EEG coherence in Alzheimer's disease. Electroencephalogr. Clin. Neurophysiol. 90(3): 242-245, Mar. 1994.

[20]   Besthorn, C., R. Zerfass, C. Geiger-Kabisch, H. Sattel, S. Danial, U. Schreiter-Gasser, and H. Fröstl. Discrimination of Alzheimer's disease and normal aging by EEG data. Electroencephalogr. Clin. Neurophysiol. 103(2): 241-248, Aug. 1997.

[21]   Bishop, C. Pre-processing and Feature Extraction. In: Neural Networks for Pattern Recognition. New York, NY: Oxford University Press, Inc., ch.8.

[22]   Blanco, S., Q. Quiroga, O. Rosso, and S. Kochen. Time-frequency analysis of electroencephalogram series. Phys. Rev. E. 51(3): 51, Mar. 1995.

[23]   Braitenberg, V. and A. Schüz. Cortex: Statistics and Geometry of Neuronal Connectivity. 2nd ed. Berlin: Springer, 1998.

[24]   Brassen, S., D. Braus, W. Weber-Fahr, H. Trost, S. Moritz, and G. Adler. Late-onset depression with mild cognitive deficits: electrophysiological evidences for a preclinical dementia syndrome. Dement. Geriatr. Cogn. Disord. 18(3-4): 271-277, Jul. 2004.

[25]   Brenner, R., R. Ulrich, D. Spiker, R. Sclabassi, C. Reynolds III, R. Marin, and F. Boller. Computerized EEG spectral analysis in elderly normal, demented and depressed subjects. Electroencephalogr. Clin. Neurophysiol. 64(6): 483-492, Dec. 1986.

[26]   Broster, L., J. Li, C. Smith, G. Jicha, F. Schmitt, and Y. Jiang. Repeated retrieval during working memory is sensitive to amnestic mild cognitive impairment. Submitted.

[27]   Bullmore, E. and O. Sporns. Complex brain networks: graph theoretical analysis of structural and functional systems. Nat. Rev. Neurosci. 10(3): 186-198, Mar. 2009.

[28]   Cao, C. and S. Slobounov. Application of a novel measure of EEG non-stationarity as 'Shannon entropy of the peak frequency shifting' for detecting residual abnormalities in concussed individuals. Clin. Neurophysiol. 122(7): 1314-1321, Jul. 2011.

[29]   Carlson, R. Physiology of Behavior. 9th ed. Amherst, ME: Pearson Education, Inc., 2007.

[30]   Cernak, I., Z. Wang, J. Jiang, X. Bian, and J. Savic. Ultrastructural and functional characteristics of blast injury-induced neurotrama. J. Trauma. 50(4): 695-706, Apr. 2001.

[31]   Chen, Y., G. Rangarajan, J. Feng, and M. Ding. Analyzing multiple nonlinear time series with extended Granger causality. Phys. Lett. A. 324(1): 26-35, Apr. 2004.

[32]   Costa, M., A. Goldberger, and C.-K. Peng. Multiscale entropy analysis of biological signals. Phys. Rev. E. 71(2 Pt. 1): 021906, Feb. 2005.

[33]   Costa, M., A. Goldberger, and C.-K. Peng. Multiscale entropy analysis of complex physiologic time series. Phys. Rev. Lett. 89(6): 068102, Aug. 2002.

[34]   Cover, T. and J. Thomas. Elements of Information Theory. New York, NY: Wiley, 1991.

[35]   Czigler, B., D. Csikós, Z. Hidai, Z. Gaál, E. Csibri, E. Kiss, P. Salacz, and M. Molnár. Quantitative EEG in early Alzheimer's disease patients—power spectrum and complexity features. Int. J. Psychophysiol. 68(1): 75-80, Apr. 2008.

[36]   Dauwels, J., F. Vialatte, and A. Cichocki. A comparative study of synchrony measure for the early diagnosis of Alzheimer's disease based on EEG. NeuroImage. 49(1): 668-693, Jan. 2010.

[37]   Dauwels, J., F. Vialatte, A., and A. Cichocki. Diagnosis of Alzheimer's disease from EEG signals: where are we stading? Curr. Alzheimer Res. 7(6): 487-505, Sep. 2010.

[38]   Dauwels, J., F. Vialatte, C. Latchoumane, J. Jeong, and A. Cichocki. EEG synchrony analysis for early diagnosis of Alzheimer's disease: a study with serveral synchrony measures and EEG data sets. Proc. IEEE Eng. Med. Biol. Soc. 2009: 2224-2227, 2009.

[39]   De Meyer, G., F. Shapiro, H. Vanderstichele, E. Vanmechelen, S. Engelborghs, P. De Deyn, E. Coart, O. Hansson, L. Minthon, H. Zetterberg, K. Blennow, L. Shaw, and J. Trojanowski. Diagnosis-independent Alzheimer's disease biomarker signature in cognitively normal elderly people. Arch. Neurol. 67(8): 949-956, Aug. 2010.

[40]   Docktree, P., S. Kelly, R. Roche, M. Hogan, R. Reilly, and I. Robertson. Behavioural and physiological impairments of sustained attention after traumatic brain injury. Brain Res. Cogn. Brain Res. 20(3): 403-414, Aug. 2004.

[41]   Dong, J., D. Liu, C. Zhang, J. Ma, G. Wang, D. Guo, Y. Liu, H. Zhong, J. Zhang, C.-K. Peng, and J. Fang. Automated sleep staging technique based on the empirical mode decomposition algorithm: a preliminary study. Adv. Adapt. Data Anal. 2(2): 267-276, 2010.

[42]   Escudero, J., D. Abásolo, R. Honero, P Espino, and M. López. Analysis of electroencephalograms in Alzheimer's disease patients with multiscale entropy. Physiol Meas. 27(11): 1091-1106, Nov. 2006.

[43]   Farrarini, L., I. Veer, E. Baerends, M. van Tol, R. Renken, N. van der Wee, D. Veltman, A. Aleman, F. Zitman, B. Penninx, M. van Buchem, J. Reiber, S. Rombouts, and J. Miles. Hierarchical functional modularity in the resting-state human brain. Hum. Brain Mapp. 30(7): 2220-2231, Jul. 2009.

[44]   Fu, S., Y. Huang, Y. Luo, Y. Wang, J. Fedota, P. Greenwood, and r. Parasuraman. Perceptual load interacts with involuntary attention at early processing stages: event-related potentials studies. Neuroimage. 48(1): 191-199, Oct. 2009.

[45]   Gauthier, S., B. Reisberg, M. Zaudig, R. Petersen, K. Ritchie, K. Broich, S. Belleville, H. Brodaty, D. Bennet, H. Chertkow, J. Cummings, M. de Leon, H. Feldman, M. Ganguli, H. Hampel, P. Scheltens, M. Tierney, P. Whitehouse, and B. Winblad. Mild cognitive impairment. Lancet. 367(9518): 1262-1270, Apr. 2006.

[46]   Gianotti, L., G. Künig, D. Lehmann, P. Faber, R. Pascual-Marqui, K. Kochi, and U. Schreiter-Gasser. Correlation between disease severity and brain electic LORETA tomography in Alzheimer's disease. Clin. Neurophysiol. 118(1): 186-196, Jan. 2007.

[47]   Girvan, M. and M. Newman. Community structure in social and biological networks. Proc. Natl. Acad. Sci. USA. 99(12): 7821-7826, Jun. 2002.

[48]   Gloor, P. Hans Berger on the Electroencephalogram of Man. Amsterdam: Elsevier, 1969.

[49]   Goldberger, A. L. Amaral, L. Glass, J. Huasdorff, P. Ivanov, R. Mark, J. Mietus, G. Moody, C.-K. Peng, and H. Stanley. PhysioBank, PhysioToolkit, and PhysioNet:

components of a new research resource for complex physiologic signals. Circulation. 101: e215-e220, 2000.

[50]   Gosselin, N., C. Bottari, J. Chen, M. Petrides, S. Tinawi, E. de Guise, and A. Pitto. Electrophysiology and functional MRI in post-acute mild traumatic brain injury. J. Neurotrauma. 28(3): 329-341, Mar. 2011.

[51]   Grote, S., W. Böcker, W. Mutschler, B. Bouillon, and R. Lefering. Diagnostic value of the Glasgow Coma Scale for traumatic brain injury in 18,002 patients with severe multiple injuries. J. Neurotrauma. 28(4): 527-534, Apr. 2011.

[52]   Güntekin, B., E. Saatçi, and G. Yener. Decrease of evoked delta, theta and alpha coherences in Alzheimer's patients during a visual oddball paradigm. Brain Res. 1235: 109-116, Oct. 2009.

[53]   Gurney, K. An Introduction to Neural Networks. London, UK: Routledge, 1997.

[54]   Hastie, T. and R. Tibshirani. Classification by pairwise coupling. Ann. Statist. 26: 451-471, 1998.

[55]   He, Y., Z. Chen, G. Gong, and A. Evans. Neuronal networks in Alzheimer's disease. Neuroscientist. 15(4): 333-350, Aug. 2009.

[56]   Hellwig, B. A quantitative analysis of the local connectivity between pyramidal neurons in layers 2/3 of the rat visual cortex. Biol. Cybern. 82(2): 111-121, Feb. 2000.

[57]   Hermann, B., A. Thornton, and J. Joseph. Automated infant hearing screening using the ABR: development and validation. Am. J. Audiol. 4(2): 6-14, Jul. 1995.

[58]   Hermann, C., and T. Demiralp. Human EEG gamma oscillations in neuropsychiatric disorders. Clin. Neurophysiol. 116(12): 2719-2733, Dec. 2005.

[59]   Hidasi, Z., B. Czigler, P. Salacz, E. Csibri, and M. Molnár. Changes of EEG spectra and coherence following performance in a cognitive task in Alzheimer's disease. Int. J. Psychophysiol. 65(3): 252-260, Sep. 2007.

[60]   Hoffman, D., S. Stockdale, and L. Van Egren. Symptom changes in the treatment of mild traumatic brain injury using EEG neurofeedback. Clin. Electroencephalogr. 27(3): 164, 1996.

[61]   Hogan, M., G. Swanwick, J. Kaiser, M. Rowan, and B. Lawlor. Memory-related EEG power and coherence reductions in mild Alzheimer's disease. Int. J. Psychophysiol. 49(2): 147-163, Aug. 2003.

[62]   Hornero, R., D. Abásolo, J. Escudero, and C. Gómez. Nonlinear analysis of electroencephalogram and magnetoencephalogram recordings in patients with Alzheimer's disease. Philos. Transact. A Math. Phys. Eng. Soc. 367(1887): 317-336, Jan. 2009.

[63]   Huang, C., L. Wahlund, T. Dierks, P. Julin, B. Winblad, and V. Jelic. Discrimination of Alzheimer's disease and mild cognitive impairment by equivalent EEG sources: a cross-sectional and longitudinal study. Clin. Neurophysiol. 111(11): 1961-1967, Nov. 2000.

[64]   Hurley, R., J. McGowan, K. Arfanakis, and K. Taber. Traumatic axonal injury: novel insights into evolution and identification. J. Neuropsychiatry Clin. Neurosci. 16(1): 1-7, Winter 2004.

[65]   Ikonomovic, M., W. Klunk, E. Abrahamson, C. Mathis, J. Price, N. Tsopelas, B. Lopresti, S. Ziolko, W. Bi, W. Paljug, M. Debnath, C. Hope, B. Isanki, R. Hamilton, and S.

DeKosky. Post-mortem correlates of in vivo PiB-PET amyloid imaging in a typical case of Alzheimer's disease. Brain. 131(Pt. 6): 1630-1645, Jun. 2008.

[66]   Iqbal, K. A. Alonso, S. Chen, M. Chohan, E. El-Akkad, C. Gong, S. Khatoon, B. Li, F. Liu, A. Rahman, H. Tanimukai, and I. Grundke-Iqbal. Tau pathology in Alzheimer disease and other tauopathies. Biochim. Biophys. Acta. 1739(2-3): 198-210, Jan. 2005.

[67]   Jack, C. Jr., V. Lowe, M. Senjem, S. Wigand, B. Kemp, M. Shiung, D. Knopman, B. Boeve, W. Klunk, C. Mathis, and R. Petersen. ^{11}C PiB and structural MRI provide complementary information in imaging of AD and amnestic MCI. Brain 131(Pt. 3): 665-680, Mar. 2008.

[68]   Jasper, H. Report of committee on methods of clinical exam in EEG. Electroencephalogr. Clin. Neurophysiol. 10(2): 370-375, May 1958.

[69]   Jelles, B., P. Scheltens, W. van der Flier, E. Jonkman, F. da Silva, and C. Stam. Global dynamical analysis of the EEG in Alzheimer's disease: specific changes of functional interactions. Clin. Neurophysiol. 119(4): 837-841, Apr. 2008.

[70]   Jeong, J. EEG dynamics in patients with Alzheimer's disease. Clin. Neurophsyiol. 115(7): 1490-1505, Jul. 2204.

[71]   Jeong, J., J. Gore, and B. Peterson. Mutual information analysis of the EEG in patients with Alzheimer's disease. Clin. Neurophysiol. 112(5): 827-835, May 2001.

[72]   Jiang, Z. Abnormal cortical functional connections in Alzheimer's disease: analysis of inter- and intra-hemispheric EEG coherence. J. Zheniang Univ. Sci. B. 6(4): 259-264, Apr. 2005.

[73]   Leon-Carrion, J., J. Martin-Rodriguez, J. Damas-Lopez, J. Martin., and M. Dominquez-Morales. A QEEG index of level of functional dependence for people sustaining acquired brain injury: the Seville independence index (SINDI). Brain. Inj. 22(1): 61-74, Jan. 2008.

[74]   Kamiński, M. and H. Liang. Causal influence: advantages in neurosignal analysis. Crit. Rev. Biomed. Eng. 33(4): 347-430, 2005.

[75]   Kaplan, A., A. Fingelkurts, A. Fingelkurts, S. Borisov, and B. Darkhovsky. Nonstationary nature of the brain activity as revealed by EEG/MEG: methodological, practical and conceptual challenges. Signal Process. 85(11): 2190-2212, Nov. 2005.

[76]   Knyazeva, M., M. Jalili, A Brioschi, I. Bourquin, E. Fornari, M. Hasler, R. Meuli, P. Maeder, and J. Ghika. Topography of EEG multivariate phase synchronization in early Alzheimer's disease. Neurobiol. Aging. 31(7): 1132-1144, Jul. 2008.

[77]   Koenig, T., D. Lehmann, N Saito, T. Kuginuki, T. Kinoshita, and M. Koukkou. Decreased functional connectivity of EEG theta-frequency activity in first-episode, neuroleptic-naïve patients with schizophrenia: preliminary results. Sychizonphrenia Res. 50(1-2): 55-60, May 2001.

[78]   Krenker, A., J. Bešter, and A. Kos. Introduction to the Artificial Neural Networks. In: Artificial Neural Networks – Methodological Advances and Biomedical Applications. InTech, 2011, pp. 3-18.

[79]   Kullback, S. Information Theory and Statistics. New York, NY: Wiley, 1959.

[80]   Lachapelle, J., J. Bolduc-Teasdale, A. Pitto, and M. McKerral. Deficits in complex visual information processing after mild TBI: electrophysiological markers and vocational outcome prognosis. Brain Inj. 22(3): 265-274, Mar. 2008.

[81]   Lachaux, J.-P., E. Rodriguez, J. Martinerie, and F. Varela. Measuring phase synchrony in brain signals. Hum. Brain Mapp. 8(4): 194-208, 1999.

[82]   Lake, D., J. Richmann, M. Griffin, and J. Moorman. Sample entropy analysis of neonatal heart rate variability. Am. J. Physiol. 283(3): R789-R797, Sep. 2002.

[83]   Latchoumane, C., F. Vialatte, A. Cichocki, and J. Jeong. Multi-way analysis of Alzheimer's disease: classification based on space-frequency characteristics of EEG time series. Proc. World Congress on Engineering. 2: 1646-1649, Jul. 2008.

[84]   Leslie, K., D. Sessler, M. Schroeder, and K. Walters. Propofol blood concentration and the bispectral index predict suppression of learning during propofol/epidural anesthesia in volunteers. Anesth. Analg. 81(6): 1269-1274, Dec. 1995.

[85]   Leung, K. (E)-4-(2-(6-(2-(2-(2-([^{18}F]-fluoroenthoxy)ethoxy)ethoxy)pyridine-3-yl)vinyl)-N-methylbenzenamine. In: Molecular Imaging and Contrast Agent Database (MICAD). Bethesda, MD: National Center for Biotechnology Information, 2004-2013. Available at http://www.ncbi.nlm.nih.gov/books/NBK32300/.

[86]   Liu, J., H. Singh, and P. White. Electroencephalogram bispectral analysis predicts the depth of midazolam-induced sedation. Anesthesiology. 84(1): 64-69, Jan. 1996.

[87]   Locatelli, T., M. Cursi, D. Liberati, M. Franceschi, and G. Comi. EEG coherence in Alzheimer's disease. Electroencephalogr. Clin. Neurophysiol. 106(3): 229-237, Mar. 1998.

[88]   Mathworks. 2013. http://www.mathworks.com/matlab.

[89]   McBride, J., A. Sullivan, H. Xia, A. Petrie, and X. Zhao. Reconstruction of physiological signals using iterative retraining and accumulated averaging of neural network models. Physiol. Meas. 32(6): 661-675, Jun. 2011.

[90]   McBride, J., X. Zhao, N. Munro, C. Smith, G. Jicha, and Y. Jiang. Resting EEG Discrimination of early stage Alzheimer's disease from normal aging using inter-channel coherence graphs. Ann. Biomed. Eng. Mar. 2013. [Epub ahead of print]

[91]   McBride, J., X. Zhao, T. Nichols, V. Vagnini, N. Munro, D. Berry, and Y. Jiang. Scalp EEG-based discrimination of cognitive deficits after traumatic brain injury using event-related Tsallis entropy analysis. IEEE Trans. Biomed. Eng. 60(1): 90-96, Jan. 2013.

[92]   Meunier, D., S. Archard, A. Morcom, and E. Bullmore. Age-related changes in modular organization of human brain functional networks. Neuroimage. 44(3): 715-723, Feb. 2009.

[93]   Moody, G. The PhysioNet/Computing in Cardiology Challenge 2010: mind the gap. Comput. Cardiol. 37: 305-308, Jul. 2010.

[94]   Moretti, D., C. Fracassi, M. Pievani, C. Geroldi, G. Binetti, O. Zanetti, K. Sosta, P. Rossini, and G. Frisoni. Increase of theta/gamma ratio is associated with memory impairment. Clin. Neurophysiol. 120(2): 295-303, Feb. 2009.

[95]   National Institute of Neurological Disorders and Stroke. Traumatic brain injury: hope through research. Available at http://www.ninds.nih.gov/disorders/tbi/detail_tbi.htm.

[96]   Newton High Performance Computing Program. 2013. https://newton.utk.edu/.

[97]   Nikulin, V. and T. Brismar. Comment on 'multiscale entropy analysis of complex physiologic time series.' Phys. Rev. Lett. 92(8): 089803, Feb. 2004.

[98]   Park, J.-H., S. Kim, C.-H. Kim, A. Cichocki, and K. Kim. Multiscale entropy analysis of EEG from patients under different pathological conditions. Fractals. 15(4): 399-404, Feb. 2007.

[99]   Paul, D., and G. Rao. Correlation of bispectral index with Glasgow coma score in mild and moderate head injuries. J. Clin. Mont. Comput. 20(6): 339-404, Dec. 2006.

[100] Petersen, R. Mild Cognitive Impairment. New York, NY: Oxford Press, 2003.

[101] Petersen, R., R. Doody, A. Kurz, R. Mohs, J. Morris, P. Rabins, K. Ritchie, M. Rossor, L. Thal, and B. Winblad. Current concepts in mild cognitive impairment. Arch. Neurol. 58(12): 1985-1992, Dec. 2001.

[102] Petrov, T., J. Steiner, B. Braun, and J. Rafols. Sources of endothelin-1 in hippocampus and cortex following traumatic brain injury. Neurscience. 115(1): 275-283, 2002.

[103] Pijnenburg, A., R. Strijers, Y. Made, W. van der Filer, P. Scheltens, and C. Stam. Investigation of resting-state EEG functional connectivity in frontotemporal lobar degeneration. Clin. Neurophysiol. 119(8): 1732-1738, Aug. 2008.

[104] Pijnenburg, Y., Y. van der Made, A. van Cappellen van Walsum, D. Knol, P. Scheltens, and C. Stam. EEG synchronization likelihood in mild cognitive impairment and Alzheimer's disease during a working memory task. Clin. Neurophysiol. 115(6): 1332-1339, Jun. 2004.

[105] Pincus, S. and A. Goldberger. Physiological time-series analysis: what does regularity quantify? Am. J. Physiol. 266(4 Pt. 2): H1643-H1656, Apr. 1994.

[106] Pincus, S. Approximate entropy as a measure of system complexity. Proc. Natl. Acad. Sci. USA. 88(6): 2297-2301, Mar. 1991.

[107] Polikar, R., A. Topalis, D. Green, J. Kounois, and C. Clark. Comparative multiresolution wavelet analysis of ERP spectral bands using an ensemble of classifiers approach for early diagnosis of Alzheimer's disease. Comput. Biol. Med. 37(4): 542-558, Apr. 2007.

[108] Purves, D., G. Augustine, D. Ftizpatrick, L. Katz, A.-S. LaMantia, J. McNamara, and S. Williams. Neuroscience. 2nd ed. Sunderland, MA: Sinauer Associates, 2001.

[109] Quiroga, Q., O. Rosso, and E. Basar. Wavelet-entropy: a measure of order in evoked potentials. Electroencephalogr. Clin. Neurphysiol. 49: 229-303, 1999.

[110] Rampil, I. A primer for EEG signal processing in anesthesia. Anesthesiology. 89(4): 980-1002, Oct. 1998.

[111] Rampil, I. Electroencephalogram. In: Textbook of Neuroanesthesia with Neurosurgical and Neuroscience Perspectives. New York, NY: McGraw-Hill, 1997, pp. 193-219.

[112] Reijneveld, J., S. Ponten, H. Berendse, and C. Stam. The application of graph theoretical analysis to complex networks in the brain. Clin. Neurophsyiol. 118(11): 2317-1331, Nov. 2007.

[113] Richmann, J. and J. Moorman. Physiological time-series analysis using approximate entropy and sample entropy. Am. J. Physiol. Heart Circ. Phsiol. 278(6): H2039-H2049, Jun. 2000.

[114] Roche, R., P. Docktree, H. Garavan, J. Foxe, I. Robertson, and S. O'Mara. EEG alpha power changes reflection response inhibition deficits after traumatic brain injury (TBI) in humans. Neurosci. Lett. 362(1): 1-5, May 2004.

[115] Saeed, M., C. Lieu, G. Raber, and R. Mark. MIMIC II: a massive temporal ICU patient database to support research in intelligent patient monitoring. Comput. Cardiol. 29: 641-644, Sep. 2002.

[116]   Salvador, R., J. Suckling, M. Coleman, J. Pickard, D. Menon, and E. Bullmore. Neurophysiological architecture of functional magnetic resonance images of human brain. Cereb. Cortex. 15(9): 1332-13342, Sep. 2005.

[117]   Schmitt, F., P. Nelson, E. Abner, S. Scheff, G. Jicha, C. Smith, G. Cooper, M. Mendiondo, D. Danner, L. van Eldik, A. Caban-Holt, M. Lovell, and R. Kryscio. University of Kentucky Sanders-Brown healthy brain aging volunteers: donor characteristics, procedures and neuropathology. Curr. Alzheimer Res. 9(6): 724-733, Jul. 2012.

[118]   Schreiber, T. Measuring information transfer. Phys. Rev. Lett. 85(2): 461-464, Jul. 2000.

[119]   Schreiter-Gasser, U., V. Rousson, f. Hentschel, H. Sattel, and T. Gasser. Alzheimer's disease versus mixed dementias: an EEG perspective. Clin. Neurophysiol. 119(10): 2255-2259, Oct. 2008.

[120]   Shannon, C. The Mathematical Theory of Communication. Urbana, IL: University of Illinois Press, 1962.

[121]   Shaw, N. The neurophysiology of concussion. Prog. Neurobiol. 67(4): 281-344, Jul. 2002.

[122]   Signorino, M., E. Pucci, Belardinelli, G. Nolfe, and F. Angeleri. EEG spectral analysis in vascular and Alzheimer's dementia. Electroencephalogr. Clin. Neurophysiol. 94(5): 313-325, May 1995.

[123]   Sink, K., K. Holden, and K. Yaffe. Pharmacological treatment of neuropsychiatric symptoms for dementia: a review of the evidence. JAMA. 293(5): 596-560, Feb. 2005.

[124]   Snaedal, J., G. Johannesson, T. Gudmundsson, S. Gudmundsson, T. Pajdak, and K. Johnsen. The use of EEG in Alzheimer's disease, with and without scopolamine—a pilot study. Clin. Neurphysiol. 121(6): 836-841, Jun. 2010.

[125]   Sneddon, R. The Tsallis entropy of natural information. Physica A. 386(1): 101-118, Dec. 2007.

[126]   Sneddon, R. W. Shankle, J. Hara, A. Rodriguez, D. Horrman, and U. Saha. EEG detection of early Alzheimer's disease using psychophysical tasks. Clin. EEG Neurosci. 36(3): 141-150, Jul. 2005.

[127]   Soininen, H., J. Partanen, V. Laulumaa, E. Haelkala, M. Laaksi, and P. Riekkinen. Longitudinal EEG spectral analysis in early stage of Alzheimer's disease. Electroencephalogr. Clin. Neurophysiol. 72(4): 290-297, Apr. 1989.

[128]   Spiller, M. How local anesthesia affects nerves. Available at http://doctorspiller.com/Local_Anesthetics/local_anesthetics_4.htm.

[129]   Sporns, O., D. Chialvo, M. Kaiser, and C. Hilgetag. Organization, development and function of complex brain networks. Trends. Cogn. Sci. 8(9): 418-425, Sep. 2004.

[130]   Stam, C., B. Jones, G. Nolte, M. Breakspear, and P. Scheltens. Small-world networks and functional connectivity in Alzheimer's disease. Cereb. Cortex. 17(1): 92-99, Jan. 2007.

[131]   Stam, C., T. Montez, B. Jones. S. Rombouts, Y. van der Made, Y. Pijnenburg, and P. Scheltens. Disturbed fluctuations of resting state EEG synchronization in Alzheimer's disease. Clin. Neurophsyiol. 116(3): 708-715, Nar. 2005.

[132]   Stam, C., G. Nolte, and A. Daffertshofer. Phase lag index: assessment of functional connectivity from multi channel EEG with diminished bias from common sources. Hum. Brain Mapp. 28(11): 1178-1193, Nov. 2007.

[133]   Stam, C. and J. Reijneveld. Graph theoretical analysis of complex networks in the brain. Nonlinear Biomed. Phys. 1(1): 3, Jul. 2007.

[134]   Stam, C., Y. van der Made, Y. Pijnenburg, and P. Scheltens. EEG synchronization in mild cognitive impairment and Alzheimer's disease. Acta. Neurol. Scand. 108(2): 90-96, Aug. 2003.

[135]   Stam, C., and F. van Dijk. Synchronization likelihood: an unbiased measure of generalized synchronization in multivariate data sets. Physica D. 163(3-4): 236-251, Mar. 2002.

[136]   Stevens, A., T. Kricher, M. Nikola, M. Bartels, N. Rosellen, and H. Wornstall. Dynamic regulation of EEG power and coherence is lost early and globally in probable DAT. Eur. Arch. Psychiatry Clin. Neurosci. 251(5): 199-204, Oct. 2001.

[137]   Su, B., X. Wang, A. Nunomura, P. Moreira, H. Lee, G. Perry, M. Smith, and X. Zhu. Oxidative stress signaling in Alzheimer's disease. Curr. Alzheimer Res. 5(6): 525-532, Dec. 2008.

[138]   Sugihara, G., R. May, H. Ye, C. Hsieh, E. Deyle, M. Fogarty, and S. Munch. Detecting causality in complex ecosystems, Science 338(6106): 496-500, 2012.

[139]   Šušmáková, K. Human sleep and sleep EEG. Meas. Sci. Rev. 4(2): 59-74, 2004.

[140]   Thatcher, R., C. Biver, R. McAlester, M. Camacho, and A. Salazar. Biophysical linkage between MRI and EEG amplitude in closed head injury. Neuroimage. 7(4 Pt. 1): 352-367, Sep. 1998.

[141]   Thatcher, R., C. Biver, R. McAlester, and A. Salazar. Biophysical linkage between MRI and EEG coherence in closed head injury. Neuroimage. 8(4): 307-326, Mar. 1998.

[142]   Thatcher, R., D. North, F. Curtin, R. Walker, C. Biver, J, Gomez, and A. Salazar. An EEG severity index of traumatic brain injury. J. Neuropsychiarty Clin. Neurosci. 13(1): 77-87, Winter 2001.

[143]   Thomas, E. and A. Holmes Nonparametric permutation tests for functional neuroimaging: a primer with examples. Human Brain Mapp. 15(1): 1–25, Jan. 2001.

[144]   Tong, S., A. Bezerianos, A. Malhotra, Y. Zhu, and N. Thakor. Parameterized entropy analysis of EEG following hypoxic-ischemic brain injury. Phys. Lett. A. 314(5-6): 534-361, Aug. 2003.

[145]   Tononi, G., O. Sporns, and G. Edelman. A measure for brain complexity: relating functional segregation and integration in the nervous system. Proc. Natl. Acad. Sci. USA. 91(11): 5033-5037, May 1994.

[146]   Tyszka, J., S. Grafton, W. Chew, R. Woods, and P. Colletti. Parceling of mesial frontal motor areas during ideation and movement using functional imaging at 1.5 tesla. Ann. Neurol. 35(6): 746-749, Jun. 1994.

[147]   Vagnini, V., D. Berry, J. Clark, and Y. Jiang. New measures to detect malingered neurocognitive deficit: applying reaction time and event-related potentials. J. Clin. Exp. Neuropsychol. 30(7): 766-776, Oct. 2008.

[148]   van der Hiele, K., A. Vein, R. Reijntjes, R. Westendorp, E. Bollen, M. van Buchen, J. van Dijk, and H. Middlekoop. EEG correlates in the spectrum of cognitive decline. Clin. Neurophysiol. 118(9): 1931-1939, Sep. 2007.

[149]   van Deursen, J., E. Vuurman, F. Verhey, V. van Kranen-Mastenbroek, and W. Riedel. Increased EEG gamma band activity in Alzheimer's disease and mild cognitive impairment. J. Neural Transm. 115(9): 1301-1311, Sep. 2009.

[150] Wada, Y., Y. Nanbu, Y. Koshino, N. Yamaguchi, and T. Hashimoto. Reduced interhemispheric EEG coherence in Alzheimer's disease: analysis during rest and photic stimulation. Alzheimer Dis. Assoc. Disord. 12(3): 175-181, Sep. 1998.

[151] Waldemar, G., B. Dubois, M. Emre, J. Georges, I. McKeith, M. Rossor, P. Scheltens, P Tariska, and B. Winblad. Recommendations for the diagnosis and management of Alzheimer's disease and other disorders associated with dementia: EFNS guidline. Uer. J. Neurol. 14(1): e1-26, Jan. 2007.

[152] Wallace, B., A. Wagner, E. Wagner, and J. McDeavitt. A history and review of quantitative electroencephalography in traumatic brain injury. J. Head Trauma Rehabil. 16(2): 165-190, Apr. 2001.

[153] Wan, B., D. Ming, H. Qi, Z. Xue, Y. Tin, Z. Zhou, and L. Cheng. Linear and nonlinear quantitative EEG analysis. IEEE Eng. Med. Biol. Mag. 27(5): 58-63, Sep.-Oct. 2008.

[154] Watts, D., and S. Strogatz. Collective dynamics of 'small-world' networks. Nature. 393(6684): 440-442, Jun. 1998.

[155] Wee, C., P. Tap, W. Li, K. Denny, J. Browndyke, G. Potter, K. Welsh-Bohmer, L. Wang, and D. Shen. Enriched white matter connectivity networks for accurate identification of MCI patients. Neuroimage. 54(3): 1812-1822, Feb. 2011.

[156] Weiner, M., D. Veitch, P. Aisen, L. Beckett, N. Cairns, R. Green, D. Harvey, C. Jack, W. Jagust, E. Liu, J. Morris, R. Petersen, A. Aykin, M. Schmidt, L. Shaw, J. Siuciak, H. Soares, A. Toqa, and J. Trojanowski. The Alzheimer's disease neuroimaging initiative: a review of papers published since its inception. Alzheimers Dement. 8(1 Suppl.): S1-68, Feb. 2012.

[157] WETA. BrainLine.org. Available at http://www.brainline.org/index.html.

[158] White, E. Cell types. In: Cortical Circuits: Synaptic Organization of the Cerebral Cortex—Structure, Function and Theory. Boston, MA: Birkäuser, 1989, pp. 19-45.

[159] Wong, D., P. Rosenberg, Y. Zhou, A. Kumar, V. Raymont, H. Ravert, R. Dannals, A. Nandi, J. Brasić, W. Ye, C. Lyketsos, H. Kung, A. Joshi, D. Skovronsky, and M. Pontecorvo. In vivo imaging of amyloid deposition in Alzheimer disease using the radioligand ^{18}F-AV-45 (florbetapir F 18). J. Nucl. Med. 51(6): 913-920, Jun. 2010.

[160] Woon, W., A. Cichocki, F. Vialatte, and T. Musha. Techniques for early detection of Alzheimer's disease using spontaneous EEG recordings. Physiol. Meas. 28: 335-347, Apr. 2007.

[161] Yagyu, T., J. Wackermann, M. Shigeta, V. Jelic, T. Kinoshita, K. Kochi, P. Julin, O. Almkvist, L. Wahlund, I. Kondakor, and D. Lehmann. Global dimensional complexity of multichannel EEG in mild Alzheimer's disease and age-matched cohorts. Dement. Geriatr. Cogn. Disord. 8(6): 343-347, Nov.-Dec. 1997.

[162] Zetterberg, H., N. Mattson, and K. Blennow. Cerebrospinal fluid analysis should be considered in patients with cognitive problems. Int. J. Alzheimer Dis. 2010: 163065, Jul. 2010.

[163] Zhang, D., X. Jia, H. Ding, D. Ye, and N. Thakor. Application of Tsallis entropy for EEG: quantifying the presence of burst suppression after asphyxia cardiac arrest in rats. IEEE Trans. Biomed. Eng. 57(4): 867-74, Apr. 2010.

[164] Zhao, P., P. Van-Eetvelt, C. Goh, N. Hudson, S. Wimalaratna, and E. Ifeachor. Characterization of EEGs in Alzheimer's disease using information theoretic methods. Proc. IEEE Eng. Med. Biol. Soc. 2007: 512705131, 2007.

VITA

Joseph Curtis McBride was born on June 13th, 1988 in Little Rock, AR but was raised in East Tennessee. He graduated with a Bachelor of Science in Biomedical Engineering from the University of Tennessee-Knoxville (UTK) in 2010. He is currently (as of March 2014) a PhD Candidate in Biomedical Engineering at UTK and enrolled in the Master of Engineering Management program at the University of Tennessee Space Institute. He has served as course instructor and guest lecturer for several graduate and undergraduate courses at UTK and is the author of the second edition of *Exercises in Engineering Experimentation*, the laboratory manual for the College of Engineering instrumentation and measurement curriculum. Joseph lives with his wife and son in Knoxville, TN.